

June 2021

Phasor Domain Modeling of Type-III Wind Turbines

Mohammed Alqahtani
University of South Florida

Follow this and additional works at: <https://digitalcommons.usf.edu/etd>



Part of the [Electrical and Computer Engineering Commons](#)

Scholar Commons Citation

Alqahtani, Mohammed, "Phasor Domain Modeling of Type-III Wind Turbines" (2021). *USF Tampa Graduate Theses and Dissertations*.

<https://digitalcommons.usf.edu/etd/9650>

This Dissertation is brought to you for free and open access by the USF Graduate Theses and Dissertations at Digital Commons @ University of South Florida. It has been accepted for inclusion in USF Tampa Graduate Theses and Dissertations by an authorized administrator of Digital Commons @ University of South Florida. For more information, please contact scholarcommons@usf.edu.

Phasor Domain Modeling of Type-III Wind Turbines

by

Mohammed Alqahtani

A dissertation submitted in partial fulfillment
of the requirements for the degree of
Doctor of Philosophy in Electrical Engineering
Department of Electrical Engineering
College of Engineering
University of South Florida

Co-Major Professor: Zhixin Miao, Ph.D.
Co-Major Professor: Lingling Fan, Ph.D.
Nasir Ghani, Ph.D.
Rasim Guldiken, Ph.D.
Kaiqi Xiong, Ph.D.

Date of Approval:
June 15, 2021

Keywords: Doubly-fed induction generator, squirrel-cage induction machine, voltage unbalance, harmonic analysis, space vector

Copyright © 2021, Mohammed Alqahtani

Dedication

To my parents, wife, sisters, and brother.

Acknowledgments

First, I would like to express my deepest gratitude to my advisor, Dr. Zhixin Miao, for the opportunity to work under his supervision during my Ph.D. studies. I appreciate his endless support, guidance, training, and encouragement throughout the past four years. I would thank Dr. Lingling Fan for her unlimited help and support. She has always been available for discussion, and she has helped me to overcome several research obstacles with her sharp insight.

Second, I would like to thank and appreciate the rest of the committee members: Dr. Nasir Ghani, Dr. Rasim Guldiken, and Dr. Kaiqi Xiong, for providing valuable comments and encouragement.

I would like to thank Prince Sattam bin Abdulaziz University for providing me with the full scholarship to pursue my Ph.D. degree.

I would like to extend my sincere appreciation and thanks to my recent colleagues from the smart grid power system lab, in particular Ali Aljumah, Sulaiman Almutairi, Abdullah Alburidy, Rabi Kar, Abdulhakim Alsaif, Zhengyu Wang, Abdullah Alassaf, Yangkun Xu, and my former colleagues Dr. Yin Li, Dr. Minyue Ma, Dr. Ibrahim Alsaleh and Dr. Anas Almunif.

Last but not least, I would like to express my gratitude, appreciation and thank my parents, wife, sisters, and brother for their support, encouragement, and sacrifices during my studies.

Table of Contents

List of Tables	iv
List of Figures	vi
Abstract	x
Chapter 1: Introduction	1
1.1 Background	1
1.2 Types of Wind Turbines	2
1.3 Wind Farms Modeling	3
1.4 Terms and Definitions	6
1.5 Statement of the Problem and Research Tasks	6
1.5.1 Task-A: Analysis of Type-III WT's Under Balanced Conditions	10
1.5.2 Task-B: Analysis of Type-III WT's Subject to Unbalance	12
1.6 Outline of the Dissertation	14
Chapter 2: Steady-State Modeling of Type-III WT's Under Balanced Voltage	15
2.1 Introduction	15
2.2 Squirrel Cage Induction Machine (Testbed-A)	15
2.2.1 Equivalent Circuits of an Induction Machine	16
2.2.2 Steady-State Calculations	17
2.2.3 Case Study 1: State Variables Calculations	18
2.2.4 Case Study 2: Minimal Grid Voltage a Motor Can Handle	19
2.3 Type-III Wind Turbine (Testbed-B)	21
2.3.1 Steady-State DFIG-Based WT Model	22
2.3.1.1 DFIG Equivalent Circuit	22
2.3.1.2 Power Equations	23
2.3.2 Control System	24
2.3.2.1 Converters Currents Limits	25
2.3.2.2 Controller Target	27
2.3.2.3 Control Modes	28
2.3.3 Voltage Thresholds Identification	29
2.3.3.1 Validation of the Voltage Thresholds	32
2.3.4 Calculating Steady-State Operating Conditions for Type-III WT	38
2.4 Conclusion	39

Chapter 3: Steady-State Analysis of Type-III Wind Turbines Subject to Unbalance	41
3.1 Introduction	41
3.2 Squirrel Cage Induction Machine (Testbed-A)	42
3.2.1 Equivalent Circuits of an Induction Machine	42
3.2.2 Ripples in the Torque	44
3.2.3 Steady-State Calculations	44
3.2.3.1 Initial Values	45
3.2.4 Case Studies	46
3.2.4.1 Motor State Variables During Unbalanced Voltage	46
3.2.4.2 Maximum Torque During Unbalanced Voltage Dip	48
3.3 Type-III Wind Turbine (Testbed-B)	50
3.3.1 Induction Machine Circuit Analysis (DFIG)	50
3.3.2 Constant Modulation Index	54
3.3.2.1 GSC Ac Side and DC/AC Relationship	55
3.3.2.2 RSC	59
3.3.2.3 DC-Link	60
3.3.2.4 Validation	61
3.3.3 Current Control Considered	63
3.3.3.1 DQ to ABC	66
3.3.3.2 Control Signals	70
3.3.3.3 Validation	70
3.3.4 Outer Loops Considered	73
3.3.4.1 GSC Power	76
3.3.4.2 RSC Power	77
3.3.4.3 DC-Link Power	77
3.3.4.4 Control Signals	78
3.3.4.5 Controller Target	78
3.3.4.6 Validation	79
3.4 Conclusion	79
Chapter 4: Mixed Integer Programming-Based Modeling	85
4.1 Introduction	85
4.2 MIP Formulation for Type-III WTs Modeling	86
4.2.1 System Configuration	86
4.2.1.1 Control System	86
4.2.1.2 LVRT Function	88
4.2.2 Optimization Problem Formulation	89
4.2.2.1 Scenario-P1 Modeling	91
4.2.2.2 Scenario-P2 Modeling	91
4.2.2.3 MIP Formulation	92
4.2.2.4 LVRT Considered	94
4.2.3 Validation	95

4.3	MIP Formulation for Fault Location Identification	100
4.3.1	Overview	100
4.3.2	Fault Identification in a Tree Network	103
4.3.3	Minimum Placement of MicroPMUs	105
4.3.4	MIP Formulation for Three-Phase Systems	108
4.3.4.1	Faulted Bus and Phase Determination	110
4.3.5	Numerical Examples	111
4.3.5.1	The IEEE 37-Bus System	112
4.3.5.2	The IEEE 123-Bus System	114
4.3.5.2.1	Less Number of MicroPMUs	118
4.3.5.2.2	Noisy MicroPMUs	118
4.3.5.3	134-Node Real-Life Feeder	120
4.3.5.3.1	DG Penetration	122
4.3.5.3.2	Errors in Line Impedance	122
4.3.5.3.3	MicroPMUs Synchronization Errors	123
4.3.6	Discussion and Comparison	124
4.4	Conclusion	126
Chapter 5:	Conclusion and Future Work	130
5.1	Conclusion	130
5.2	Future Work	131
5.2.1	Islanded Microgrid Power Flow	131
	References	134
	Appendix A: Copyright Permissions	143
	About the Author	End Page

List of Tables

Table 2.1	Parameters of Simulink model (Testbed-B)	19
Table 2.2	Motor Variables	19
Table 2.3	Parameters of Simulink model (Testbed-B)	32
Table 2.4	Parameters of the Simulink model	40
Table 2.5	Steady-state results	40
Table 3.1	Motor variables	47
Table 3.2	Model parameters	63
Table 3.3	Results comparison (constant modulation index)	64
Table 3.4	Results comparison (inner loops)	72
Table 3.5	Results comparison (two-level controller)	82
Table 4.1	Parameters of Simulink model	95
Table 4.2	Phase-to-ground faults ($\Delta - \Delta$)	113
Table 4.3	Double and three-phase faults ($\Delta - \Delta$)	113
Table 4.4	Identification results for the IEEE 37-bus feeder ($\Delta - Y$)	115
Table 4.5	Identification results for the IEEE 123-bus test feeder	119
Table 4.6	Identification results with noise considered for the IEEE 123-bus test feeder	119

Table 4.7 Comparison between the proposed method in this paper with [77] and [79]

128

List of Figures

Figure 1.1	The four main wind turbine technologies [7].	3
Figure 1.2	Wind farm-A.	5
Figure 1.3	FAM representation of wind farm-A.	5
Figure 1.4	SAM representation of wind farm-A.	5
Figure 1.5	MMM representation of wind farm-A.	6
Figure 1.6	RL circuit.	8
Figure 2.1	System configuration (Testbed-A).	16
Figure 2.2	Positive-sequence equivalent circuit.	16
Figure 2.3	EMT model configuration (Testbed-A).	18
Figure 2.4	Induction motor response to change in voltage.	20
Figure 2.5	Motor response.	21
Figure 2.6	System configuration (Testbed-B).	22
Figure 2.7	Equivalent circuit of the DFIG.	23
Figure 2.8	RSC control.	25
Figure 2.9	GSC control.	25
Figure 2.10	RSC control modes.	29
Figure 2.11	GSC control modes.	29

Figure 2.12	Proposed algorithm.	30
Figure 2.13	EMT model configuration (Testbed-B).	33
Figure 2.14	System response to changes in the voltage (Case-A).	34
Figure 2.15	System response to changes in the voltage (Case-B).	35
Figure 2.16	System response to changes in the voltage (Case-C).	36
Figure 2.17	System response to changes in the voltage (Case-D).	37
Figure 2.18	Steady-state model of the given system.	39
Figure 2.19	EMT model configuration.	39
Figure 3.1	Induction motor equivalent circuit	42
Figure 3.2	Simulation results.	47
Figure 3.3	Rotor currents of the induction motor.	48
Figure 3.4	Torque-speed curve of induction motor.	49
Figure 3.5	Induction motor response to change in load torque.	49
Figure 3.6	Motor response for change in load torque.	51
Figure 3.7	DFIG equivalent circuit.	53
Figure 3.8	Type III WTs (constant modulation index).	55
Figure 3.9	GSC ac side	56
Figure 3.10	DC-link circuit representation.	60
Figure 3.11	Steady-state equations (constant modulation index).	62
Figure 3.12	MATLAB/SimPowerSystems testbed.	63
Figure 3.13	Simulation waveforms (constant modulation index).	64

Figure 3.14	FFT analysis (constant modulation index).	65
Figure 3.15	Type III WTs (with current control).	65
Figure 3.16	Current control.	67
Figure 3.17	Steady-state equations (current control).	71
Figure 3.18	Simulation waveforms (current control considered).	73
Figure 3.19	FFT analysis (current control considered).	74
Figure 3.20	Outer control.	75
Figure 3.21	Steady-state equations (two-level controller).	81
Figure 3.22	Simulation waveforms (two-level controller).	83
Figure 3.23	FFT analysis (two-level controller).	84
Figure 4.1	Type-III WTs.	86
Figure 4.2	RSC control.	87
Figure 4.3	GSC control.	88
Figure 4.4	Operating modes combinations.	89
Figure 4.5	Reduced operating modes combinations.	90
Figure 4.6	Comparison between the simulation and proposed method results.	96
Figure 4.7	Comparison between the simulation and proposed method results.	97
Figure 4.8	Comparison between the simulation and proposed method results.	98
Figure 4.9	Comparison between the simulation and proposed method results.	99
Figure 4.10	A fault scenario can be viewed as the superposition of two circuits.	104
Figure 4.11	Modified version of the IEEE 37-bus test feeder.	112

Figure 4.12	Modified version of the IEEE 123-bus test feeder.	116
Figure 4.13	Simulation results of the fault-location algorithm.	117
Figure 4.14	MicroPMUs placement with reduced number.	120
Figure 4.15	Simulation results by the reduced number of microPMUs.	121
Figure 4.16	Simulation results with noise.	122
Figure 4.17	Single-line diagram of the 134-node feeder [89].	123
Figure 4.18	Simulation results of the fault identification algorithm.	124
Figure 4.19	Simulation results with DGs.	125
Figure 4.20	Simulation results with errors in line impedances.	126
Figure 4.21	Simulation results with microPMUs synchronization errors.	127
Figure 4.22	Location error for different faults ($R_f=1 \Omega$) using microPMUs.	128

Abstract

This dissertation research focuses on developing an accurate steady-state phasor model for Doubly Fed Induction Generator (DFIG)-based wind turbines (Type-III WTs). Unlike the classical synchronous or asynchronous generators, Type-III WTs are electronically coupled to the power grid. The steady-state and dynamic responses of the DFIG-based WTs depend on the behavior of the converters controllers. Accurate modeling requires reproducing the behavior of the power electronics and the control system for various operating scenarios. The analysis of this research area is carried out in two stages or tasks. The first task focuses on the balanced stator voltage situation, while the unbalanced stator voltage is considered in the second task.

In the first task, two methods to compute steady-state operating conditions of Type-III WTs considering the control limits are proposed. The proposed methods are applicable for ideal operating conditions and undervoltage scenarios. In the first method, an optimization problem is first formulated to identify the voltage thresholds at which the behavior of the control system changes due to the current limits. Using the identified limits, an efficient algorithm for steady-state calculations is designed. The problem is formulated as equality and inequality constraints and solved using a non-linear programming solver. In the second method, a one-step algorithm is developed. An efficient algorithm using Mixed Integer Non-Linear Programming (MINLP) is developed to compute the steady-state operating point of Type-III WTs. For a given stator voltage and wind speed, the electrical and mechanical variables of the system can be computed. A full-order model of DFIG-based WT is considered. Some overly simplifying assumptions that are commonly adopted in the literature are

avoided. Losses in the back-to-back converters, and nonzero reactive power support through the grid-side converter (GSC) are considered. Compared to state-of-the-art, the proposed methods are much more accurate computation models for DFIGs. The proposed methods are validated with electromagnetic transient (EMT) simulations.

In the second task, an adequate model of Type-III WTs under grid unbalance is proposed. The proposed model takes into consideration not only positive-, negative-sequence circuits but also the 3rd harmonic circuit. In addition to modeling, we design an efficient algorithm for steady-state analysis. To this end, harmonic circuit analysis of the induction machine, the rotor-side converter (RSC), the dc-link, and the GSC ac side is first carried out. Furthermore, relationships between dc side variables and ac side variables of the two dc/ac converters are investigated. The steady-state analysis problem is formulated as a set of algebraic equality constraints. This formulation is defined in YALMIP, a MATLAB interface for optimization problems. The optimization problem is solved by a non-linear optimization solver. The results of the steady-state analysis are phasors of harmonic components at steady-state. They are compared with and validated by the phasors obtained from Fourier transforms of electromagnetic transient (EMT) simulation results.

Chapter 1: Introduction

This chapter, first, gives a brief background about wind farms and how they are modeled in power systems. Then, the motivation of this research is presented, and the research scope is identified. The relevant literature and approaches are briefly introduced for each task, and our contribution is presented. The definition of some terminologies that are used throughout the paper is provided in this chapter.

1.1 Background

Recently, the number of wind farms integrated into power systems has increased significantly. Highlights of the wind power development include:

- Between 2010-2020, the capacity of the wind farm power generation increased by 166% in the U.S., with an average of 10% annually [1]. Globally, wind capacity increased by 15% annually, from 2009 to 2019 [2].
- In 2019, over 7% of the total U.S. electricity was supplied by wind farms. Iowa and Kansas states generated over 40% of their electricity by wind energy. In the same year, \$13 billion was invested in the U.S. to add over 9 gigawatts of wind power capacity. It is expected that more than 10 gigawatts of wind power capacity will be added in 2020 [3], and 20% of the nation's electric generation will be produced by wind energy in 2030 [4].

- Since 2010, the U.S. average turbine capacity has increased by more than 40% compared to a 13% increase in average hub height. Further growth is expected by wind experts [5].

1.2 Types of Wind Turbines

Based on AC generator types and converter types, wind turbines are classified into four types, as shown in Fig 1.1 [6]. In Type-I WTs, which is the early technology used in wind turbines, a Squirrel-Cage Induction Generator (SCIG) is deployed in fixed-speed applications. A straightforward power conversion technique is implemented. The induction machine is directly connected to the grid, allowing minimal variation in speed, limiting the power flow's ability, and reducing efficiency. The main advantage of this design is the cheap and straightforward construction. In Type-II WTs, a wounded-rotor induction machine with rotor resistance control is used. Unlike a squirrel-cage induction generator with its rotor short-circuited, the wound-rotor machine has its rotor terminals accessible. The machine's rotor is connected to variable resistors, which gives the ability to control the speed of the machine in a limited range. An efficient way of converting the mechanical power produced by the wind to electric power requires a design that can generate a constant frequency AC from mechanical power with a wide range of variable speeds. Type-III and Type-IV wind turbines can operate by variable speed prime movers while generating fixed frequency electricity. That ability allows higher energy capture and more control on power flow.

Type-III WTs use Doubly-Fed Induction Generators (DFIG). The rotor of a DFIG is fed with a variable-frequency and variable-magnitude three-phase voltage. Using voltage-source converters connected to the rotor side of the DFIG, the frequency and amplitude of the voltage injected into the rotor can be controlled. The stator frequency is kept constant to the grid nominal frequency [8]. As the two back-to-back converters are connected to the rotor side, the converter power rating is reduced significantly compared to other wind conversion systems in which the converters are connected directly to the stator. In addition,

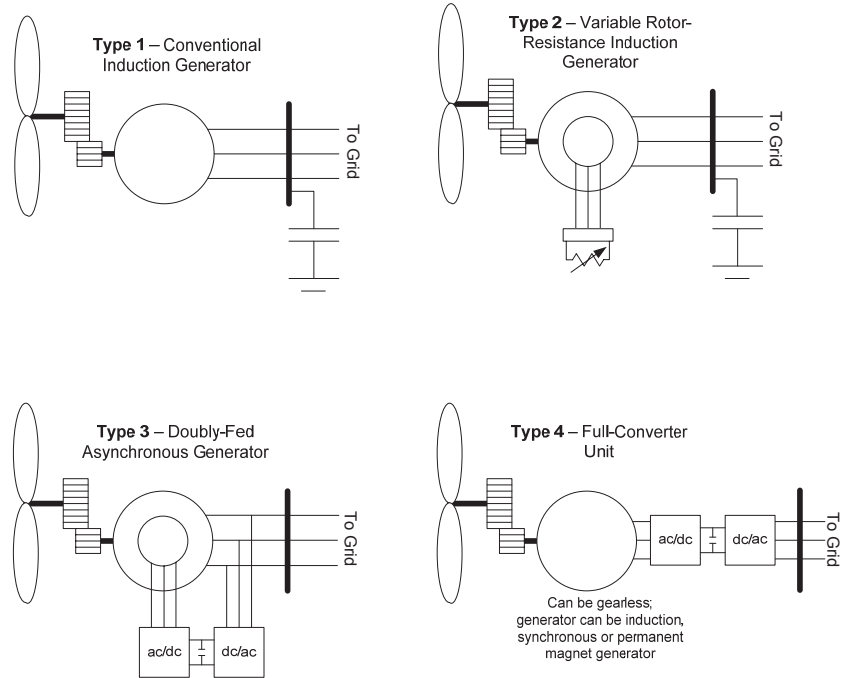


Figure 1.1: The four main wind turbine technologies [7]. Copyright © 2013, IEEE. Permission is included in Appendix A.

the DFIG can generate more than its rated power without suffering overheating issues since the significant part of the power is drawn from the stator [9]. The power rating of the converters is between 25-35% of the nominal power of the generator; thus, fewer power losses compared to other wind conversion techniques [10].

In Type-IV WTs, a permanent magnet synchronous or squirrel-cage induction generator can be used. The generator is integrated into power systems with full-rated power electronic converters. As the generator is decoupled from the grid using a back-to-back converter, the generator can operate at a wide range of speed for optimal power capture.

1.3 Wind Farms Modeling

A wind farm can be represented and modeled using a detailed or aggregated model [11]. In the detailed model (one-to-one modeling), each wind turbine in the farm is completely

modeled with its internal electric network. This model is usually used when studying the dynamic behavior of a small number of wind turbines. However, when dealing with a large number of wind turbines, the computation time becomes an issue because of the high order of the model. To overcome that issue, several aggregated models have been proposed. The key idea in the aggregation is to maintain the entire response of the entire wind farm at the point of common coupling (PCC) while reducing the computational burden.

The performance of a wind turbine depends mainly on the incoming wind speed. Within the wind farm, the wind captured by each wind turbine is different in most situations. As a result, the aggregation methods are mainly divided based on how the model handles the wind speed variation within the farm.

- Full Aggregated Model (FAM): In this model, all the wind turbines within the farm are aggregated into one equivalent wind turbine with an equivalent internal electric circuit. This model is the fastest in terms of computational speed due to the reduced-order model. This method is effective and suitable for equal wind distribution among the farm. However, during irregular wind distribution, the major challenge in this representation is the calculation of the equivalent wind for the equivalent wind turbine in a way that matches the behavior of the entire wind farm.
- Semi Aggregated Model (SAM): In this model, the generators in the wind turbines are modeled as one equivalent unit, while the turbines are modeled individually. That means multiple turbines drive one equivalent generator to consider the effect of the different wind speeds within the wind farm.
- Multi Machine Model (MMM): In this model, the group of wind turbines receiving the same incoming wind are aggregated into one equivalent machine. In this model, the wind farm is represented by multiple equivalent machines depending on the incoming wind speed.

Fig. 1.2 shows a wind farm with irregular wind distribution. Fig. 1.3, Fig. 1.4 and Fig. 1.5 show the FAM, SAM and MMM, respectively, for the wind farm A shown in Fig. 1.2.

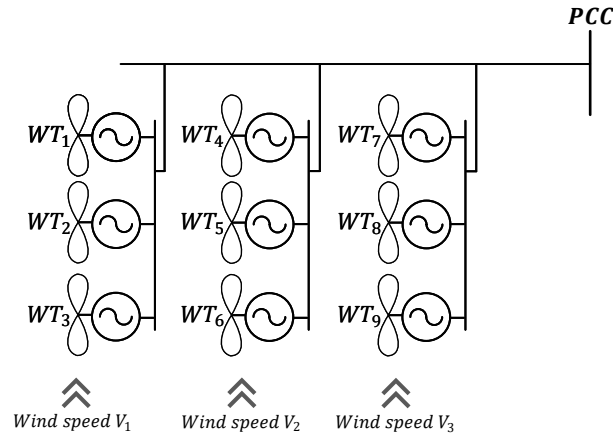


Figure 1.2: Wind farm-A.

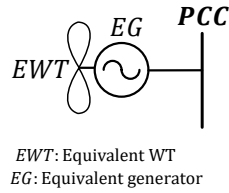


Figure 1.3: FAM representation of wind farm-A.

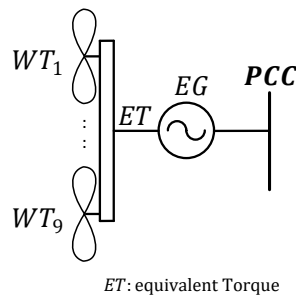


Figure 1.4: SAM representation of wind farm-A.

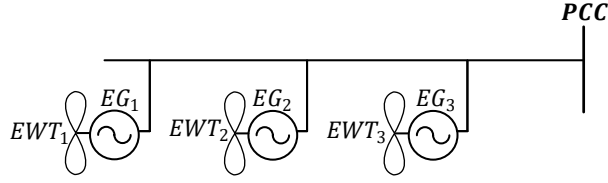


Figure 1.5: MMM representation of wind farm-A.

1.4 Terms and Definitions

This section describes some terminologies that are used to describe some power quality issues that will be mentioned throughout the dissertation. [12, 13].

- Undervoltage: Is a diminishing in the Root-Mean-Squared (RMS) AC voltage to less than 90% at the power frequency for longer than 60 seconds. Faults, switching off a capacitor bank, or switching on a large load may cause that event.
- Voltage unbalance: The ratio of the negative sequence component to the positive sequence component, usually expressed as a percentage. In normal balanced conditions, the three-phase voltages are identical in magnitude, and the phase angles are displaced 120 degrees. The unbalance condition is when there is a difference in magnitude of the voltage or the phase angle, or both. Single-phase faults, single-phase loads, or blown fuses in one of the three-phases capacitor banks can cause an unbalanced condition.
- Waveform distortion and harmonics: A distorted waveform is a non-ideal sine wave of the power frequency at steady-state. Harmonics are sinusoidal waves with a frequency that is an integer multiple of the power system's fundamental frequency.

1.5 Statement of the Problem and Research Tasks

In past years, wind farm plants were allowed to be disconnected during non-ideal operation conditions to protect the converters from overcurrent or overvoltage. Due to the high

penetration of wind farms in electric power systems, stricter grid codes have been enforced by transmission system operators (TSOs) worldwide. Wind farms should remain connected to support the grid during some abnormal conditions in order to avoid more severe scenario, such as cascading failure and voltage collapse [14, 15].

For instance, in 2011, a severe failure occurred in North China Power Grid. A two-phase fault of a 35 kV overhead line caused the voltage protection relays of 644 wind turbines to operate and disconnect the wind farms from the system, which led to a loss of 854 MW of the injected power. As a result, the frequency of the North Power Grid dropped to 49.95 Hz [16]. Another catastrophic failure happened on April 25th in Gansu. Because of a severe weather condition, a three-phase fault occurred at a 330 kV substation in Jiayuguan. As a result of the large voltage drop that occurred, wind farms connected to the Yumen 330 kV substation were disconnected. Voltage protection relays of Guazhou wind turbines tripped off as well. 1535 MW was lost due to that event [17].

Consequently, the focus of the researchers in that field has shifted from the assumption of having an ideal grid voltage condition to investigate abnormal grid conditions [18]. This topic has been a subject of great interest. Studies have been conducted considering steady-state and dynamic conditions such as low-voltage ride-through [19, 20], unbalance voltage [21–23], voltage regulation [24], and dynamic modeling [25–28].

The dynamic and steady-state responses of DFIG-based WT can be studied with high precision in the time domain using electromagnetic-transient simulations. The behavior of the electronically coupled generators can be reproduced accurately using this technique. This modeling approach relies on solving a large set of ordinary differential equations (ODEs). Besides the computational burden by the ODEs, which increases the execution time, running time-domain simulation requires detailed modeling of every element of the system and adequate tuning for the control parameters. To prevent numerical issues that may occur when

starting the electromagnetic simulations due to the large set of non-linear ODEs, setting initial conditions of the state variables is essential.

Alternatively, the analysis can be carried out in the frequency domain. Indeed, steady-state analysis is usually done using the frequency domain as it is more convenient. Load flow and short circuit analysis are fundamental studies conducted in the frequency domain. When the analysis is carried in the frequency domain, the system can be described using algebraic equations instead of ODEs. For instance, consider the simple RL circuit.

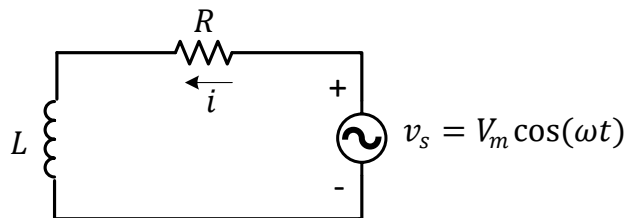


Figure 1.6: RL circuit.

By applying using Kirchhoff voltage law, the simple circuit shown in can be expressed in the time domain by the ODE in (1.1), while it is expressed in the frequency domain using a complex algebraic equation as shown in (1.2). The current flowing in the circuit can be found by either integrating the ODE or directly using the algebraic equation.

$$V_m \cos(\omega t) = Ri + L \frac{di}{dt} \quad (1.1)$$

$$\bar{V} = \bar{I}(R + j\omega L) \quad (1.2)$$

As mentioned earlier, principal studies in the power system that deal with very large systems are carried out in the phasor domain; however, there is a lack of accurate phasor modeling of the electronically coupled generator, specially WTs [29]. For instance, available shorts circuit software packages ignore the complexity of the power electronics control system in the WTs and model it as either a voltage source behind an impedance, how the conven-

tional synchronous machine is modeled, or as a current source with a pre-defined current value. Using a voltage source behind an impedance for modeling traditional electromechanical rotating machines can be considered accurate modeling, but it is not well suited for electronically coupled generators [29].

Although these modeling approaches are not very accurate, they were justified as the number of the converter-based WTs was not huge, and the inaccuracy of the modeling would not have a significant impact on the overall analysis of the system. Now, with the high penetration of the electronically coupled WTs, accurate modeling is essential. Accurate modeling can be achieved by reproducing the behavior of power electronics and the control system for various operating scenarios.

This dissertation aims to develop an accurate phasor domain model for Type-III WTs that fully represents the steady-state response of the WTs under various stator voltage scenarios. Achieving that goal can improve the load flow and short circuit analysis of power systems with penetrated Type-III WTs. Moreover, it can improve the initialization process of the EMT simulation models.

In order to archive the principal goal of the dissertation, designing efficient algorithms for steady-state analysis of Type-III WTs, this research is divided into two main tasks as the following.

1. Task-A: To construct an accurate computing model for Type-III WTs steady-state calculations considering the control system response for different stator voltage levels (balanced dip).
2. Task-B: To adequately model Type-III WTs under unbalance stator voltage by considering not only positive- and negative-sequence circuits but also harmonics circuits associated with the unbalanced condition, and design an efficient algorithm for steady-state calculations.

1.5.1 Task-A: Analysis of Type-III WTs Under Balanced Conditions

Due to the increase in wind power generation, the number of DFIGs has increased over the last decades [30]. The penetration of the DFIG-based WTs into power systems has changed its characteristics and behavior, which gives rise to significant challenges. The stability of the power systems is remarkably affected by the penetration of the wind farms [31]. Researchers and engineers commonly use eigenvalues analysis and time-domain simulations to study the DFIG integrated power systems. Both techniques require an initial operating point which can be obtained using steady-state analysis. Accurate steady-state values are essential to prevent numerical issues that may occur when starting the electromagnetic simulations due to the large set of nonlinear ordinary differential equations [32]. Unlike synchronous generators, the non-linearity of the DFIG-based WTs equations complicates the calculation process.

Iterative [30,33–35] and non-iterative (direct) [32,36,37] methods have been proposed to calculate the steady-state operating point of the DFIG-based WTs. In the iterative method, Newton-Raphson is adopted to solve the non-linear equations of the DFIG. In the direct methods, authors overcome the nonlinearity by assuming known rotor speed and use basic calculus to solve the system. Compare to iterative methods, direct approaches require less computation time and do not involve convergence issues. However, most direct methods ignore the losses of the back-to-back converters or use a reduced-order DFIG model, which reduces the methods' accuracy. In [32], the authors proposed a non-iterative approach that considers the losses of the back-to-back converters, and it is based on the full-order DFIG model. By assuming known rotor speed, the steady-state calculation problem is formulated using a set of linear equations and only one quadratic equation. Two sets of solutions are obtained for two equilibrium points. The first solution corresponds to a stable equilibrium point, while the other solution will result in an unstable equilibrium point. The proposed

method ignores the limits of the control systems, limiting its application to certain operating conditions where there is no limit hitting.

A challenge in computing the operating condition is the consideration of control limits. In many conditions, converters may hit the control limits, e.g., during voltage dip. Once a limit is reached, the behavior of the control system changes. Considering those limits makes the computing model more sophisticated, yet this is essential for accuracy.

In the literature, [35, 38] try to tackle the challenge. The proposed method employ Newton-Raphson approach to calculate the operating point of the DFIG-based WTs. After each iteration, stator and rotor currents are checked for limits violations. Once a violation is identified, the active and reactive powers of the DFIG are recalculated using the PQ curve proposed in [39], which ignores the converter losses and is based on the assumption $P_r = -sP_s$. In [29], for short circuit studies, a phasor domain model for Type-III WTs, which uses the concept of a control-based equivalent circuit, is proposed. Rotor current limits are taken into consideration; however, current calculations are based on approximation.

Our contribution is that we proposed two methods to compute steady-state operating conditions of Type-III WTs considering the control limits. The proposed methods are applicable for ideal operating conditions and undervoltage scenarios. In the first method, an optimization problem is first formulated to identify the voltage thresholds at which the behavior of the control system changes due to the current limits. An efficient algorithm for steady-state calculations is designed using the identified limits. The problem is formulated as equality and inequality constraints and solved using a non-linear programming solver. In the second method, a one-step algorithm is developed. An efficient algorithm using Mixed Integer non-linear Programming (MINLP) is developed to compute the steady-state operating point of Type-III WTs. For a given stator voltage and wind speed, the electrical and mechanical variables of the system can be computed. A Full-order model of DFIG-based WT is considered. Some overly simplifying assumptions that are commonly adopted in the

literate are avoided. Losses in the back-to-back converters, and nonzero reactive power support through the GSC are taken into account. Compared to state-of-the-art, the proposed methods are much more accurate computation models for DFIG. The proposed methods are validated with electromagnetic transient (EMT) simulations.

1.5.2 Task-B: Analysis of Type-III WTs Subject to Unbalance

With the use of two power electronics converters, the harmonic issue is identified as one of the main issues in the design of Type-III WTs [40]. Severe scenarios in which the entire power system loses its stability may occur when the generated harmonics coincide with the system resonant frequency [41].

Non-sinusoidal rotor injection due to the switching technique in the converter and the non-sinusoidal distribution of the rotor winding are the main sources of harmonics during normal operation conditions, while core saturation and winding faults are other sources caused by abnormal conditions [8, 42–44].

On the stator side, the common sources of harmonics are non-ideal operation conditions, e.g., voltage disturbances, voltage unbalance, and flicker [8, 21, 45–47]. The focus of this task is the effect of grid voltage unbalance on DFIG.

Research has been conducted on grid unbalance from the control perspective and the analysis perspective. From the control perspective, several control designs and improvements [19, 48] have been proposed to overcome the well-known consequences on DFIG due to unbalanced grid voltage, including ripples in torque and active power.

From the analysis perspective, harmonic analysis for DFIGs under unbalanced grid conditions was carried out in 2010 in [8] with the following simplification assumptions. The converter controls are ignored, and it is assumed that the rotor injection voltage magnitude and frequency are constant during the system disturbances. While the research gives insights on DFIG's circuits, the research does not include the effect of converter control.

Converter controls are included in later research, e.g., [49], where a sequence domain-based model of Type-III WT under unbalanced is built considering various control modes. The negative-sequence converter control is modeled as a Norton circuit: a current source in parallel with an impedance. The analysis neglects the double-frequency component in the DC-link voltage, and discards the 3rd harmonic effect. Similarly, the Norton circuit representation is adopted in [50], where a phasor-domain model is developed considering the WT control systems. The WT is represented by a current source, and an iterative method is used to account for the converter control. The proposed method is limited to WTs that contain decoupled sequence control since the negative-sequence currents are assumed to be eliminated.

As an improvement from [50], [51] considers the impact of negative-sequence components in WTs controls. On the other hand, only the inner loop control is considered in the computing. In addition, the method in [51] considers only fundamental components and discards harmonics associated with the unbalanced condition (especially 3rd harmonic).

In summary, none of the aforementioned literature on DFIG under unbalance, e.g., [8, 50, 51], has adequately modeled the 3rd harmonic circuit. Research on 3rd harmonics is only available recently for a grid-following converter [52].

Our contribution is that we adequately model DFIG for unbalanced grid conditions by including not only positive- and negative-sequence circuits but also 3rd harmonic circuits. Compared to a grid-following converter, the circuit of DFIG is much more complicated. An induction machine, a RSC, a GSC, and a dc-link should all be considered in circuit modeling.

Besides the modeling work, we designed an efficient algorithm for steady-state harmonic analysis of Type-III WT subject to unbalance. The latter is achieved by converting the circuit analysis problem to a set of equality constraints and solving the problem using efficient solvers.

1.6 Outline of the Dissertation

The remainder of the chapters are organized as follows:

Chapter 2 presents an accurate method of calculating the operating point of Type-III WTs considering the control impact for balanced stator voltage scenarios. An optimization-based approach is proposed to identify the stator voltage at which the control system fails to achieve its targeted values. Based on the identified values, steady-state calculations are conducted using an advanced computing tool. Results obtained by the proposed algorithm are validated using electromagnetic transient (EMT) simulations.

Chapter 3 presents steady-state harmonic analysis of Type-III WTs subject to unbalanced stator voltage. A phasor-domain model for Type-III WTs is presented to calculate positive-, negative-sequence, and third harmonic components using the concept of control-based equivalent circuits. The analysis is carried out in three stages. In the first stage, the voltage source converters of the rotor-side and grid-side are assumed to operate with a constant modulation index. In the second stage, current control loops are considered. In the third stage, outer control loops are considered. The proposed method is validated with electromagnetic transient (EMT) simulations. In chapter 4, two applications of MIP in power systems are presented. In the first part of the chapter, a MINLP problem is formulated to model the behavior of Type-III WTs considering current limits imposed by the control system. In the second part of the chapter, a MILP problem is formulated to identify faults location, type, and magnitude in distribution feeders. The analysis starts with a simple single-phase network and then extended to unbalanced distribution feeders. The placement of the microPMUs is discussed. Three different feeders with different characteristics are used for validating the proposed algorithm. Chapter 5 concludes the dissertation and presents the future work.

Chapter 2: Steady-State Modeling of Type-III WTs Under Balanced Voltage

2.1 Introduction

This chapter¹ proposes an approach to calculate steady-state operating conditions of DFIG-based WTs considering the control limits. First, optimization problems are formulated to identify the minimal stator voltages that the control system of Type-III WTs can handle before the currents limits are reached. Based on the identified values, steady-state calculations are conducted using an advanced computing tool. Analytical solutions to the steady-state operating conditions for the full-order dynamic model of DFIG-based WTs are provided. Lossy DFIG back-to-back converters are considered. The proposed method is validated with electromagnetic transient (EMT) simulations. The chapter starts with an analysis of a simple squirrel cage induction machine (Testbed-A) in section 2.2. Then, the analysis is extended to Type-III WTs (Testbed-B) in section 2.3. Section 2.4 concludes the chapter.

2.2 Squirrel Cage Induction Machine (Testbed-A)

In this section, steady-state analysis is conducted on a squirrel cage induction machine connected to the grid through a transmission line (shown in Fig .2.1). The system is assumed to operate under a balanced grid voltage condition. Two case studies are conducted on the given system.

¹Part of this chapter is published in our paper [53], 2019. Permissions are included in Appendix A.

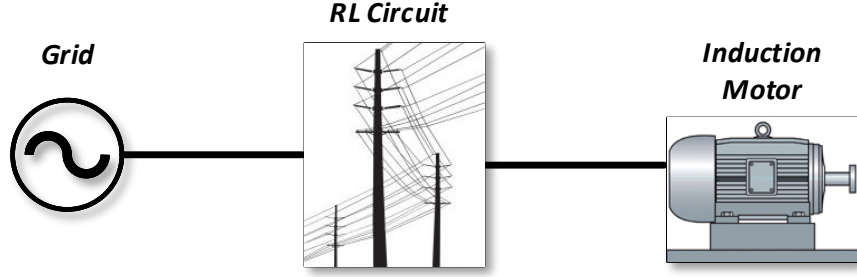


Figure 2.1: System configuration (Testbed-A).

2.2.1 Equivalent Circuits of an Induction Machine

If the circuit connecting the motor to the grid is taken into account (as in Fig .2.1), the positive-sequence circuit will be given in Fig. 2.2. V_t^p is the positive sequence voltage of the motor, V_g^p is the positive sequence voltage of the grid, I_s^p is the stator positive sequence current, I_r^p is the rotor positive sequence current, R_s is the stator resistance, X_s is the stator reactance, R_r is the rotor resistance, X_r is the rotor reactance, R_g is the line resistance, X_g is the line reactance, X_m is the magnetizing reactance, and s is the slip. The core loss is neglected since it is very low compared to the rotor and the stator copper losses.

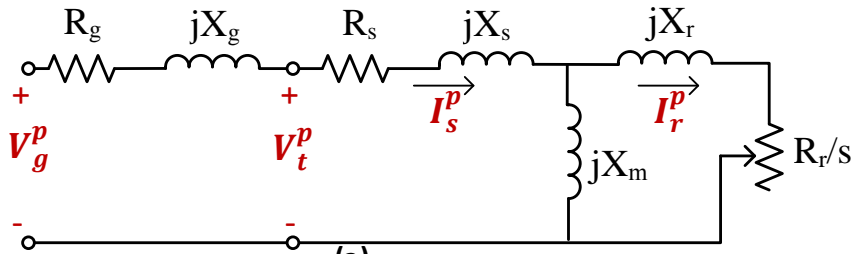


Figure 2.2: Positive-sequence equivalent circuit.

In order to find the five steady-state variables, including stator positive-sequence currents (notated as $I_s^p \angle \phi_s^p$), rotor positive-sequence currents, (notated as $I_r^p \angle \phi_r^p$) and machine slip (notated as s) for the system in Fig .2.1 for a given grid voltage and motor torque, five equations should be considered. Difficulties are introduced due to the non-linearity of these equations. In section 2.2.2, a detailed formulation is provided to solve the problem through

an advanced computing tool (YALMIP [54]). The equivalent circuit can be expressed by two equations, shown in (2.1).

$$-V_g^p \angle \theta_g^p + (R_s + R_g + j(X_s + X_m + X_g))I_s^p \angle \phi_s^p - jX_m I_r^n \angle \phi_r^n = 0 \quad (2.1a)$$

$$\left(\frac{R_r}{s} + j(X_r + X_m) \right) I_r^p \angle \phi_r^p - jX_m I_s^p \angle \phi_s^p = 0 \quad (2.1b)$$

Further, the voltage of the motor terminals can be found:

$$V_t^p \angle \theta_g^p = -V_g^p \angle \theta_g^p + (R_m + j(X_s))I_s^p \angle \phi_s^p \quad (2.2)$$

The air gap power developed by the positive sequence components is given in (2.3).

$$P_{ag}^p = 3(I_r^p)^2 \frac{R_r}{s} \quad (2.3)$$

The electromagnetic torque of the motor is given in (2.4).

$$T_{em}^p = \frac{\text{poles}}{2} \frac{P_{ag}^p}{\omega_e} \quad (2.4)$$

$$T_{em} = T_{em}^p = \frac{\text{poles}}{2} \frac{3R_r}{\omega_e} \left[\frac{(I_r^p)^2}{s} \right]$$

ω_e is stator angular frequency.

2.2.2 Steady-State Calculations

Expressions (2.1), related to the motor circuits, constitute two complex algebraic equations that can be separated into four real algebraic equations (2.5a-2.5d). Expression (2.5e) is related to the torque requirement. Suppose the grid voltage and motor torque are given. In that case, there are five unknown state variables, magnitudes, and angles of rotor and stator positive-sequence currents and the slip rate. The five unknown quantities of the motor can

be found by solving the five equations (2.5a-2.5e) using any well-known iterative way such as Newton-Ralphson. In this paper, YALMIP is used to solve the nonlinear set of equations through a nonlinear programming solver `fmincon`. Once the stator currents are found, the terminal voltages of the motor can be found using (2.2).

$$f_1 = -V_g^p \cos \theta_g^p + (R_s + R_g)I_s^p \cos \phi_g^p + X_m I_r^p \sin \phi_r^p - (X_s + X_m + X_g)I_s^p \sin \phi_s^p = 0 \quad (2.5a)$$

$$f_2 = -V_g^p \sin \theta_g^p + (R_s + R_g)I_s^p \sin \phi_g^p - X_m I_r^p \cos \phi_r^p + (X_s + X_m + X_g)I_s^p \cos \phi_s^p = 0 \quad (2.5b)$$

$$f_3 = \frac{R_r}{s} I_r^p \cos \phi_r^p - (X_r + X_m)I_r^p \sin \phi_r^p + X_m I_s^p \sin \phi_s^p = 0 \quad (2.5c)$$

$$f_4 = \frac{R_r}{s} I_r^p \sin \phi_r^p + (X_r + X_m)I_r^p \cos \phi_r^p - X_m I_s^p \cos \phi_s^p = 0 \quad (2.5d)$$

$$f_5 = T_{em} \frac{2\omega_e}{p} - 3I_r^2 \left[\frac{R_r}{s} \right] = 0 \quad (2.5e)$$

2.2.3 Case Study 1: State Variables Calculations

In order to validate the proposed method in the previous sections, a testbed of an induction motor served by a voltage source is simulated in MATLAB/SimPowerSystems environment, as shown in Fig .2.3. The motor is connected to the grid bus through an RL circuit. The model parameters are shown in Table 2.1. In Table 2.2, the simulation results

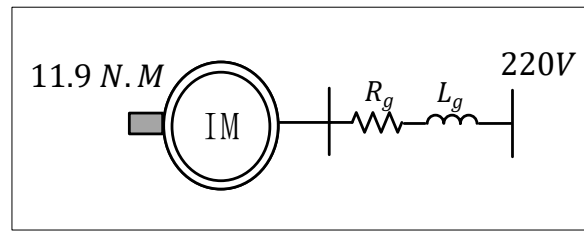


Figure 2.3: EMT model configuration (Testbed-A).

are compared with the results using the proposed method described in the previous section. The input values to the optimization problem are the grid voltage (220V or 1 p.u) and the load Torque (11.9 N.m).

Table 2.1: Parameters of Simulink model (Testbed-B)

R_s	0.435(Ω)	friction factor	0
R_r	0.816(Ω)	pole pairs	2
L_s	4.0(mH)	Inertia	0.089
L_r	2.0(mH)	T_{mech}	11.9($N.m$)
L_m	69.31(mH)	V	220(60Hz)
R_g	0.1(Ω)	HP	3
L_g	1(mH)		

Table 2.2: Motor Variables

	Simulation	Proposed method
$I_s^p \angle \phi_s^p$	11.35 \angle - 39.91	11.35 \angle - 39.91
$V_t^p \angle \theta_t^p$	176.03 \angle - 0.831	176.03 \angle - 0.831
s	0.0466	0.0467
$I_r^p \angle \phi_r^p$	9.255 \angle - 6.913	9.255 \angle - 6.912

2.2.4 Case Study 2: Minimal Grid Voltage a Motor Can Handle

A grid voltage drop may cause a motor stall. In this case study, we examine the minimal grid voltage a motor can handle for a given load torque. When the grid voltage dips, the motor voltage can be decreased as long as the steady-state equations in (2.5a-2.5e) can be satisfied. Once these equations are not satisfied, the motor will lose its stability. In Fig. 2.1, the grid voltage decreases at $t = 1.5$ s. As a result, the stator current increases to meet the load requirement. At $t = 3$ s, the grid voltage dropped to less than the minimum voltage that the motor can handle which causes stability issues. In order to find the minimal grid voltage the system can handle for a given torque, the optimization problem is formulated as in (2.6). The objective function will be the minimization of the grid voltage. The constraints of the optimization problem are the steady-state circuit and torque equations (2.5a-2.5d), the slip and angle limits. The input value to the optimization problem is the load torque of the

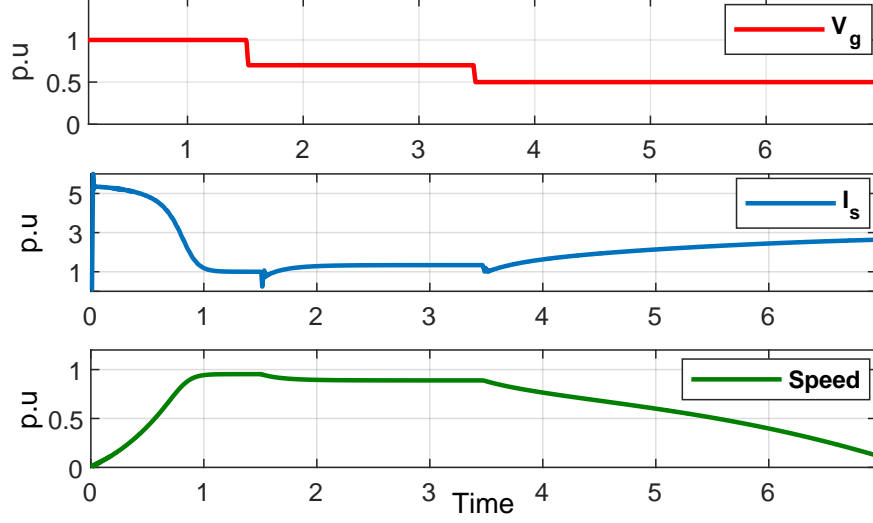


Figure 2.4: Induction motor response to change in voltage.

motor and, the decision variables are the stator, rotor currents, and the slip ($I_s^p, I_r^p, \phi_s^p, \phi_r^p, s$).

$$\begin{aligned}
 & \text{Minimize}(V_g^p) \\
 & \text{Subject to (2.5a} - 2.5d) \\
 & T_{\text{Load}} \frac{2\omega_e}{\text{Poles}} - 3I_r^{p2} \left[\frac{R_r}{s} \right] = 0 \quad (2.6) \\
 & 1 \geq s \geq 0 \\
 & \pi \geq \phi_s^p, \phi_r^p \geq -\pi
 \end{aligned}$$

By solving (2.6) for the given motor in Table 2.1, the minimal grid voltage the motor can handle for 11.9 N.m load torque is 102 V (phase voltage). Fig. 2.5b shows the motor speed response to the change in grid voltage shown Fig. 2.5a. In Case A, the grid voltage is set 1 V below the threshold at $t = 1.5$ s while it is above the threshold by 1V in Case B. It can be seen that, the motor becomes unstable when the grid voltage is below the boundary found by the proposed method.

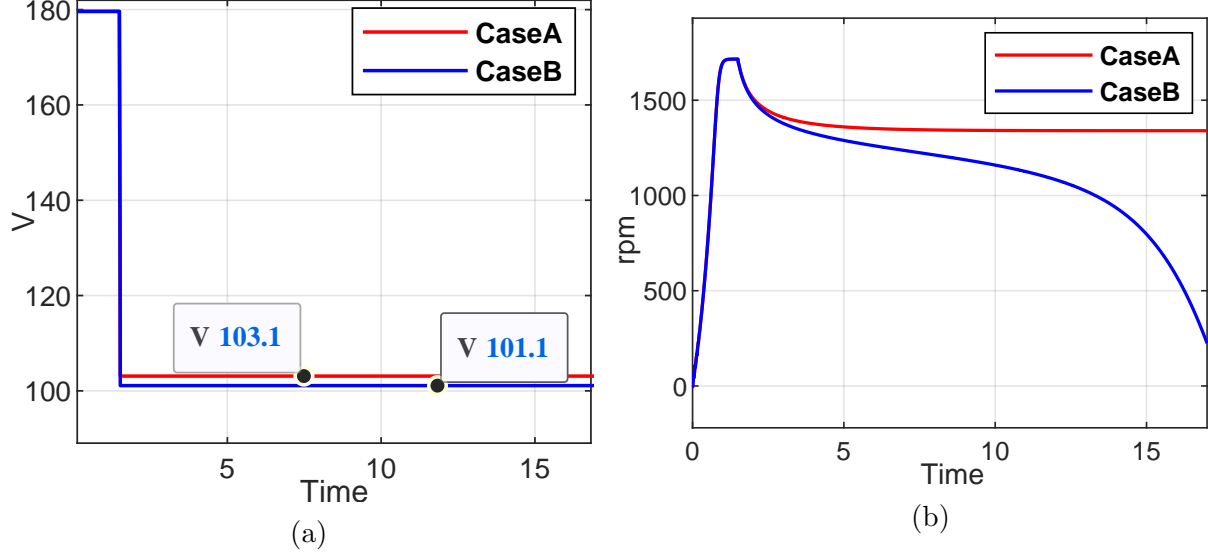


Figure 2.5: Motor response. (a) Grid voltage. (b) Motor speed.

2.3 Type-III Wind Turbine (Testbed-B)

The typical configuration of a DFIG-based WT is shown in Fig .2.6. In Type-III WTs, the stator of the induction machine (IM) is directly connected to the grid, and the wound rotor is connected to the grid through a Back-to-Back converter. The Back-to-Back converter consists of two three-phase PWM converters, Rotor-Side Converter (RSC) and Grid-Side Converter (GSC), which is connected to the grid through an AC filter. The two converters are coupled through a common DC link. i_s, i_r and i_g are the DFIG stator, rotor, and grid-side converter current, respectively. v_s, v_r and v_g are terminal voltage of the DFIG stator, rotor, and grid side-converter. P and Q are the DFIG-base WT real and reactive power outputs. R_g and X_g are the resistance and reactance of the DFIG back-to-back converter. C_{dc} is the DC-link capacitance of the DIFG back-to-back converter. P_m is the mechanical power.

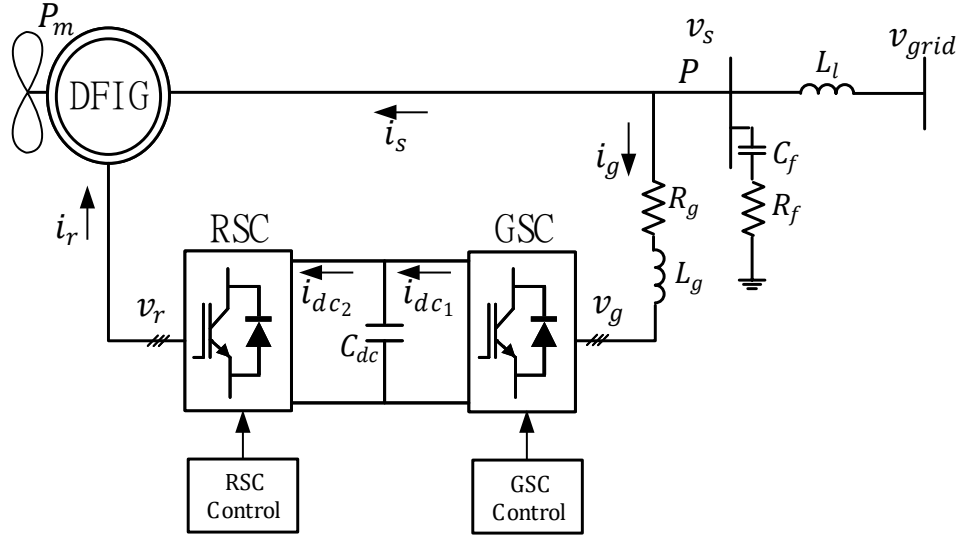


Figure 2.6: System configuration (Testbed-B).

2.3.1 Steady-State DFIG-Based WT Model

2.3.1.1 DFIG Equivalent Circuit

At steady-state, the electrical equivalent circuit of the DFIG in dq -frame (shown in Fig .2.7 can be expressed by the following equations.

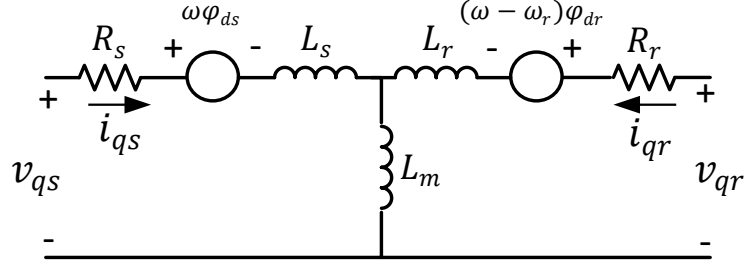
$$v_{qs} - R_s i_{qs} - (X_s + X_m) i_{ds} - X_m i_{dr} = 0 \quad (2.7a)$$

$$v_{ds} + (X_s + X_m) i_{qs} - R_s i_{ds} + X_m i_{qr} = 0 \quad (2.7b)$$

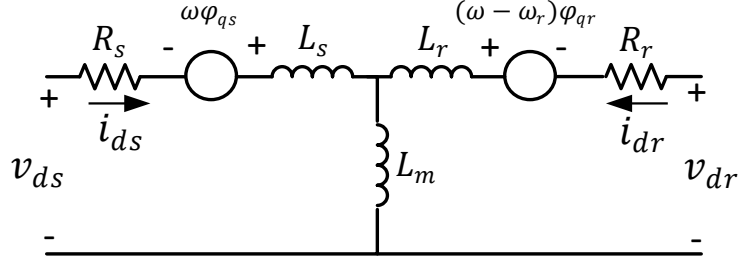
$$v_{qr} - s X_m i_{ds} - R_r i_{qr} - s(X_r + X_m) i_{dr} = 0 \quad (2.7c)$$

$$v_{dr} + s X_m i_{qs} + s(X_r + X_m) i_{qr} - R_r i_{dr} = 0 \quad (2.7d)$$

i_{ds}, i_{qs}, v_{ds} and v_{qs} are DFIG stator currents and voltages on d and q axes, respectively. i_{dr}, i_{qr}, v_{dr} and v_{qr} are DFIG rotor current and voltage on d and q axes, respectively. R_s and R_r are the resistance and reactance of the DFIG rotor and stator circuits, respectively. X_s



(a)



(b)

Figure 2.7: Equivalent circuit of the DFIG. (a) q axis. (b) d axis.

and X_r are reactance of the DFIG rotor and stator circuits, respectively. X_m is the DFIG mutual reactance. s is the slip.

2.3.1.2 Power Equations

According to the power conservation theorem, the mechanical power, which is the power extracted from the wind by the WT, is equal to the sum of rotor and stator active power and losses. The power balance equations can be written in terms of the electrical variables as the following:

$$-P - i_{dg}^2 R_g - i_{qg}^2 R_g - i_{ds}^2 R_s - i_{qs}^2 R_s - i_{dr}^2 R_r - i_{qr}^2 R_r + P_m = 0 \quad (2.8a)$$

$$P + v_{ds} i_{ds} + v_{qs} i_{qs} + v_{ds} i_{dg} + v_{qs} i_{qg} = 0 \quad (2.8b)$$

$$k_p c_p W_{\text{wind}}^3 - P_m = 0 \quad (2.8c)$$

W_{wind} is the wind speed in per unit of the base wind speed. c_p is the performance coefficient in per unit. k_p is the power gain for $c_p = 1$ p.u and $W_{\text{wind}} = 1$ p.u. i_{dg} and i_{qg} are the grid-side-converter current on d and q axes, respectively. The dynamics of the DC-link between the rotor and grid-side converter can be represented by the following equation:

$$C_{dc}v_{dc}\frac{dv_{dc}}{dt} = P_g - P_r \quad (2.9)$$

$$\begin{aligned} \text{where } P_g &= v_{qg}i_{qg} + v_{dg}i_{dg} \\ P_r &= v_{qr}i_{qr} + v_{dr}i_{dr} \end{aligned}$$

At a steady-state and three-phase balanced condition, the equation in (2.9) can be rewritten considering the active losses of the GSC as the following:

$$-v_{qs}i_{qg} - v_{ds}i_{dg} + v_{qr}i_{qr} + v_{dr}i_{dr} + i_{dg}^2R_g + i_{qg}^2R_g = 0 \quad (2.10)$$

v_{dg} and v_{qg} are the GSC voltages on d and q axes, respectively.

2.3.2 Control System

The RSC control system implemented in this chapter is shown in Fig. 2.8. θ_m is the rotor mechanical angle, and θ_e is the rotor electrical angle. The control of RSC is achieved using a two-level controller: fast inner loops and slow outer loops. The inner loops are used to calculate the voltage references in order to generate the modulation index. The slow outer loops are used to calculate the current references i_{dr}^* and i_{qr}^* . In the given control system, the outer loops are used to regulate the electromagnetic torque (T_{em}) and the stator reactive power (Q_s). The two controls are implemented by referring all the AC quantities to a synchronous reference frame oriented with the stator voltage as adopted in [55]. That is $v_{ds} = |\overline{V}_s|$ and $v_{qs} = 0$.

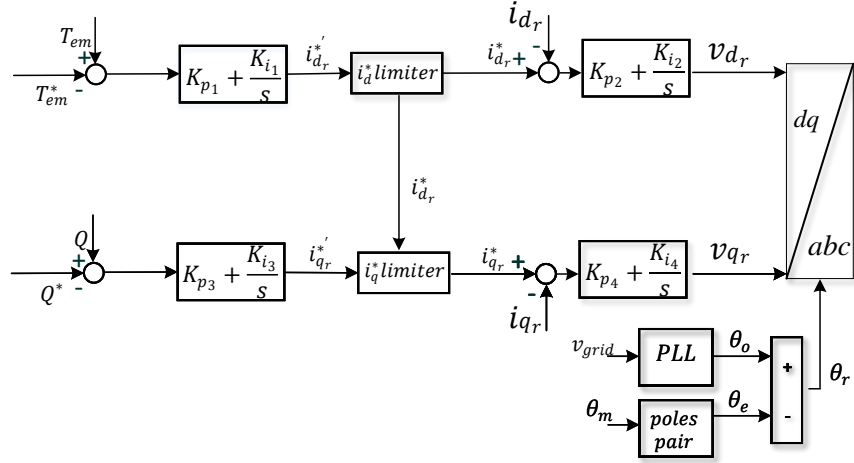


Figure 2.8: RSC control.

A similar technique is used for the GSC controls, as shown in Fig. 2.9. The outer loop of the control is set to regulate the DC-link capacitor voltage (V_{dc}) and reactive power (Q_g).

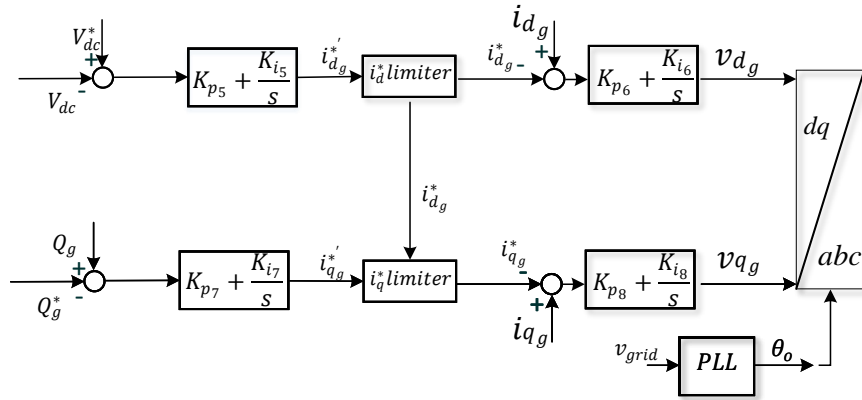


Figure 2.9: GSC control.

2.3.2.1 Converters Currents Limits

In order to avoid overcurrent scenarios that may damage the converters, currents limiters are imposed. The control system should follow the outer loop references as long as the current limits are not reached. Once the limits are hit, following the references is not guaranteed. For a grid-connected DFIG, scenarios where converters hit the limits may occur. During

such scenarios, the control system should give priority to either the active or reactive power. The control system will try to keep the prioritized quantity unchanged. The un-prioritized quantity will be changed and will not track reference due to the current limits.

In this chapter, The RSC and GSC current limiters give priority to active currents based on equations (2.11-2.14). When the LVRT mode is activated, the priority for the RSC is switched from the active to the reactive current, and the controller is switched from the Q-control to a proportional V-control to fulfill the grid code requirement regarding voltage support during voltage disturbances.

$$i_{dr}^* = \begin{cases} i_{dr}^{*'}, & \text{if } -I_r^{\text{limit}} \leq i_{dr}^{*'} \leq I_r^{\text{limit}} \\ I_r^{\text{limit}}, & \text{if } I_r^{\text{limit}} < i_{dr}^{*'} \\ -I_r^{\text{limit}}, & \text{if } -I_r^{\text{limit}} > i_{dr}^{*'} \end{cases} \quad (2.11)$$

$$i_{qr}^* = \begin{cases} i_{qr}^{*'}, & \text{if } \sqrt{i_{dr}^{*2} + i_{qr}^{*2}} \leq I_r^{\text{limit}} \\ \sqrt{I_r^{\text{limit}} - i_{dr}^{*2}}, & \text{if } \sqrt{i_{dr}^{*2} + i_{qr}^{*2}} > I_r^{\text{limit}}, i_{qr}^{*'} > 0 \\ -\sqrt{I_r^{\text{limit}} - i_{dr}^{*2}}, & \text{if } \sqrt{i_{dr}^{*2} + i_{qr}^{*2}} > I_r^{\text{limit}}, i_{qr}^{*'} < 0 \end{cases} \quad (2.12)$$

$$i_{dg}^* = \begin{cases} i_{dg}^{*'}, & \text{if } -I_g^{\text{limit}} \leq i_{dg}^{*'} \leq I_g^{\text{limit}} \\ I_g^{\text{limit}}, & \text{if } I_g^{\text{limit}} < i_{dg}^{*'} \\ -I_g^{\text{limit}}, & \text{if } -I_g^{\text{limit}} > i_{dg}^{*'} \end{cases} \quad (2.13)$$

$$i_{qg}^* = \begin{cases} i_{qg}^{*'}, & \text{if } \sqrt{i_{dg}^{*2} + i_{qg}^{*2}} \leq I_g^{\text{limit}} \\ \sqrt{I_g^{\text{limit}} - i_{dg}^{*2}}, & \text{if } \sqrt{i_{dg}^{*2} + i_{qg}^{*2}} > I_g^{\text{limit}}, i_{qg}^{*'} > 0 \\ -\sqrt{I_g^{\text{limit}} - i_{dg}^{*2}}, & \text{if } \sqrt{i_{dg}^{*2} + i_{qg}^{*2}} > I_g^{\text{limit}}, i_{qg}^{*'} < 0 \end{cases} \quad (2.14)$$

2.3.2.2 Controller Target

The control scheme of the GSC is set to regulate the DC-link voltage and reactive power. At a steady-state and normal operation condition (no limits hitting), the following equation is satisfied:

$$-v_{ds}i_{qg} - Q_g^* = 0 \quad (2.15)$$

When the GSC hits the limit ($\sqrt{i_{dg}^2 + i_{qg}^2} = I_g^{\text{limit}}$), the control system will aim to minimize the error of equation (2.16) based on the maximum allowable reactive current value obtained by equation (2.14).

$$-v_{ds}i_{qg} - Q_g^* = \text{error} \quad (2.16)$$

Similarly, the control system of the RSC is set to regulate the electromagnetic torque and reactive power. At nominal steady-state operating conditions, the following equations are satisfied:

$$X_m(i_{qs}i_{dr} - i_{ds}i_{qr}) - T_{em}^* = 0 \quad (2.17a)$$

$$-v_{ds}i_{qs} - Q_s^* = 0 \quad (2.17b)$$

When the rotor current hit the limit ($\sqrt{i_{dr}^2 + i_{qr}^2} = I_r^{\text{limit}}$), the controller will act to minimize the error of equations (2.18a, 2.18b) based on maximum allowable active and reactive current value obtained by equation (2.11-2.12).

$$X_m(i_{qs}i_{dr} - i_{ds}i_{qr}) - T_{em}^* = \text{error} \quad (2.18a)$$

$$-v_{ds}i_{qs} - Q_s^* = \text{error} \quad (2.18b)$$

2.3.2.3 Control Modes

In this section, the control system operating condition will be categorized into different operation modes as a function of the stator voltage.

For the RSC controller, If the LVRT function is ignored, there are three possible operating modes the system can operate in.

- Mode-A ($V_{t_1}^r \leq |\overline{V}_s|$): In this mode, the control system is able to track the electromagnet torque (T_{em}^*) and the reactive power (Q_s^*) references as the rotor current is still within its limit ($\sqrt{i_{dr}^{*2} + i_{qr}^{*2}} \leq I_r^{limit}$).
- Mode-B ($V_{t_2}^r \leq |\overline{V}_s| < V_{t_1}^r$): In this mode, the rotor current will hit its limit ($\sqrt{i_{dr}^{*2} + i_{qr}^{*2}} = I_r^{limit}$). As the priority in the adopted design is given to the active current, the control system will keep tracking the torque reference (T_{em}^*). However, it will not be able to satisfy the reactive power requirement (Q_s^*).
- Mode-C ($0 \leq |\overline{V}_s| < V_{t_2}^r$): In this mode, i_{dr} will hit the limit $\pm I_r^{limit}$, and i_{qr} will be zero. The control system will not be able to track the torque or the reactive power references.

Similarly, for the GSC controller, there are three possible operating modes the system can operate in.

- Mode-A ($V_{t_1}^g \leq |\overline{V}_s|$): In this mode, the control system is able to track the DC-link voltage (V_{dc}^*) and the reactive power Q_g^* references as the GSC current is still within its limit ($\sqrt{i_{dg}^{*2} + i_{qg}^{*2}} < I_g^{limit}$).
- Mode-B ($V_{t_2}^g \leq |\overline{V}_s| < V_{t_1}^g$): In this mode the GSC current will hit its limit ($\sqrt{i_{dg}^{*2} + i_{qg}^{*2}} = I_g^{limit}$). As the priority in the adopted design is given to the active current, the control system will keep tracking the the DC-link voltage reference (V_{dc}^*). However, it will not be able to satisfy the reactive power requirement (Q_g^*).

- Mode-C ($0 \leq |\bar{V}_s| < V_{t_2}^g$): In this mode, i_{dg} will hit the limit $\pm I_g^{limit}$ and i_{qg} will be zero. The control system will not be able to track the DC-link voltage or the reactive power references.

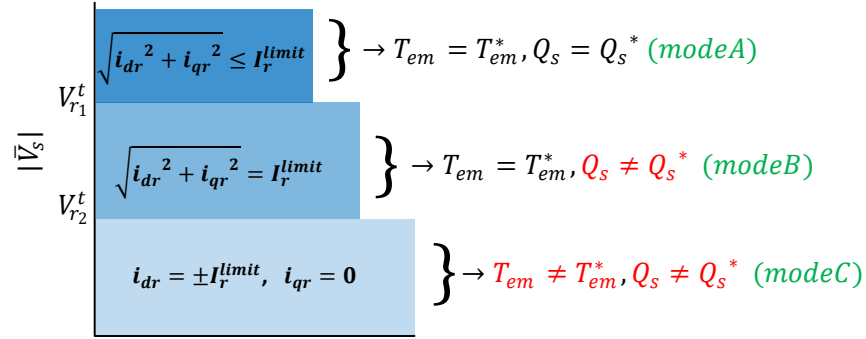


Figure 2.10: RSC control modes.

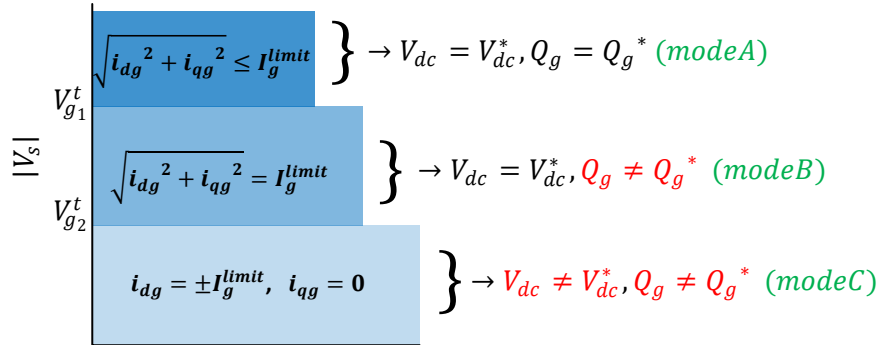


Figure 2.11: GSC control modes.

2.3.3 Voltage Thresholds Identification

In this section, optimization problems are formulated and solved to identify the voltage thresholds at which the control system's behavior changes due to hitting the current limits. The proposed algorithm is shown in Fig. 2.12. The LVRT function is not considered in this section. A set of optimization problems are formulated to have (2.11-2.14) incorporated as constraints. The objective function of the optimization problems is the minimization of the

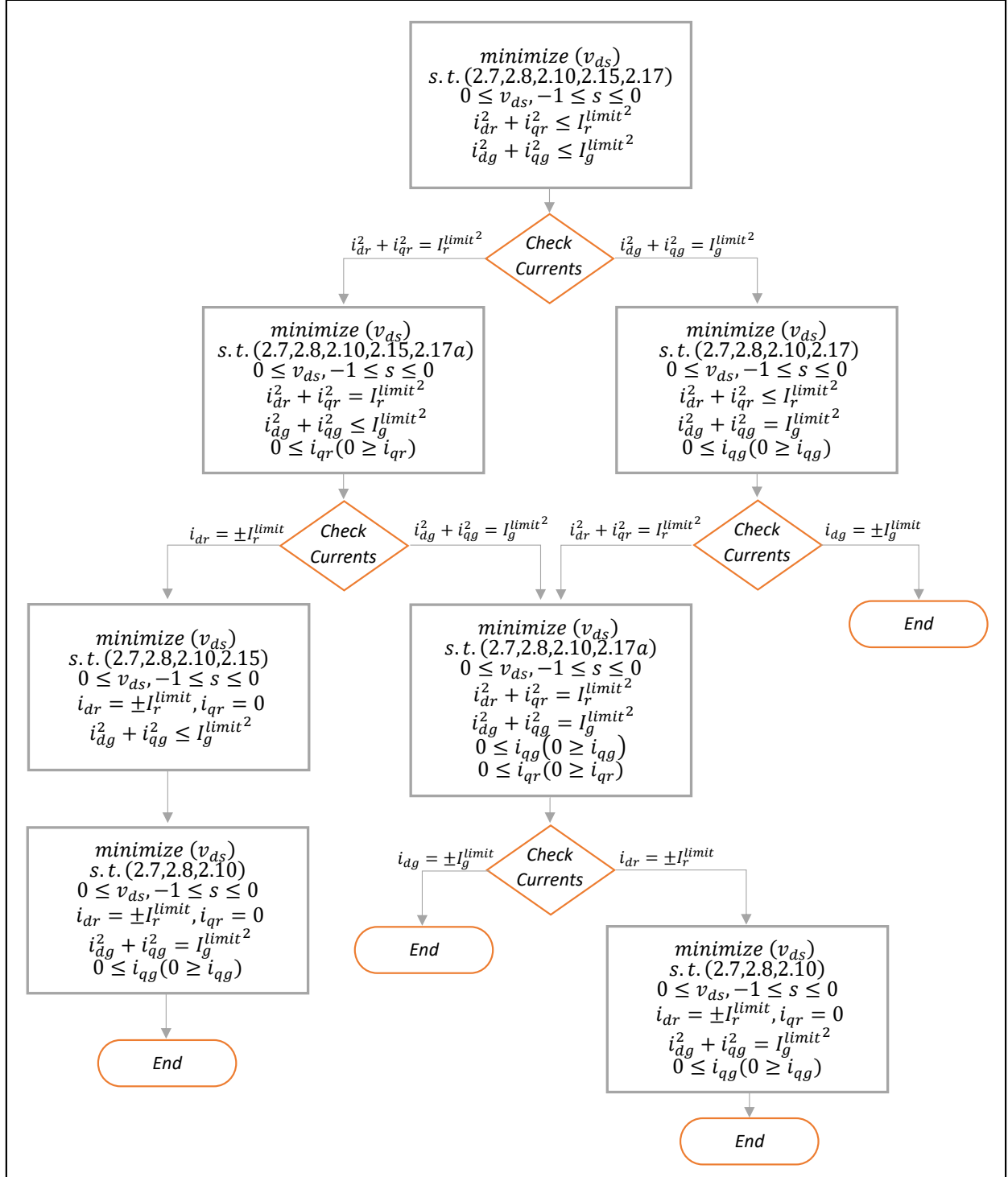


Figure 2.12: Proposed algorithm.

stator voltage. Besides the current limits, the equality constraints include the steady-state circuit, power, torque, and control equations (2.7, 2.8, 2.10, 2.15, and 2.17). The decision variables are $(i_{ds}, i_{qs}, i_{dr}, i_{qr}, i_{dg}, i_{qg}, v_{dr}, v_{qr}, s, P, P_m)$. The constraints of the following optimization problems change according to the current limit that is being hit. As the RSC and GSC current limiters prioritize active currents, i_{qr} and i_{qg} will hit the limit always before i_{dr} and i_{dg} reach their limits.

The algorithm starts by solving the main optimization problem to identify the first minimum voltage threshold V_{t1} for the region where the RMS values of the RSC current and the GSC currents are within the limit. Once the first optimization problem is solved, the first voltage threshold is identified. Then, the currents obtained from solving the optimization problem are checked to identify which converter reached the limit. Based on this information, another optimization problem is formulated to find the second voltage threshold V_{t2} . The signs of the currents (e.g. $i_{qr} \leq 0$ or $i_{qr} \geq 0$) are obtained from the solution of the previous optimization problem.

For example, if the results obtained from solving the main (first) optimization problem indicate that the RSC reached the limit ($\sqrt{i_{dr}^2 + i_{qr}^2} = I_r^{\text{limit}}$) and the sign of the reactive current is negative ($i_{qr} \leq 0$), the new optimization problem which aims to find the second voltage threshold (V_{t2}) will be formulated as in (2.19). Please note that the inequality constraint ($\sqrt{i_{dr}^{*2} + i_{qr}^{*2}} \leq I_r^{\text{limit}}$) is replaced with the equality constraint ($\sqrt{i_{dr}^{*2} + i_{qr}^{*2}} = I_r^{\text{limit}}$), and the equality constraint ($-v_{ds}i_{qs} - Q_s^* = 0$) is replaced with the inequality constraint ($i_{qr} \leq 0$). Now, the third optimization problem which aims to find the third voltage threshold (V_{t3}) will be formulated based on the information obtained from solving the optimization problem in (2.19). One of two scenarios may occur based on the solution of (2.19): RSC active current limit hitting ($i_{dr}^2 = \pm I_r^{\text{limit}}$) or GSC current limit hitting ($\sqrt{i_{dg}^2 + i_{qg}^2} = I_g^{\text{limit}}$).

$$\begin{aligned}
& \text{minimize} && (v_{ds}) \\
& \text{subject to} && (2.7, 2.8, 2.10, 2.15, 2.17a) \\
& && i_{qr}^2 + i_{gr}^2 = I_r^{limit^2} \\
& && i_{qg}^2 + i_{gg}^2 \leq I_g^{limit^2} \\
& && i_{qr} \leq 0 \\
& && -1 \leq s \leq 0
\end{aligned} \tag{2.19}$$

The algorithm ends once the GSC is not able to track the DC-link voltage. For the adopted control scheme, the DC-link voltage keep increasing once the active current in the GSC hits the limits as no protection scheme is adopted on the DC-link. The wind turbine is assumed to not operate in this region, so no calculations were conducted. This case will be addressed in future research.

2.3.3.1 Validation of the Voltage Thresholds

By solving the proposed algorithm for the given system in Table 2.3, the following sequence is identified.

Table 2.3: Parameters of Simulink model (Testbed-B)

R_s	0.023(p.u)	friction factor	0	X_g	0.3(p.u)
R_r	0.016(p.u)	pole pairs	3	R_g	0.003(p.u)
X_s	0.18(p.u)	Inertia	0.0685 s	C_{dc}	0.01 (F)
X_r	0.16(p.u)	S_n	1.5 (MVA)	V_{dc}	1150 V
X_m	2.9(p.u)	V_n	575 V	Q_s^*	-0.2(p.u)
I_r^{limit}	1(p.u)	I_g^{limit}	0.2(p.u)	Q_g^*	-0.1(p.u)
W_{wind}	11 m/s (1 p.u)	T_{em}^*	-0.63(p.u)	f_n	60 Hz
c_1	0.6450	c_2	116	c_3	0.4
c_4	5	c_5	21	c_6	0.00912
c_7	0.08	c_8	0.035		

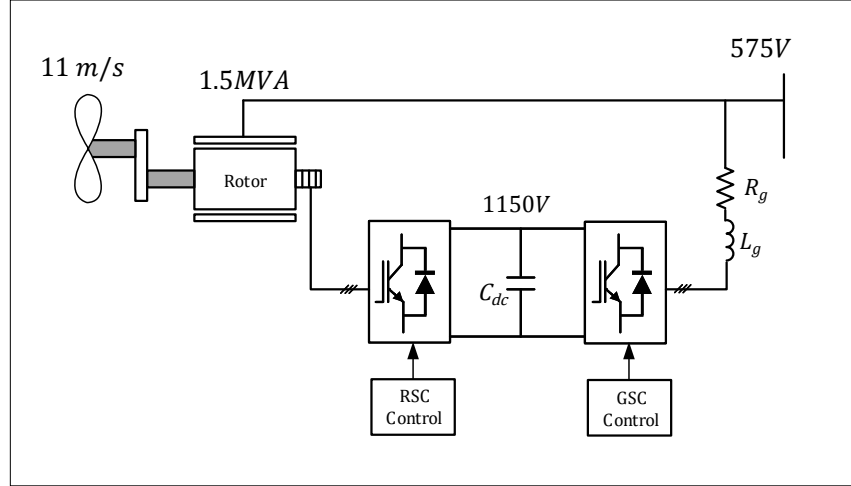


Figure 2.13: EMT model configuration (Testbed-B).

- For $|\bar{V}_s| < V_{t1}$, the reactive current of the RSC converter i_{qr} will reach the limit so that the RSC control will not be able to track the reactive power reference Q_s^* . ($V_{t1} = 0.777$).
- For $|\bar{V}_s| < V_{t2}$, the reactive current of the GSC converter i_{qg} will reach the limit so that the GSC control will not track the reactive power reference Q_g^* . ($V_{t2} = 0.720$).
- For $|\bar{V}_s| < V_{t3}$, the active current of the RSC converter i_{qr} will reach the limit so that the RSC control will not track the torque reference T_{em}^* . ($V_{t3} = 0.647$).
- For $|\bar{V}_s| < V_{t4}$, the active current of the GSC converter i_{dg} will reach the limit so that the GSC control will lose tracking the DC-link voltage reference V_{dc}^* . ($V_{t4} = 0.624$).

The optimization problems are solved by YALMIP through nonlinear programming solver Ipopt. To validate the analysis conducted in the previous section, a testbed of Type-III WT model is simulated in MATLAB/SimPowerSystems (2020), as shown in Fig .2.19. The stator voltage is dipped 0.01 p.u above and below each calculated threshold to prove the change that happens in the system crossing these thresholds. The EMT results are shown in Fig .2.14-Fig .2.17.

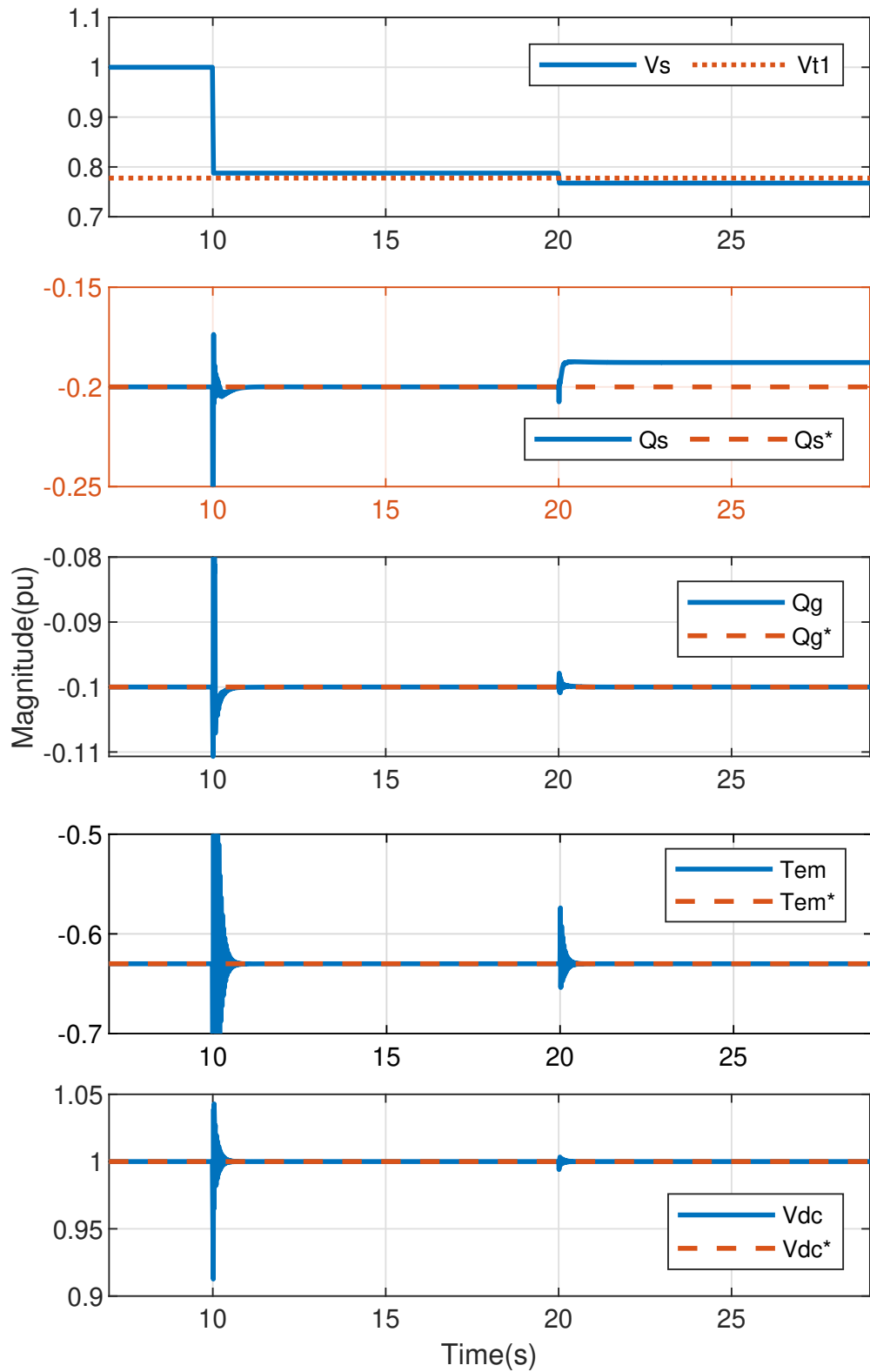


Figure 2.14: System response to changes in the voltage (Case-A). The stator voltage dropped below V_{t1} at $s = 20$, so the RSC control system could not track the reactive power reference Q_s^* .

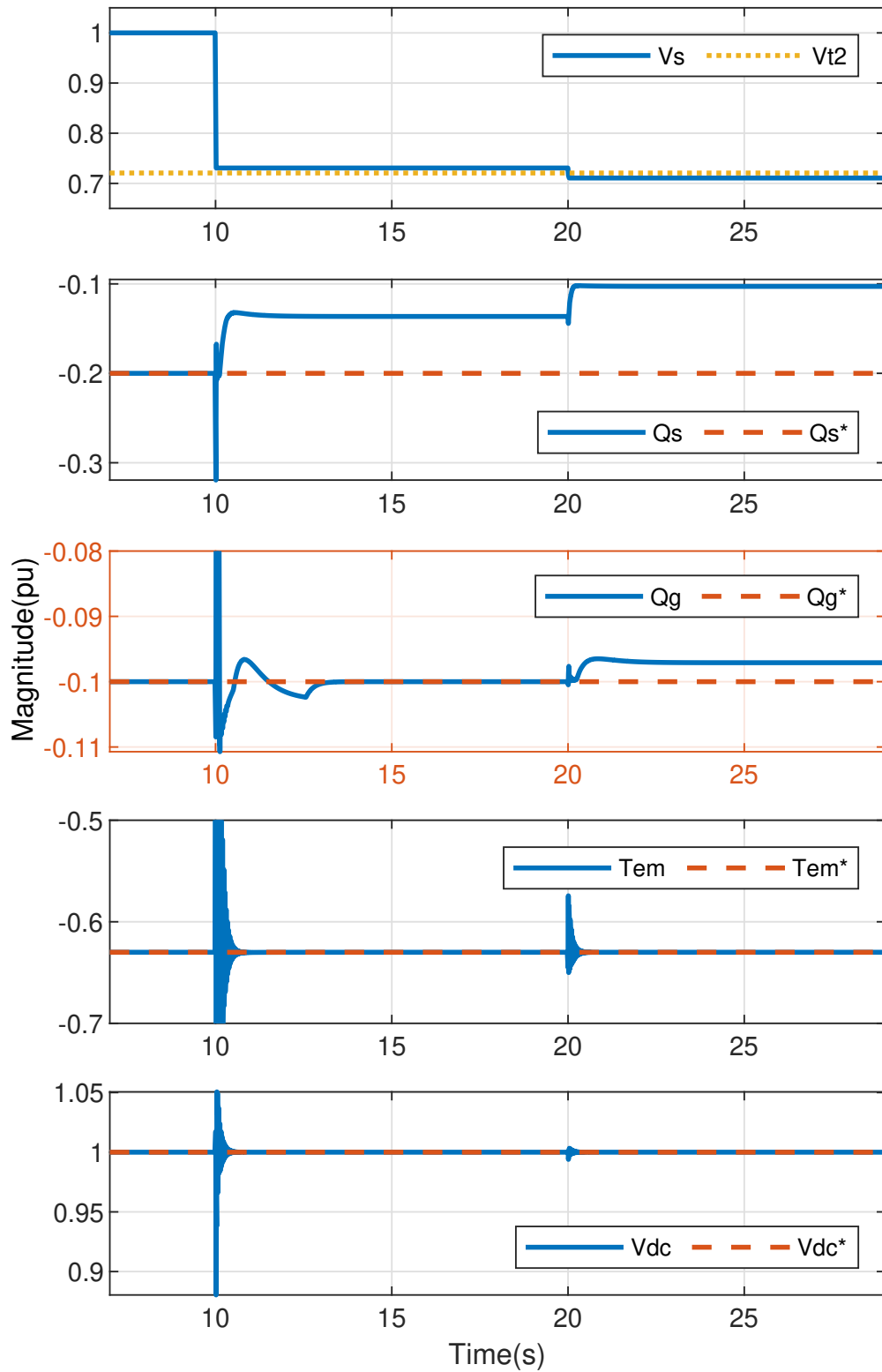


Figure 2.15: System response to changes in the voltage (Case-B). The stator voltage dropped below V_{t2} at $s = 20$, so the GSC control system could not track the reactive power reference Q_g^* .

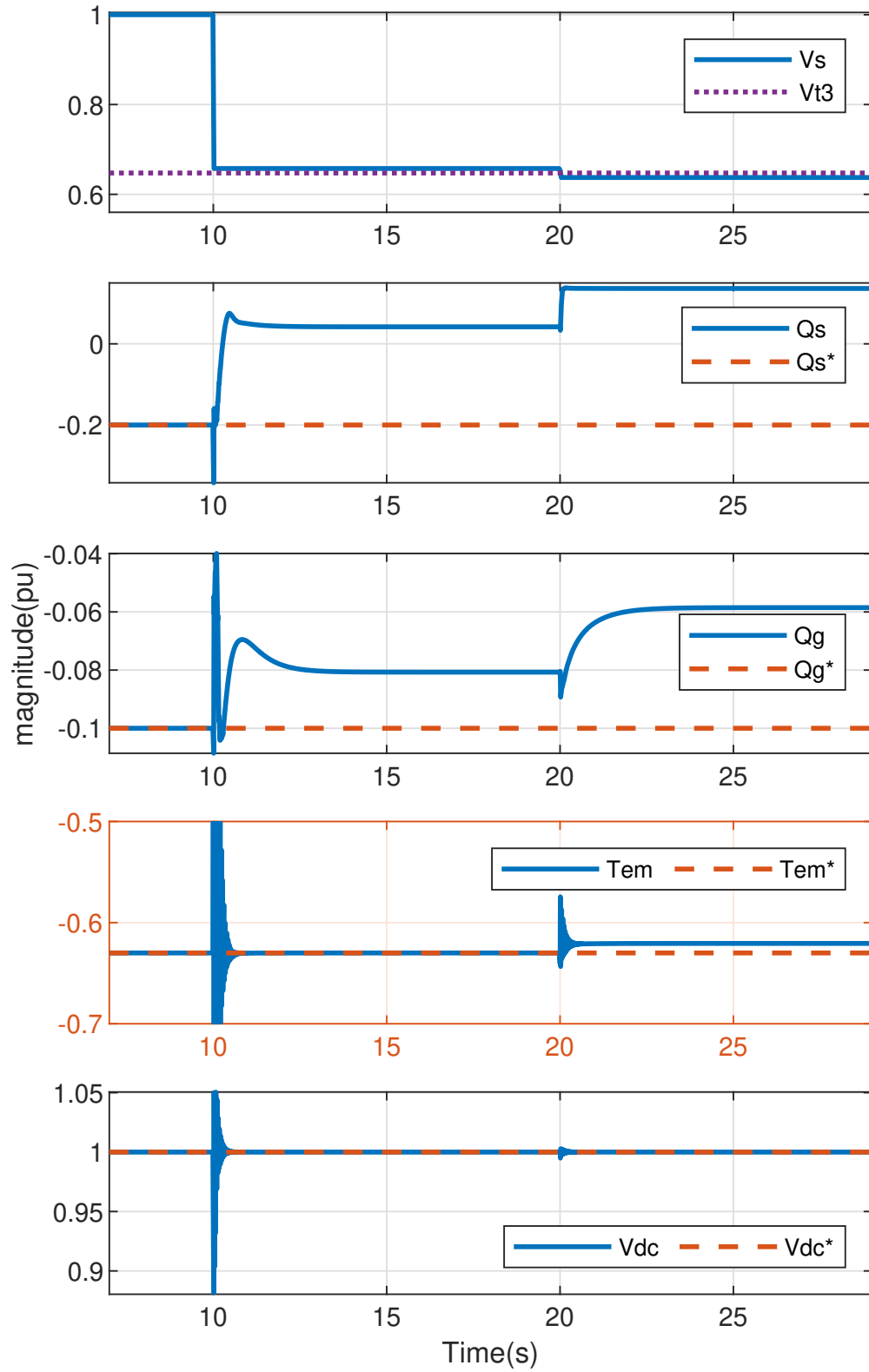


Figure 2.16: System response to changes in the voltage (Case-C). The stator voltage dropped below V_{t3} at $s = 20$, so the RSC control system could not track the electromagnetic torque reference T_{em}^* .

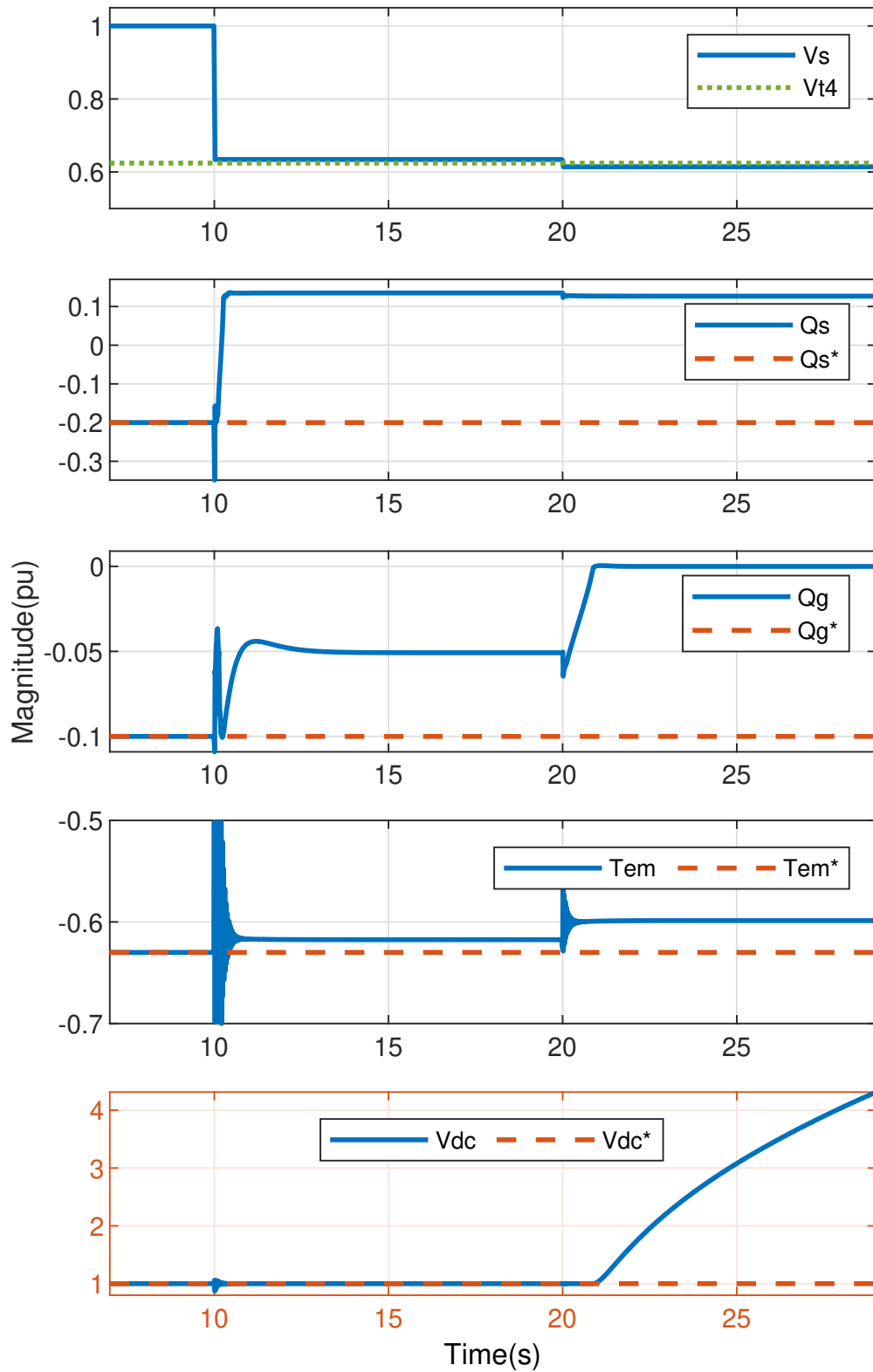


Figure 2.17: System response to changes in voltage (Case-D). The stator voltage dropped below V_{t4} at $s = 20$, so the GSC control system could not track the DC-link voltage reference V_{dc}^* .

2.3.4 Calculating Steady-State Operating Conditions for Type-III WT

In order to solve the steady-state calculation problem, known variables (system inputs) and unknown variables should be identified. In this section, it is assumed that the wind speed is known. The bus voltage \bar{V}_s is obtained from a valid power flow solution for the studied system before the steady-state calculations of the DFIG, similar to the assumption adopted in [32]. This assumption is made as this paper aims to improve the method of solving the sub-problem of calculating the steady-state of DFIG-based WTs. The power flow problem is addressed in [29, 38, 51] through an iterative process. After the stator voltage \bar{V}_s is obtained from the power flow solution, the problem is solved with the synchronous reference frame linked to the stator voltage ($\bar{V}_s = V_s \angle \theta_s \rightarrow \bar{V}_s = V_s \angle 0$). Once the problem is solved, all angles are shifted back by θ_s to obtain the actual values, where the slack bus angle being is the reference.

The optimization problem in the previous section is solved firstly to identify the voltage thresholds. The system can be modeled accurately using the identified thresholds. For instance, for the given system in the previous section, Fig. 2.18 summarises the steady-state equations and limits used to find the state variables of the Type-III WT for a given stator voltage. To validate the analysis conducted in the this section, a testbed of Type-III WT model is simulated in MATLAB/SimPowerSystems (2020), as shown in Fig .2.19. The system parameters are given system in Table 3.2, A transmission line with SCR=10 is assumed to be connected between the grid and the Type-III WT. The calculations are conducted considering four different values of the grid voltage ($V_g = 0.74, 0.70, 0.67, 0.65$ p.u), which lead to different operating conditions. The steady-state calculations are conducted using YALMIP through nonlinear programming solver Ipopt. Table 2.5 shows the calculation results and their mismatch with simulation results for the four cases.

2.4 Conclusion

This chapter proposed an optimization-based algorithm for calculating the steady-state operating condition of DFIG-based WT. The proposed method is based on a full-order model of DFIG-based WTs and considers the control limits and the losses in the converters. The proposed method is validated using electromagnetic-transient simulation built using the full-order dynamic model of DFIG-based WTs.

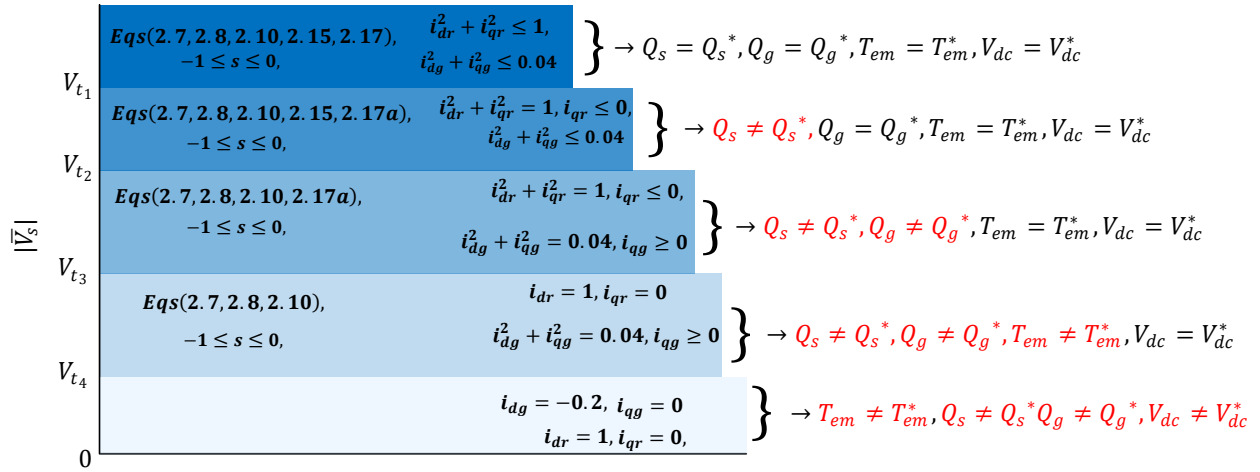


Figure 2.18: Steady-state model of the given system.

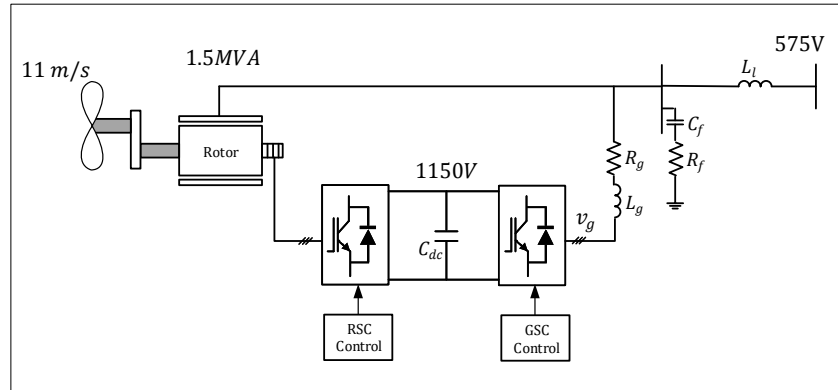


Figure 2.19: EMT model configuration.

Table 2.4: Parameters of the Simulink model

R_s	0.023(p.u)	friction factor	0	X_g	0.3(p.u)
R_r	0.016(p.u)	pole pairs	3	R_g	0.003(p.u)
X_s	0.18(p.u)	Inertia	0.0685 s	C_{dc}	0.01 (F)
X_r	0.16(p.u)	S_n	1.5 (MVA)	V_{dc}	1150 V
X_m	2.9(p.u)	V_n	575 V	Q_s^*	-0.2(p.u)
I_r^{limit}	1(p.u)	I_g^{limit}	0.2(p.u)	Q_g^*	-0.1(p.u)
W_{wind}	11 m/s (1 p.u)	T_{em}^*	-0.63(p.u)	f_n	60 Hz
X_l	0.10(p.u)	Q_f	0.08(p.u)	P_f	0.0016(p.u)

Table 2.5: Steady-state results

	Case-A		Case-B		Case-C		Case-D	
	Analysis	Mismatch	Analysis	Mismatch	Analysis	Mismatch	Analysis	Mismatch
i_{ds}	-0.8142	-1.9E-7	-0.8561	1.3E-8	-0.8901	-6.7E-7	-0.8889	-3.8E-6
i_{qs}	0.1566	1.1E-6	0.0690	7.9E-6	-0.0529	8.6E-6	-0.3716	9.9E-6
i_{dr}	0.8969	-1.6E-7	0.9440	-2.9E-6	0.9826	-1.7E-6	0.9848	1.6E-6
i_{qr}	-0.4393	-1.0E-6	-0.3298	-8.5E-6	-0.1855	-9.4E-6	0.1736	-1.0E-5
i_{dg}	-0.1482	2.2E-7	-0.1596	1.3E-6	-0.1691	1.2E-6	-0.1978	-2.8E-7
i_{qg}	0.1107	2.4E-7	0.1155	1.9E-6	0.1066	2.0E-6	0.0292	-1.0E-5
v_{dr}	-0.1551	8.4E-8	-0.1389	-4.8E-7	-0.1216	-6.4E-7	-0.1050	-2.5E-6
v_{qr}	-0.0800	2.2E-7	-0.0825	1.6E-6	-0.0839	1.3E-6	-0.0935	-9.4E-8
P	0.7180	1.1E-8	0.7168	-1.2E-8	0.7155	-8.1E-9	0.7121	1.4E-6
P_m	0.7499	2.2E-8	0.7499	1.5E-8	0.7499	-8.7E-9	0.7495	7.5E-7
s	-0.1903	-8.9E-8	-0.1903	-2.0E-8	-0.1903	2.1E-9	-0.2211	-3.2E-6

Chapter 3: Steady-State Analysis of Type-III Wind Turbines Subject to Unbalance

3.1 Introduction

This chapter² aims to adequately model Type-III WT's under grid unbalance by considering not only positive- and negative-sequence circuits but also the 3rd harmonic circuit. In addition to the modeling, an efficient algorithm for a steady-state harmonic analysis of Type-III WT subject to unbalance is proposed. The latter is achieved by converting the circuit analysis problem to a set of equality constraints and solving the problem using efficient solvers. EMT simulation results validate the analysis results.

The chapter starts with analyzing a simple squirrel cage induction machine (Testbed-A) in section 3.2. Then, the analysis is extended to Type-III WT's (Testbed-B) in section 3.3. Section 3.4 concludes the chapter. In section 3.3, First, the occurrence of the 3rd harmonic in Type-III WT's under unbalance is analyzed mathematically to give a clear insight. Equivalent circuits of the 3rd harmonic of DFIG are presented in Section 3.3.1. A phasor-domain model of Type-III WT's is developed to calculate the positive-, negative-sequence, and 3rd harmonic phasors using the concept of control-based equivalent circuits. The analysis is carried out in three stages. In the first stage, the voltage source converters of the rotor-side and grid-side are assumed to operate with a constant modulation index (Section 3.3.2). In the second stage, current control loops are considered (Section 3.3.3). In the third stage, outer loops are

²Part of this chapter was submitted to Electric Power Systems Research [56],2021. The other part is published in our paper [53],2019. Permissions are included in Appendix A.

considered (Section 3.3.4). The proposed method is validated with electromagnetic transient (EMT) simulations.

3.2 Squirrel Cage Induction Machine (Testbed-A)

In this section, a steady-state analysis is conducted on a squirrel cage induction machine connected to the grid through a transmission line (shown in Fig .2.1). The system is assumed to operate under an unbalanced grid voltage condition.

3.2.1 Equivalent Circuits of an Induction Machine

During unbalanced voltage conditions, a three-phase induction motor can be represented by two equivalent steady-state circuits: positive- and negative-sequence circuits. The zero-sequence is neglected as the zero-sequence stator current does not setup a magnetic field. Hence there is no induction on the rotor side, nor will there be torque generated. If the circuit connecting the motor to the grid is taken into account (as in Fig .2.1), the positive- and negative-sequence equivalent circuits will be given in Fig. 3.1. The core loss is neglected since it is very low compared to the rotor and the stator copper losses.

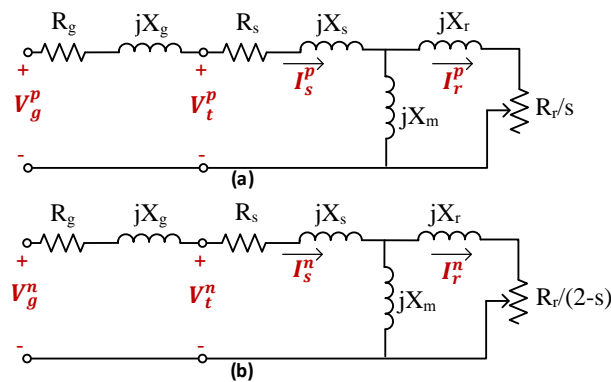


Figure 3.1: Induction motor equivalent circuit. (a) Positive-sequence circuit. (b) Negative-sequence circuit.

In order to find the nine steady-state variables including stator positive- and negative-sequence currents (notated as $I_s^p \angle \phi_s^p$, $I_s^n \angle \phi_s^n$), rotor positive- and negative-sequence currents, (notated as $I_r^p \angle \phi_r^p$, $I_r^n \angle \phi_r^n$) and machine slip (notated as s) for the system in Fig .2.1 for a given grid voltage and motor torque, nine equations should be considered. Difficulties are introduced due to the non-linearity of these equations. In following section, detailed formulation is provided to solve the problem through an advanced computing tool (YALMIP [54]).

The two equivalent circuits can be expressed by four equations, shown in (3.1).

$$\begin{aligned} -V_g^p \angle \theta_g^p + (R_s + R_g + j(X_s + X_m + X_g))I_s^p \angle \phi_s^p \\ - jX_m I_r^p \angle \phi_r^p = 0 \end{aligned} \quad (3.1a)$$

$$\begin{aligned} -V_g^n \angle \theta_g^n + (R_s + R_g + j(X_s + X_m + X_g))I_s^n \angle \phi_s^n \\ - jX_m I_r^n \angle \phi_r^n = 0 \end{aligned} \quad (3.1b)$$

$$\left(\frac{R_r}{s} + j(X_r + X_m) \right) I_r^p \angle \phi_r^p - jX_m I_s^p \angle \phi_s^p = 0 \quad (3.1c)$$

$$\left(\frac{R_r}{2-s} + j(X_r + X_m) \right) I_r^n \angle \phi_r^n - jX_m I_s^n \angle \phi_s^n = 0 \quad (3.1d)$$

Further, the voltage of the motor terminals can be found:

$$V_t^p \angle \theta_t^p = -V_g^p \angle \theta_g^p + (R_m + j(X_s))I_s^p \angle \phi_s^p \quad (3.2)$$

$$V_t^n \angle \theta_t^n = -V_g^n \angle \theta_g^n + (R_g + j(X_s))I_s^n \angle \phi_s^n$$

The air gap power developed by the positive and negative-sequence components is given in (3.3). One produces forward electromagnetic torque while the other produces backward torque.

$$P_{ag}^p = 3(I_r^p)^2 \frac{R_r}{s}, P_{ag}^n = 3(I_r^n)^2 \frac{R_r}{(2-s)} \quad (3.3)$$

As a result of the two components of the air gap power, the electromagnetic torque of the motor will contain two components as given in (3.4).

$$\begin{aligned}
 T_{em}^p &= \frac{\text{poles}}{2} \frac{P_{ag}^p}{\omega_e}, \quad T_{em}^n = \frac{\text{poles}}{2} \frac{P_{ag}^n}{-\omega_e}, \\
 T_{em} &= T_{em}^p + T_{em}^n = \frac{\text{poles}}{2} \frac{3R_r}{\omega_e} \left[\frac{(I_r^p)^2}{s} - \frac{(I_r^n)^2}{(2-s)} \right]
 \end{aligned} \tag{3.4}$$

3.2.2 Ripples in the Torque

During the unbalanced condition of the stator, the magnitude of the three-phases and the angle displacements will not be the same. The positive- and negative-component of the stator current can be obtained by decomposing the three-phase currents using the symmetrical component theory. The positive-sequence component of rotor current can be observed at frequency $\omega_r = \omega_e - \omega_m = s\omega_e$ while the negative sequence component are observed at frequency $-\omega_e - \omega_m = -(2-s)\omega_e$.

While interactions between stator and rotor currents in the same sequence produce torque of dc values, interactions between stator current and rotor current in difference sequences introduce ripples of 120 Hz. Detailed analysis can be referred in [57].

3.2.3 Steady-State Calculations

Expressions (3.1a-3.1d), related to the motor circuits, constitute four complex algebraic equations which can be separated into eight real algebraic equations as given in (3.5a-3.5h). Expression (3.5i) is related to the torque requirement. If the grid voltage and motor torque are given, there are nine unknown state variables, magnitudes and angles of rotor and stator positive- and negative-sequence currents, and the slip rate. The nine unknown quantities of the motor can be found by solving the nine equations (3.5a-3.5i) using any well-known iterative way such as Newton-Raphson. This paper uses YALMIP to solve the nonlinear set of equations through a nonlinear programming solver `fmincon`. Once the stator currents

are found, the terminal voltages of the motor can be found using (3.2). For the balanced voltage condition, only the set of equations related to the positive sequence circuit are used and, the developed torque of the motor has only the positive component.

$$f_1 = -V_g^p \cos \theta_g^p + (R_s + R_g)I_s^p \cos \phi_g^p + X_m I_r^p \sin \phi_r^p - (X_s + X_m + X_g)I_s^p \sin \phi_s^p = 0 \quad (3.5a)$$

$$f_2 = -V_g^p \sin \theta_g^p + (R_s + R_g)I_s^p \sin \phi_g^p - X_m I_r^p \cos \phi_r^p + (X_s + X_m + X_g)I_s^p \cos \phi_s^p = 0 \quad (3.5b)$$

$$f_3 = \frac{R_r}{s} I_r^p \cos \phi_r^p - (X_r + X_m)I_r^p \sin \phi_r^p + X_m I_s^p \sin \phi_s^p = 0 \quad (3.5c)$$

$$f_4 = \frac{R_r}{s} I_r^p \sin \phi_r^p + (X_r + X_m)I_r^p \cos \phi_r^p - X_m I_s^p \cos \phi_s^p = 0 \quad (3.5d)$$

$$f_5 = -V_g^n \cos \theta_g^n + (R_s + R_g)I_s^n \cos \phi_g^n + X_m I_r^n \sin \phi_r^n - (X_s + X_m + X_g)I_s^n \sin \phi_s^n = 0 \quad (3.5e)$$

$$f_6 = -V_g^n \sin \theta_g^n + (R_s + R_g)I_s^n \sin \phi_g^n - X_m I_r^n \cos \phi_r^n + (X_s + X_m + X_g)I_s^n \cos \phi_s^n = 0 \quad (3.5f)$$

$$f_7 = \frac{R_r}{2-s} I_r^n \cos \phi_r^n - (X_r + X_m)I_r^n \sin \phi_r^n + X_m I_s^n \sin \phi_s^n = 0 \quad (3.5g)$$

$$f_8 = \frac{R_r}{2-s} I_r^n \sin \phi_r^n + (X_r + X_m)I_r^n \cos \phi_r^n - X_m I_s^n \cos \phi_s^n = 0 \quad (3.5h)$$

$$f_9 = T_{em} \frac{2\omega_e}{p} - 3I_r^{p2} \left[\frac{R_r}{s} \right] + 3I_r^{n2} \left[\frac{R_r}{(2-s)} \right] = 0 \quad (3.5i)$$

3.2.3.1 Initial Values

Solving the set of the nonlinear equations (3.5a-3.5i) requires setting initial values for the decision variables. A large error in the initial values may cause the algorithm to converge to a local solution not desired. It may also cause non-convergence issues. A robust method to estimate the initial values is by obtaining the values of the variable at a slip rate close to zero since it is the region where induction motors operate during the steady-state operation. In this literature, the initial values are obtained at slip equals to 0.1 as given in (3.6).

$$\begin{aligned}
I_s^p \angle \phi_s^p &= \frac{V_g^p \angle \theta_r^p}{R_s + R_g + Z_p + jX_s + jX_g} \\
I_s^n \angle \phi_s^n &= \frac{V_g^n \angle \theta_r^n}{R_s + R_g + Z_n + jX_s + jX_g} \\
I_r^p \angle \phi_r^p &= \frac{jX_m I_s^p \angle \phi_s^p}{jX_m + jX_r + \frac{R_r}{0.1}} \\
I_r^n \angle \phi_r^n &= \frac{jX_m I_s^n \angle \phi_s^n}{jX_m + jX_r + \frac{R_r}{2-0.1}} \\
\text{where } Z_p &= \frac{(jX_r + \frac{R_r}{0.1})jX_m}{jX_r + \frac{R_r}{0.1} + jX_m} \\
Z_n &= \frac{(jX_r + \frac{R_r}{2-0.1})jX_m}{jX_r + \frac{R_r}{2-0.1} + jX_m}
\end{aligned} \tag{3.6}$$

3.2.4 Case Studies

3.2.4.1 Motor State Variables During Unbalanced Voltage

In order to validate the proposed method in the previous section, a testbed of an induction motor served by a voltage source is simulated in MATLAB/SimPowerSystems environment, as shown in Fig .2.3. The motor is connected to the grid bus through an RL circuit. The model parameters are shown in Table 2.1.

In the simulation model, the motor runs until it reaches the steady-state region. Then, an unbalanced voltage condition occurs where the voltage at phase a drops to 0.8 p.u. The stator voltages and currents during the voltage dip condition obtained from the simulated are shown in Fig. 3.2a and Fig. 3.2b, respectively. Fig. 3.2c shows the motor speed. In Table 3.1, the simulation results are compared with the results using the proposed method. The input values to the optimization problem are the grid voltage (phase-a is 143.7 V or 0.8 p.u) and the load Torque (11.9 N.m). The algorithm required 4 iterations to find the solutions for the equations. Fig. 3.3 shows the rotor currents for phase A and the positive- and negative-component of the rotor current after they are extracted. The positive-sequence of the rotor

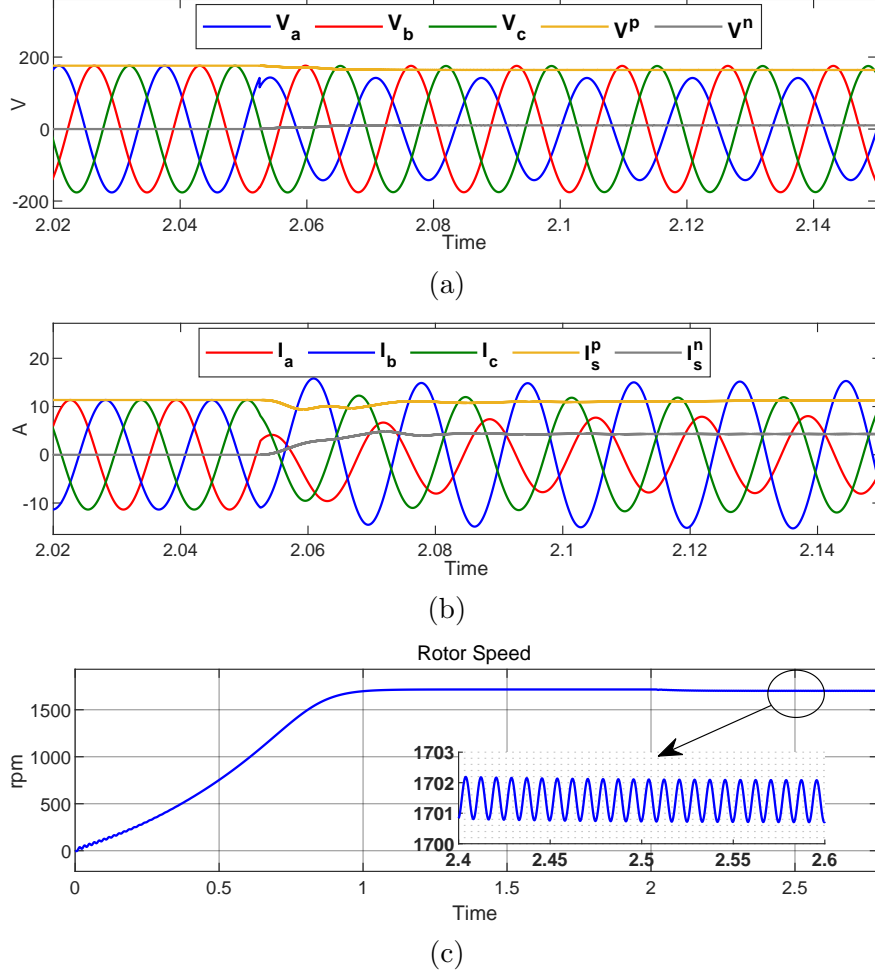


Figure 3.2: Simulation results. (a) Stator voltages. (b) Stator currents. (c) Motor speed.

Table 3.1: Motor variables

	Simulation	Proposed method
$I_s^p \angle \phi_s^p$	11.8148 \angle -37.2163	11.8145 \angle -37.2151
$I_s^n \angle \phi_s^n$	4.3057 \angle 109.5634	4.3010 \angle 109.5387
$V_t^p \angle \theta_t^p$	164.0435 \angle -0.9893	164.0438 \angle -0.9893
$V_t^n \angle \theta_t^n$	10.3024 \angle 179.2334	10.3043 \angle 179.2385
s	0.0548	0.0548
$I_r^p \angle \phi_r^p$	10.05 \angle -8.2253	10.0445 \angle -8.2268
$I_r^n \angle \phi_r^n$	4.1805 \angle 110.4117	4.1799 \angle 110.4327

current rotates at frequency 3.2 Hz while the negative component has a frequency of 116.7

Hz. Table 3.1 shows the magnitude and angles of the positive and negative component of the rotor current obtained from the simulation and proposed method.

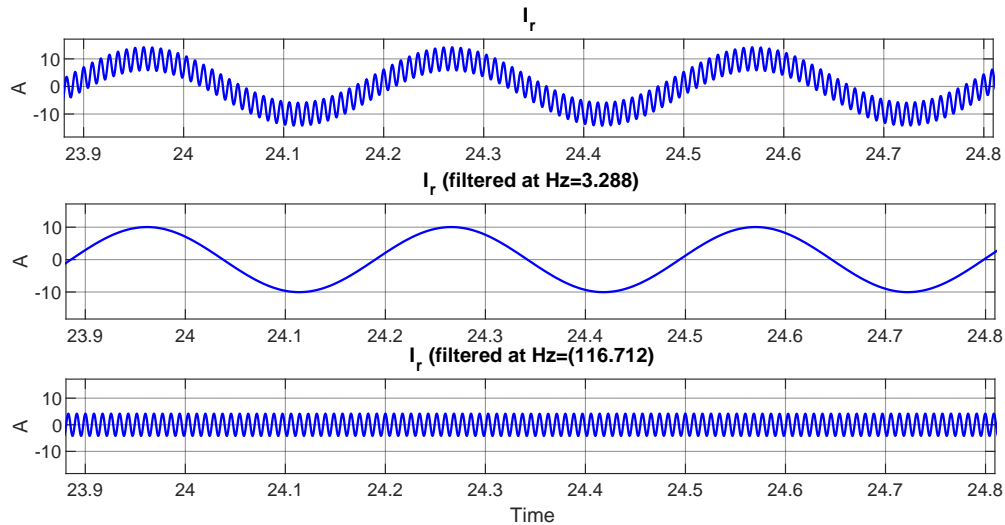


Figure 3.3: Rotor currents of the induction motor.

3.2.4.2 Maximum Torque During Unbalanced Voltage Dip

The maximum or breakdown torque is a function of the terminal voltage of the motor, as shown in Fig. 3.4. As the terminal voltage drops, the maximum torque can be achieved by the motor decreases. During unbalanced voltage conditions, the maximum load torque limit the induction motor can handle is reduced due to the reversing torque produced by the negative sequence current. When a motor reaches a steady-state region during a voltage dip, the motor torque can be increased to a certain value or limit. Beyond this limit, the motor will go to the instability region where the steady-state equations (3.5a-3.5i) can not be satisfied. For example, in Fig. 3.8, after the grid voltage dropped at $t = 1.5$ s, the motor reaches the steady-state region again and meets the load torque requirement. At $t = 2.5$ s, the load torque is increased. The motor can serve the given load torque since it is below the maximum breakdown point. At $t = 4$ s, the load torque is increased again. However, the load torque is more than the maximum torque capability of the motor during the voltage

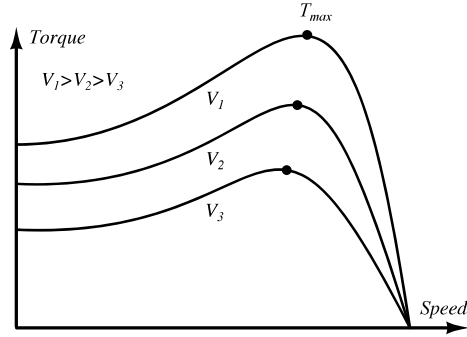


Figure 3.4: Torque-speed curve of induction motor.

dip which leads the motor to the instability region. Fig. 3.5a shows the balanced voltage dip case while Fig. 3.5b shows the unbalanced voltage case.

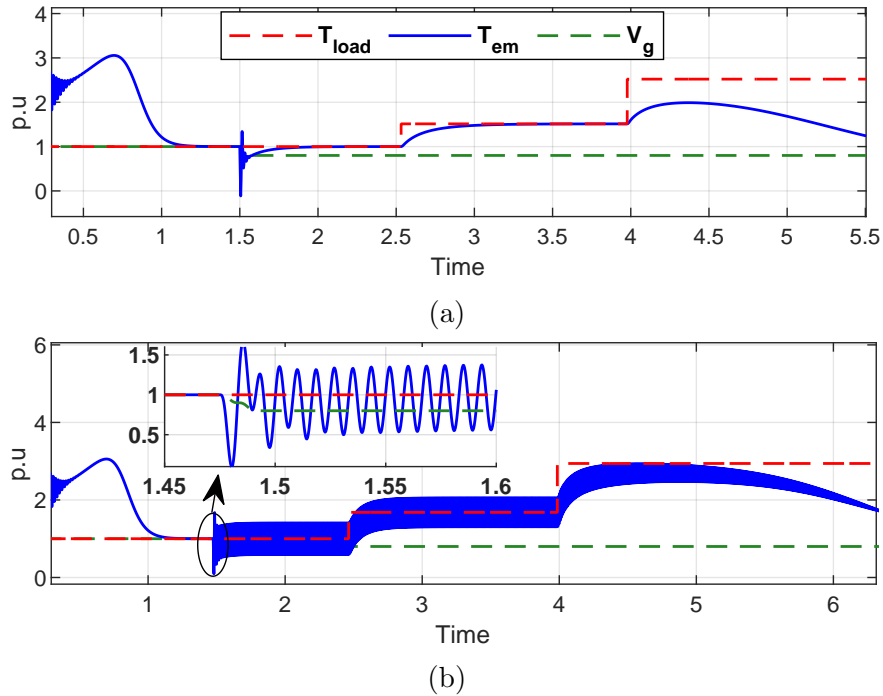


Figure 3.5: Induction motor response to change in load torque. (a) Balanced voltage dip. (b) Unbalanced voltage dip.

To find the maximum torque limit during balanced and unbalanced voltage dip conditions, the optimization problem is formulated as in (3.7) and solved by `fmincon` through YALMIP. The objective function will be the maximization of the electromagnetic torque.

The constraints of the optimization problem include the nine equations describing the circuits and torque, the slip limit, and the angle limits. The decision variables are the stator, rotor currents and the slip $(I_s^p, I_s^n, I_r^p, I_r^n, \phi_s^p, \phi_s^n, \phi_r^p, \phi_r^n, s)$ while the input value to the optimization problem is the grid voltage.

$$\begin{aligned}
& \text{Maximize}(T_{em}) \\
& \text{subject to (2.5)} \\
& 1 \geq s \geq 0 \\
& \pi \geq \phi_s^p, \phi_s^n, \phi_r^p, \phi_r^n \geq -\pi
\end{aligned} \tag{3.7}$$

The maximum torques are found to be 23.5 and 32 N.m for the balanced and unbalanced voltage dip, respectively. To validate these limits, the load torque is set to values that are below the thresholds by 0.5 N.m at $t = 2.5$ s after the occurrence of the voltage dip at $t = 1.5$ s, as shown in Fig. 3.6. At $t = 6$ s, the load torque is increased above the thresholds by 0.5 N.m. It can be seen that the motor loses its stability after crossing the given thresholds while it is stable below them.

3.3 Type-III Wind Turbine (Testbed-B)

In this section, the steady-state analysis of the induction machine subject to unbalance stator voltage is extended to Type-III WTs.

3.3.1 Induction Machine Circuit Analysis (DFIG)

During unbalanced stator voltage conditions, a three-phase squirrel-cage induction motor can be represented by two separate equivalent steady-state circuits: positive- and negative-sequence circuits. Since the zero-sequence stator current does not generate a magnetic field, the zero-sequence is neglected. For DFIG, since the RSC is connected to the rotor, 3rd harmonic component will occur in the currents. This phenomenon is due to dq -frame RSC

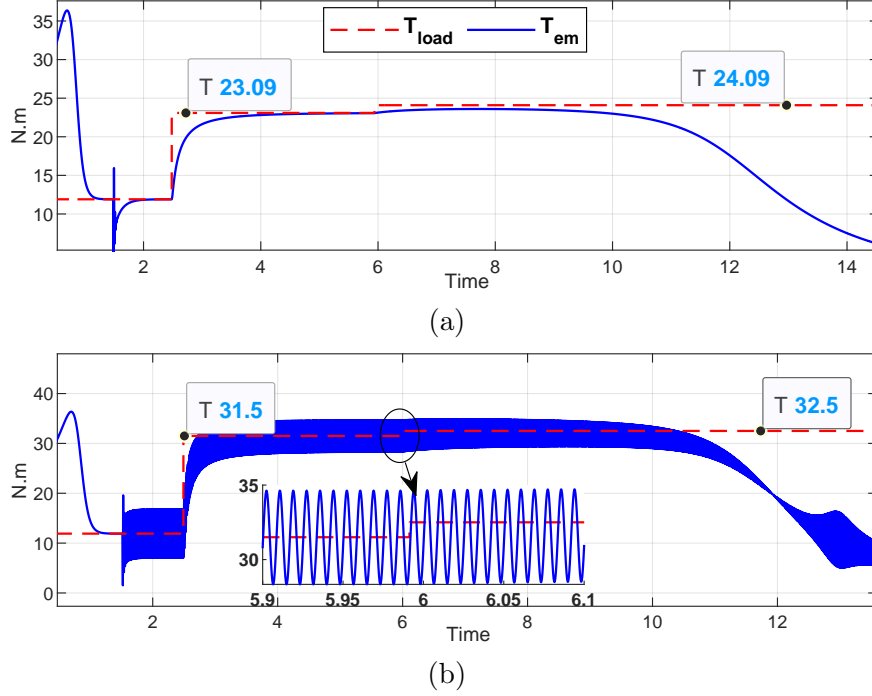


Figure 3.6: Motor response for change in load torque. (a) During balanced dip. (b) During unbalanced dip.

converter control and the well-known frequency coupling phenomenon of converter controls [52, 58]. It is also demonstrated by (3.14) in Section 3.3.2.1 when the VSC is assuming dq -frame modulation and the DC-link voltage has 2nd harmonics.

To find out the equivalent circuit of each sequence and 3rd harmonic, the slip needs to be calculated. For the positive-sequence circuit with the assumption that the three-phase stator currents are positive sequence at the nominal frequency ω_0 , the slip can be written as follows.

$$s = \frac{\omega_0 - \omega_m}{\omega_0} \quad (3.8)$$

where ω_m is the angular frequency corresponding to the mechanical speed.

Since the negative-sequence stator current generates a magnetic field rotating in the opposite direction with respect to the positive-sequence field, the negative-sequence slip can be expressed as the following.

$$s^- = \frac{-\omega_0 - \omega_m}{-\omega_0} = \frac{-\omega_0 - (1-s)\omega_0}{-\omega_0} = 2 - s \quad (3.9)$$

If the stator current has 3rd harmonic (positive-sequence), then the resulting magnetic field rotates at three-times of the nominal speed. The 3rd harmonic slip can be written as follows.

$$s^{(3)} = \frac{3\omega_0 - \omega_m}{3\omega_0} = \frac{2 + s}{3} \quad (3.10)$$

As an example, when the machine is rotating at a speed of 48 Hz ($s = 0.2$), the positive sequence rotor currents will be rotating at +12 Hz ($f_0 - f_m = 60 - 48$). The negative-sequence rotor currents can be seen as a three-phase balanced set with a frequency of -108 Hz ($= -60 - 48$) Hz, while the 3rd harmonic will be rotating at +132 Hz ($= 180 - 48$).

When the machine is rotating at 72 Hz ($s = -0.2$), the positive sequence rotor currents will be rotating at -12 Hz ($= 60 - 72$), and the negative-sequence currents will be rotating at -132 Hz ($= -60 - 72$). The 3rd harmonic will be rotating at +108 Hz ($= 180 - 72$).

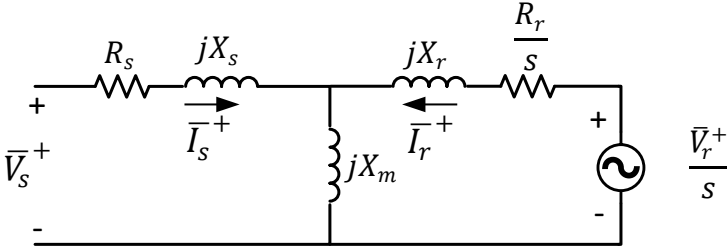
The rotor circuit electric frequency can be found as follows for the positive-sequence, negative-sequence and, 3rd harmonic circuits.

$$\begin{aligned} \text{Positive: } f_r &= s f_0 \\ \text{Negative: } f_r^- &= s^- (-f_0) = (2 - s)(-f_0) \\ \text{3rd Harmonic: } f_r^{(3)} &= s^{(3)}(3f_0) = \frac{2 + s}{3}(3f_0) \end{aligned} \quad (3.11)$$

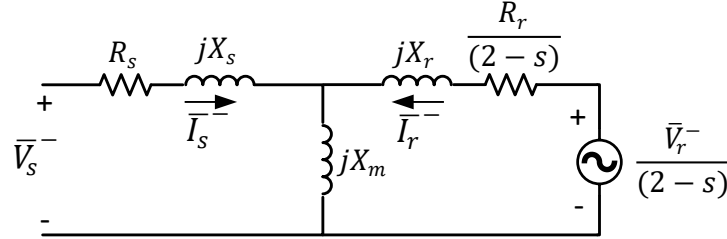
where f_0 is the nominal frequency in Hz.

In the positive-sequence induction machine equivalent circuit, shown in Fig. 3.7, both the electro-magnetomotive force (emf) in the rotor circuit and the rotor side impedance at $f_r = s f_0$ Hz are divided by s to have the rotor side and the stator side integrated into one circuit. Using the same analogy, the equivalent circuits of negative-sequence and 3rd

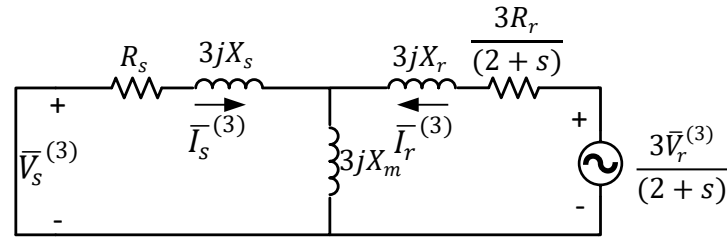
harmonic component are derived and shown in Fig. 3.7. The core loss is neglected since it is very low compared to the rotor and the stator copper losses. The equivalent circuits can be expressed by the equations shown in (3.12a-3.12f).



(a)



(b)



(c)

Figure 3.7: DFIG equivalent circuit. (a) Positive-sequence equivalent circuit. (b) Negative-sequence equivalent circuit. (c) 3rd harmonic equivalent circuit.

$$-\bar{V}_s^+ + (R_s + jX_s + jX_m)\bar{I}_s^+ + jX_m\bar{I}_r^+ = 0 \quad (3.12a)$$

$$-\frac{\bar{V}_r^+}{s} + \left(\frac{R_r}{s} + j(X_r + X_m)\right)\bar{I}_r^+ + jX_m\bar{I}_s^+ = 0 \quad (3.12b)$$

$$-\bar{V}_s^- + (R_s + jX_s + jX_m)\bar{I}_s^- + jX_m\bar{I}_r^- = 0 \quad (3.12c)$$

$$-\frac{\bar{V}_r^-}{2-s} + \left(\frac{R_r}{2-s} + j(X_r + X_m)\right)\bar{I}_r^- + jX_m\bar{I}_s^- = 0 \quad (3.12d)$$

$$(R_s + 3jX_s + 3jX_m)\bar{I}_s^{(3)} + 3jX_m\bar{I}_r^{(3)} = 0 \quad (3.12e)$$

$$-\frac{3\bar{V}_r^{(3)}}{2+s} + \left(\frac{3R_r}{2+s} + j3(X_r + X_m)\right)\bar{I}_r^{(3)} + j3X_m\bar{I}_s^{(3)} = 0 \quad (3.12f)$$

where superscript $-$ notates negative-sequence components and superscript (3) notates 3rd harmonic components. Subscripts s and r notate stator side and rotor side variables and parameters. R_s, R_r, X_s, X_r, X_m are stator, rotor resistance, stator, rotor leakage reactance, and magnetizing reactance at the fundamental frequency, respectively.

3.3.2 Constant Modulation Index

In this subsection, a constant dq -frame modulation index is assumed for both RSC and GSC. Hence, no control is implemented on the two VSCs. A phasor-domain circuit modeling approach will be presented to compute the negative-sequence and 3rd harmonic components in the voltage and current waveform during unbalance grid conditions. 13 variables will be found by solving a set of linear equations. The set of the unknown variables related to negative-sequence, 3rd harmonic components, and DC-link are listed as follows:

- RSC ac side components: $\bar{V}_r^-, \bar{I}_r^-, \bar{V}_r^{(3)}, \bar{I}_r^{(3)}$
- GSC ac side ncomponents: $\bar{V}_g^-, \bar{I}_g^-, \bar{V}_g^{(3)}, \bar{I}_g^{(3)}$
- Stator side ac components: $\bar{I}_s^-, \bar{I}_s^{(3)}$
- DC-link components: $\bar{V}_{dc}^{(2)}, \bar{I}_{dc1}^{(2)}, \bar{I}_{dc2}^{(2)}$.

Fig. 3.8 represents the Type-III WT. The stator terminal of the induction machine is connected directly to the grid bus. The machine's rotor is connected to the grid through a back-to-back converter(AC/DC-DC/AC): RSC and GSC. The two PWM converters are coupled through the DC-link. Modulation indices m_r and m_g are three-phase positive sequence sine waves with a frequency of sf_0 and f_0 , respectively.

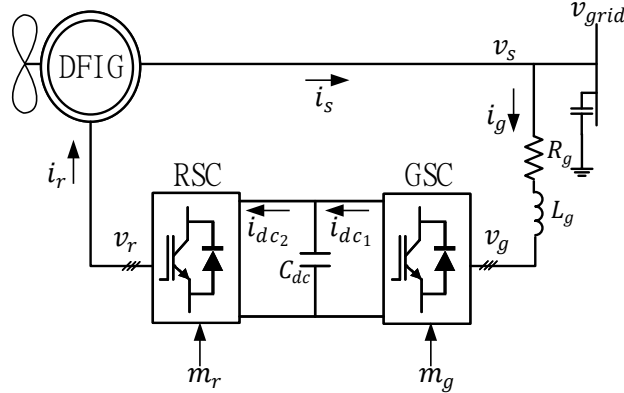
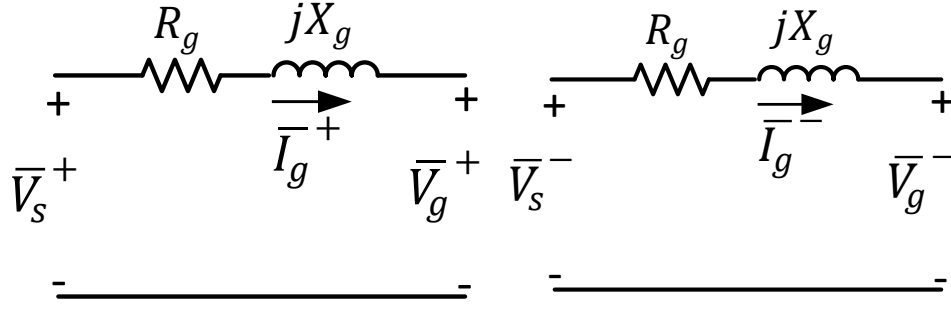


Figure 3.8: Type III WTs (constant modulation index).

Assuming that the grid bus is experiencing an unbalanced voltage condition, so the grid voltage v_{grid} will contain positive- and negative-sequence components.

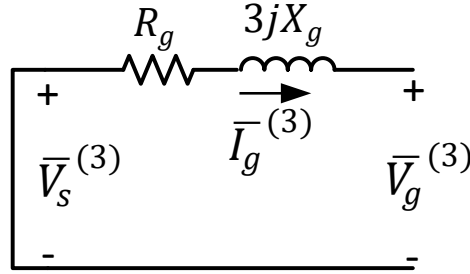
3.3.2.1 GSC Ac Side and DC/AC Relationship

The equivalent circuit of the positive-sequence, negative-sequence and 3rd harmonic component of the connection between the GSC and the grid bus can be viewed during the unbalanced voltage condition as shown Fig. 3.9. The equivalent circuits can be expressed by the equations shown in (3.13a-3.13c).



(a)

(b)



(c)

Figure 3.9: GSC ac side. (a) Positive-sequence equivalent circuit. (b) Negative-sequence equivalent circuit. (c) 3rd harmonic equivalent circuit.

$$-\bar{V}_s^+ + (R_g + jX_g)\bar{I}_g^+ + \bar{V}_g^+ = 0 \quad (3.13a)$$

$$-\bar{V}_s^- + (R_g + jX_g)\bar{I}_g^- + \bar{V}_g^- = 0 \quad (3.13b)$$

$$(R_g + 3jX_g)\bar{I}_g^{(3)} + \bar{V}_g^{(3)} = 0 \quad (3.13c)$$

For GSC, the relationship between the DC and AC voltages is the following:

$$\vec{v}_g = \vec{m}_g \frac{v_{dc}}{2} = \bar{m}_g e^{j(\omega_0 t - \frac{\pi}{2})} \frac{v_{dc}}{2}, \quad (3.14)$$

where \bar{m}_g is the dq -frame vector, $\vec{\cdot}$ notates space vector that aggregates three-phase variables:

$$\vec{f} = f_a + e^{j\frac{2\pi}{3}} f_b + e^{-j\frac{2\pi}{3}} f_c.$$

During unbalance voltage conditions, ripple of $2f_0$ will appear in the DC-link. The DC voltage can be written in the time domain as the following [23, 59, 60].

$$v_{dc}(t) = V_{dc}^{(0)} + V_{dc}^{(2)} \sin(2\omega_0 t + \theta_{dc}) \quad (3.15)$$

where $V_{dc}^{(0)}$ is the DC component of the DC-link voltage. $V_{dc}^{(2)}$ and θ_{dc} are the amplitude and phase angle of the $2f_0$ oscillations of the DC-link voltage. The relationship in (3.14) can be re-written as follows.

$$\begin{aligned} \vec{v}_g &= \frac{\bar{m}_g}{2} e^{j(\omega_0 t - \frac{\pi}{2})} \left(V_{dc}^{(0)} + \frac{\bar{V}_{dc}^{(2)} e^{j(2\omega_0 t - \frac{\pi}{2})} - \bar{V}_{dc}^{(2)*} e^{-j(2\omega_0 t - \frac{\pi}{2})}}{2j} \right) \\ &= \underbrace{\frac{\bar{m}_g}{2} V_{dc}^{(0)} e^{j(\omega_0 t - \frac{\pi}{2})}}_{f_0 \text{Hz}} + \underbrace{-j \frac{\bar{m}_g \bar{V}_{dc}^{(2)}}{4} e^{j(3\omega_0 t - \frac{\pi}{2})}}_{3f_0 \text{Hz}} \\ &\quad - \underbrace{j \frac{\bar{m}_g \bar{V}_{dc}^{(2)*}}{4} e^{-j(\omega_0 t - \frac{\pi}{2})}}_{-f_0 \text{Hz}} \end{aligned} \quad (3.16)$$

Note that sine is the base function instead of cosine. As it can be seen in (3.16), the terminal voltage of the GSC contains three components: positive-, negative-sequence and 3rd harmonic components. The positive-sequence is only dependent on the DC value of the DC-link voltage while the negative-sequence and the 3rd harmonic component are dependent on the $2f_0$ ripple component in the DC-link voltage.

Thus, in the phasor frame, the GSC voltage has three harmonic components and, they can be written as follows.

$$\bar{V}_g^+ = \frac{1}{2} \bar{m}_g V_{dc}^{(0)} \quad (3.17a)$$

$$\bar{V}_g^- = \frac{j}{4} \bar{m}_g^* \bar{V}_{dc}^{(2)} \quad (3.17b)$$

$$\bar{V}_g^{(3)} = \frac{-j}{4} \bar{m}_g \bar{V}_{dc}^{(2)} \quad (3.17c)$$

Note that the phasor uses sine, instead of cosine as the base function. The currents relations can be found starting from the power conservation equation as stated below.

$$\begin{aligned} P_{dc_1} &= P_g, \\ \implies v_{dc} i_{dc_1} &= \frac{3}{2} \Re(\vec{v}_g \vec{i}_g^*) = \frac{3}{4} \Re(\vec{m}_g v_{dc} \vec{i}_g^*) \\ \implies i_{dc_1} &= \Re\left(\frac{3}{4} \vec{m}_g \vec{i}_g^*\right) = \frac{3}{8} \left(\vec{m}_g \vec{i}_g^* + \vec{m}_g^* \vec{i}_g\right) \end{aligned}$$

Since the GSC ac current contains positive-, negative-sequence and 3rd harmonic components, its space vector can be written as follows.

$$\vec{i}_g = \bar{I}_g^+ e^{j(\omega_0 t - \frac{\pi}{2})} + \bar{I}_g^* e^{-j(\omega_0 t - \frac{\pi}{2})} + \bar{I}_g^{(3)} e^{j(3\omega_0 t - \frac{\pi}{2})}.$$

Thus, the dc current has the following expression.

$$i_{dc_1} = \frac{3}{8} \underbrace{(\bar{m}_g \bar{I}_g^+ + \bar{m}_g^* \bar{I}_g^+)}_{0\text{Hz}} + \underbrace{\bar{m}_g^* \bar{I}_g^{(3)} e^{j2\omega_0 t} + \bar{m}_g \bar{I}_g^{(3)*} e^{-j2\omega_0 t}}_{2f_0\text{Hz}} + \underbrace{\bar{m}_g \bar{I}_g^- e^{j(2\omega_0 t + \pi)} + \bar{m}_g^* \bar{I}_g^{*-} e^{-j(2\omega_0 t + \pi)}}_{2f_0\text{Hz}} \quad (3.18)$$

In the phasor frame, the DC current component can be written as the following.

$$I_{dc1}^{(0)} = \frac{3}{4} m_g I_g^+ \cos(\theta_{m_g} - \theta_g^+) \quad (3.19a)$$

$$\bar{I}_{dc1}^{(2)} = \frac{3}{4} (-j \bar{m}_g \bar{I}_g^- + j \bar{m}_g^* \bar{I}_g^{(3)}) \quad (3.19b)$$

3.3.2.2 RSC

Similarly, the RSC voltages can be derived as the following.

$$\begin{aligned} \vec{v}_r &= \frac{\vec{m}_r}{2} v_{dc} \\ &= \frac{\bar{m}_r}{2} e^{j(s\omega_0 t - \frac{\pi}{2})} \left(V_{dc}^{(0)} + \frac{\bar{V}_{dc}^{(2)} e^{j(2\omega_0 t - \frac{\pi}{2})} - \bar{V}_{dc}^{(2)*} e^{-j(2\omega_0 t - \frac{\pi}{2})}}{2j} \right) \\ &= \underbrace{\frac{\bar{m}_r}{2} V_{dc}^{(0)} e^{j(s\omega_0 t - \frac{\pi}{2})}}_{s f_0 \text{ Hz}} \underbrace{-j \frac{\bar{m}_r}{4} \bar{V}_{dc}^{(2)} e^{j((2+s)\omega_0 t - \frac{\pi}{2})}}_{(2+s) f_0 \text{ Hz}} \underbrace{-j \frac{\bar{m}_r}{4} \bar{V}_{dc}^{(2)*} e^{-j((2-s)\omega_0 t - \frac{\pi}{2})}}_{-(2-s) f_0 \text{ Hz}} \end{aligned} \quad (3.20)$$

It can be seen that the occurrence of the negative-sequence $-(2-s)f_o$ and 3rd harmonic component $((2+s)f_o)$ at the RSC is due to the occurrence of the $2f_o$ ripple in the DC link. The two components are independent of the average value of the DC voltage $V_{dc}^{(0)}$. In the phasor domain, the relationship of voltage components can be written as the following:

$$\bar{V}_r^+ = \frac{1}{2} \bar{m}_r V_{dc}^{(0)}, \quad (3.21a)$$

$$\bar{V}_r^- = \frac{j}{4} \bar{m}_r^* \bar{V}_{dc}^{(2)}, \quad (3.21b)$$

$$\bar{V}_r^{(3)} = \frac{-j}{4} \bar{m}_r \bar{V}_{dc}^{(2)}. \quad (3.21c)$$

Similarly, the currents relations between the AC and DC sides of RSC can be found starting from the power equation stated below.

$$P_{dc_2} = P_r$$

$$i_{dc_2} = \frac{3}{8} \underbrace{(\overline{m}_r \overline{I}_r^{+*} + \overline{m}_r^* \overline{I}_r^+)}_{0 \text{ Hz}} + \underbrace{\overline{m}_r^* \overline{I}_r^{(3)} e^{j2\omega_0 t} + \overline{m}_r \overline{I}_r^{(3)*} e^{-j2\omega_0 t}}_{2f_0 \text{ Hz}} + \underbrace{\overline{m}_r \overline{I}_r^- e^{j(2\omega_0 t + \pi)} + \overline{m}_r^* \overline{I}_r^{-*} e^{-j(2\omega_0 t + \pi)}}_{2f_0 \text{ Hz}} \quad (3.22)$$

In the phasor domain, the current component can be written as the following.

$$I_{dc_2}^{(0)} = \frac{3}{4} m_r I_r^+ \cos(\theta_{m_r} - \theta_r^+) \quad (3.23a)$$

$$\overline{I}_{dc_2}^{(2)} = \frac{3}{4} (-j\overline{m}_r \overline{I}_r^- + j\overline{m}_r^* \overline{I}_r^{(3)}) \quad (3.23b)$$

3.3.2.3 DC-Link

By representing the GSC and RSC as current sources, the DC-link circuit can be viewed as shown in Fig. 3.10.

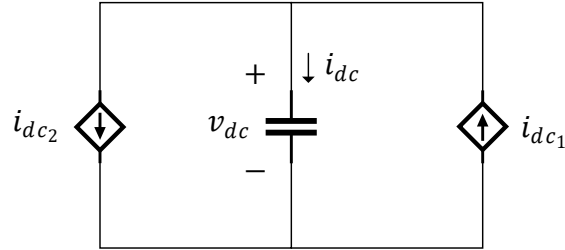


Figure 3.10: DC-link circuit representation.

By applying KCL, the currents relation can be found as follows.

$$i_{dc} = i_{dc_1} - i_{dc_2} \quad (3.24)$$

Considering the dc component and the $2f_0$ component, in phasor-domain, (3.24) can be written as the following.

$$I_{dc}^{(0)} = I_{dc1}^{(0)} - I_{dc2}^{(0)} \quad (3.25a)$$

$$\bar{I}_{dc}^{(2)} = \bar{I}_{dc1}^{(2)} - \bar{I}_{dc2}^{(2)} \quad (3.25b)$$

For the 0 Hz component, the capacitor is open circuited, so (3.25a) can be re-written as the following.

$$\bar{I}_{dc1}^{(0)} = \bar{I}_{dc2}^{(0)} \quad (3.26)$$

For the $2f_0$ Hz component, the relation in (3.25b) can be re-written as the following.

$$j2\omega_0 C_{dc} \bar{V}_{dc}^{(2)} = \bar{I}_{dc1}^{(2)} - \bar{I}_{dc2}^{(2)} \quad (3.27)$$

The set of the 13 unknown variables related to negative-sequence and 3rd harmonic component: $\bar{V}_r^-, \bar{I}_r^-, \bar{V}_g^-, \bar{I}_s^-, \bar{V}_r^{(3)}, \bar{I}_r^{(3)}, \bar{V}_g^{(3)}, \bar{I}_s^{(3)}, \bar{I}_g^-, \bar{I}_g^{(3)}, \bar{V}_{dc}^{(2)}, \bar{I}_{dc1}^{(2)}, \bar{I}_{dc2}^{(2)}$ can be found by solving 13 equations, including induction machine circuits (3.12c)-(3.12f), GSC ac side relationship (3.13b) (3.13c), GSC dc/ac side voltage and current relationship (3.17b) (3.17c) (3.19b), RSC dc/ac side voltage and current relationship (3.21b) (3.21c) (3.23b), and dc-link circuit (3.27). Fig. 3.11 presents the 13 equations and their relationships. This set of equations are linear equations. The solution can be found easily.

3.3.2.4 Validation

To validate the analysis conducted in the previous sections, a testbed of Type-III WT model, as shown in Fig. 3.8, with a constant modulation index is simulated in MATLAB/SimPowerSystems(2020a), as shown in Fig .3.12. The average model is used to omit the harmonics produced by the switching. The model parameters are listed in Table 3.2. The

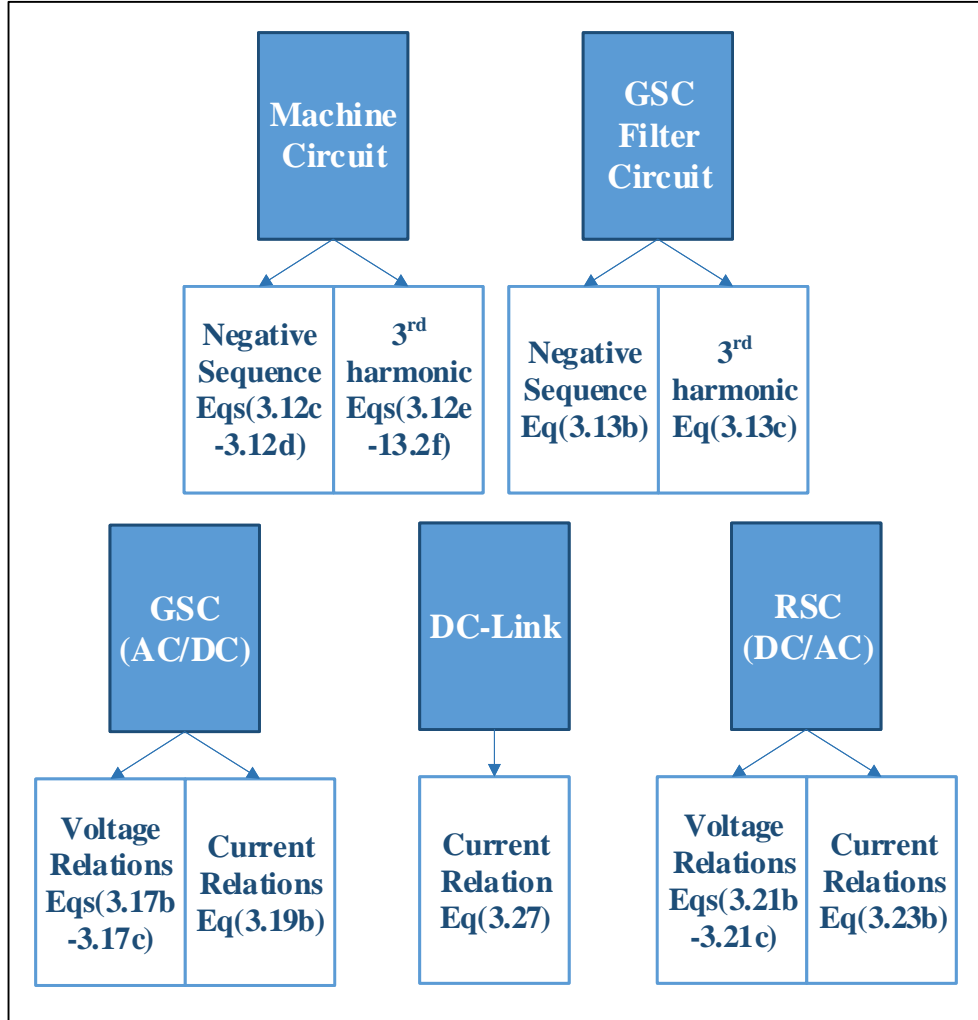


Figure 3.11: Steady-state equations (constant modulation index).

modulation index of the GSC is assumed to be a balanced three-phase positive-sequence with a frequency of 60 Hz ($\bar{m}_g = 0.6\angle 2.9^\circ$), while the modulation index of the RSC is rotating at 12 Hz ($\bar{m}_r = 0.16\angle 13.6^\circ$). The induction machine is rotating at corresponding electrical frequency of 48 Hz. Initially, the system is operating at nominal grid voltage ($V_s^+ = 1\angle 0^\circ$ p.u.). At $t = 10$ seconds, unbalance is introduced into the grid voltage. The positive- and negative-sequence components of the stator voltage are: ($\bar{V}_s^+ = 1\angle 0^\circ, \bar{V}_s^- = 0.15\angle 180^\circ$).

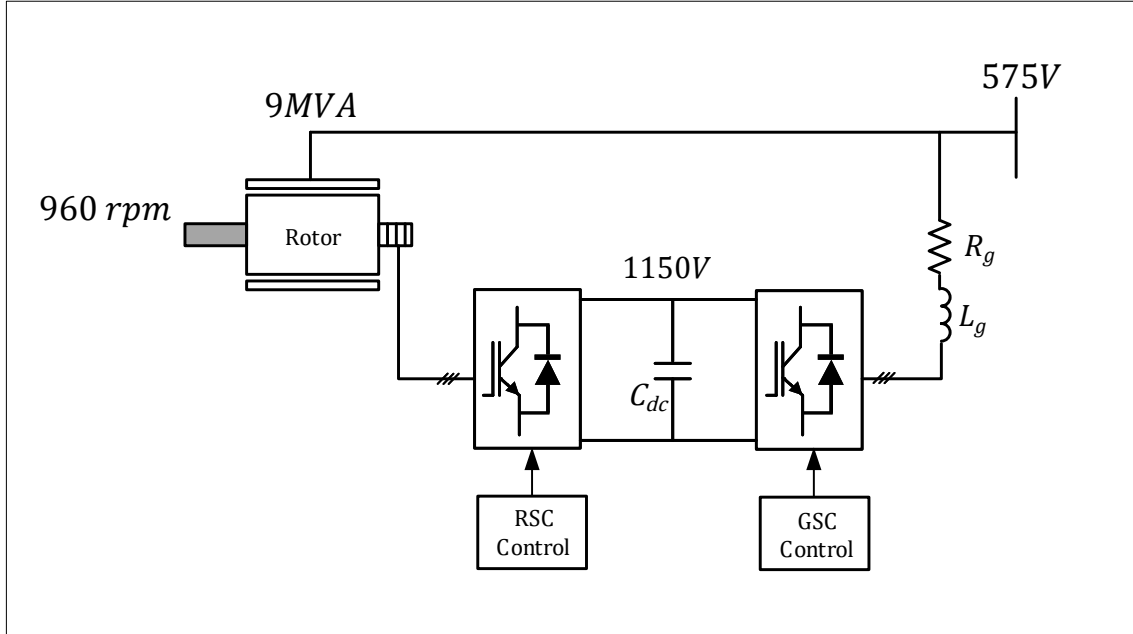


Figure 3.12: MATLAB/SimPowerSystems testbed.

Table 3.2: Model parameters

R_s	0.023(p.u)	friction factor	0	X_g	0.3(p.u)
R_r	0.016(p.u)	pole pairs	3	R_g	0.003(p.u)
X_s	0.18(p.u)	Inertia	0.685	C_{dc}	0.06 (F)
X_r	0.16(p.u)	S_n	9 (MVA)		
X_m	2.9(p.u)	V_n	575 (60Hz)		

The simulation results and FFT analysis results are shown in Fig. 3.13 and Fig. 3.14. The analytical results and the simulation results are compared in Table 3.3. It is found that they agree with each other with a mismatch less than 0.027%.

3.3.3 Current Control Considered

In this section, the steady-state analysis is extended by considering the current control systems of the GSC and RSC, as shown in Fig. 3.15. While in section 3.3.2 the modulation indices are treated as known, in this section, the converter dq -frame voltages are treated as

Table 3.3: Results comparison (constant modulation index)

	Analysis	Simulation	Mismatch	$\frac{\text{analysis-simulation}}{\text{simulation}} \times 100$
\overline{V}_g	0.030656∠ - 2.74	0.030656∠ - 2.90	6E-07	0.00195%
\overline{I}_s	0.462866∠95.72	0.462910∠95.69	4E-05	0.00950%
\overline{I}_g	0.60206∠90.10	0.602015∠90	4E-05	0.00744%
\overline{V}_r	0.008175∠13.75	0.008175∠12.4	2E-07	0.00036%
\overline{I}_r	0.440131∠ - 84.08	0.440177∠ - 84.5	4E-05	0.01026%
$\overline{V}_g^{(3)}$	0.030656∠ - 176.94	0.030656∠ - 177.1	6E-07	0.00195%
$\overline{I}_s^{(3)}$	0.010608∠ - 100.86	0.010608∠ - 101.96	1E-07	0.00131%
$\overline{I}_g^{(3)}$	0.034062∠ - 86.75	0.034062∠ - 88.20	2E-07	0.00073%
$\overline{I}_r^{(3)}$	0.011267∠78.99	0.01127∠77.4	3E-06	0.02661%
$\overline{V}_r^{(3)}$	0.008175∠166.55	0.008175∠165	3E-08	0.00036%
$\overline{V}_{dc}^{(2)}$	0.204375∠ - 89.84	0.204379∠ - 90	3E-06	0.00161%
$\overline{I}_{dc1}^{(2)}$	0.286239∠2.84	0.2862∠2.69	3E-05	0.01380%
$\overline{I}_{dc2}^{(2)}$	0.054146∠172.5	0.054156∠172	9E-06	0.01769%

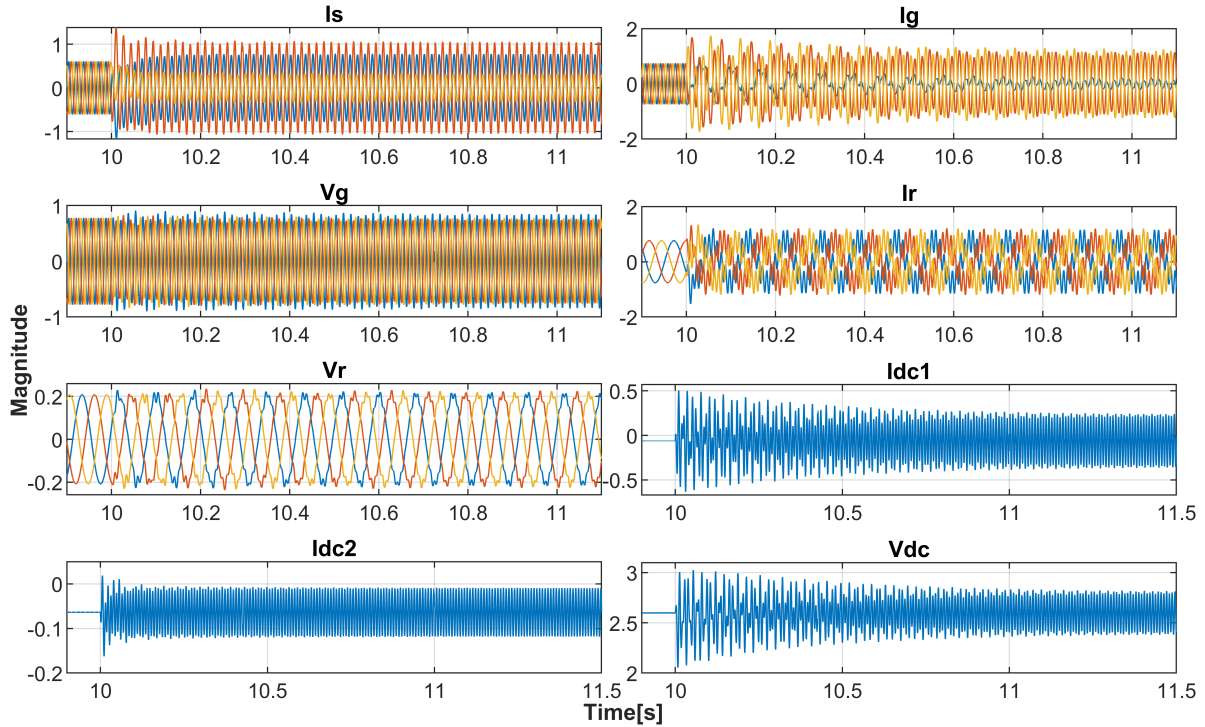


Figure 3.13: Simulation waveforms (constant modulation index).

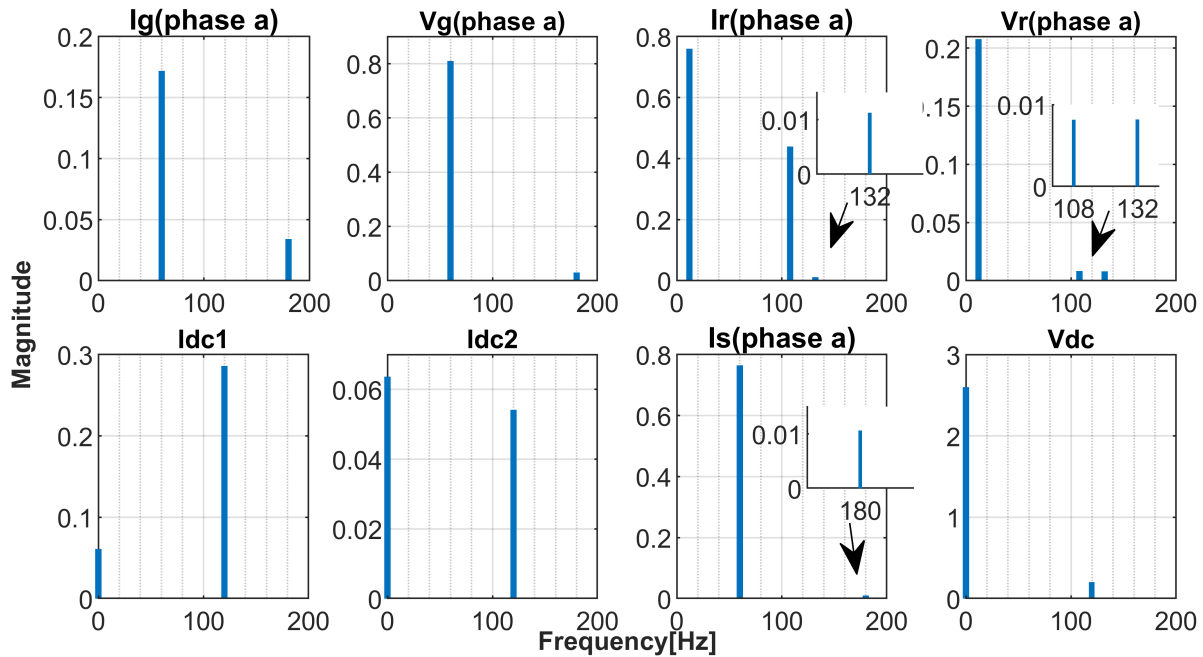


Figure 3.14: FFT analysis (constant modulation index).

unknown variables. Variables associated with dq -frame converter controls have 0 Hz and 120 Hz components under unbalance.

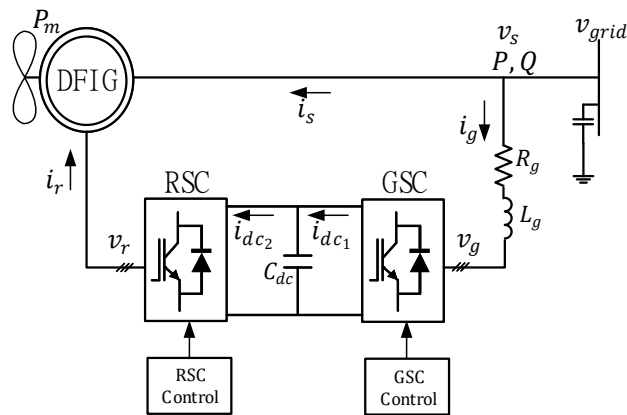


Figure 3.15: Type III WTs (with current control).

To simplify the analysis, only current control loops are considered as shown in Fig. 3.16. In the shown figures, i_{d_r} , i_{q_r} , v_{d_r} and v_{q_r} are the d - and q -axis currents and voltages of the

RSC. i_{d_g} , i_{q_g} , v_{d_g} and v_{q_g} are the d - and q -axis currents and voltages of the GSC. θ_m is the rotor mechanical angle and θ_e is the rotor electrical angle.

By deriving a set of relations between the negative-sequence and 3rd harmonic component quantities of the RSC and GSC from one side and the second harmonic values in the control system from the other side, 18 unknown variables are to be computed. They are listed as follows.

- RSC ac side components: $\bar{V}_r^-, \bar{I}_r^-, \bar{V}_r^{(3)}, \bar{I}_r^{(3)}$
- GSC ac side components: $\bar{V}_g^-, \bar{I}_g^-, \bar{V}_g^{(3)}, \bar{I}_g^{(3)}$
- Stator side ac components: $\bar{I}_s^-, \bar{I}_s^{(3)}$
- RSC controller components: $\bar{V}_{d_r}^{(2)}, \bar{V}_{q_r}^{(2)}, \bar{I}_{d_r}^{(2)}, \bar{I}_{q_r}^{(2)}$
- GSC controller components: $\bar{V}_{d_g}^{(2)}, \bar{V}_{q_g}^{(2)}, \bar{I}_{d_g}^{(2)}, \bar{I}_{q_g}^{(2)}$

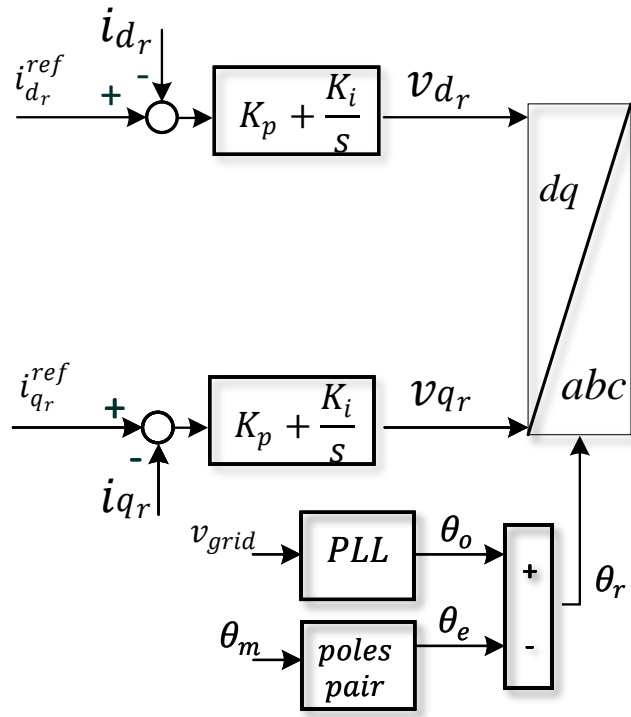
The current orders, $i_{d_g}^{\text{ref}}$, $i_{q_g}^{\text{ref}}$, $i_{d_r}^{\text{ref}}$ and $i_{q_r}^{\text{ref}}$ are supposed to be generated by the slow power control loop when the full control scheme (two-level controller: inner and outer loops) is implemented. Since the outer control loops are omitted in this analysis, the current references $i_{d_g}^{\text{ref}}$, $i_{d_r}^{\text{ref}}$, $i_{q_r}^{\text{ref}}$ are assumed to have DC values and a ripple of $2f_0$ (during unbalanced condition) to simulate some realistic scenarios where the input of the outer loop passes $2f_0$ oscillations. $i_{q_g}^{\text{ref}}$ is assumed to be zero in order to achieve unity power factor at normal operation.

3.3.3.1 DQ to ABC

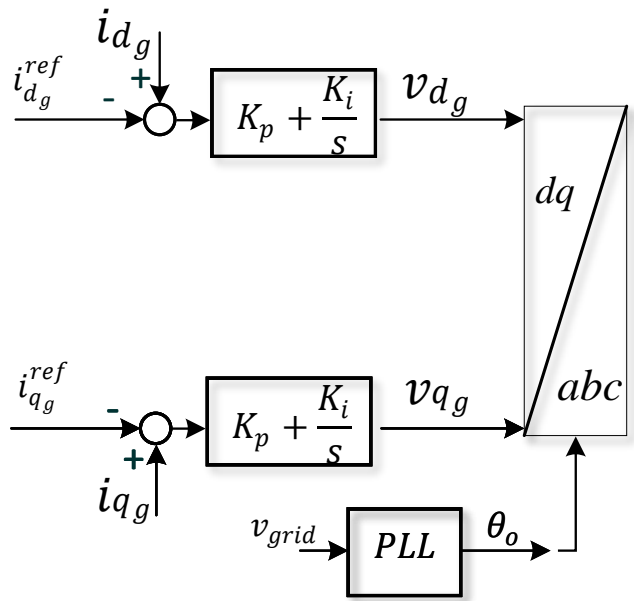
During unbalanced conditions, $2f_0$ Hz oscillations are seen in the control loop. The voltages for the GSC control can be written in the time domain as the following.

$$v_{d_g}(t) = V_{d_g}^{(0)} + V_{d_g}^{(2)} \sin(2\omega_0 t + \theta_{d_g}) \quad (3.28a)$$

$$v_{q_g}(t) = V_{q_g}^{(0)} + V_{q_g}^{(2)} \sin(2\omega_0 t + \theta_{q_g}) \quad (3.28b)$$



(a)



(b)

Figure 3.16: Current control. (A) RSC control scheme. (B) GSC control scheme.

where $V_{d_g}^{(0)}$ and $V_{q_g}^{(0)}$ is the DC components for the d - and q -axes, respectively. $V_{d_g}^{(2)}, V_{q_g}^{(2)}, \theta_{d_g}, \theta_{q_g}$ represent the amplitudes of the oscillating components and the corresponding phase angles, respectively. Using the dq/abc transformation matrix, the voltages of (3.28a)-(3.28b) are transferred to the abc -frame as shown in (3.29).

$$\begin{aligned}
\vec{v}_g &= (v_{d_g} + jv_{q_g})e^{j(\omega_0 t - \frac{\pi}{2})} \\
&= \left(V_{d_g}^{(0)} + \frac{\bar{V}_{d_g}^{(2)} e^{j(2\omega_0 t - \frac{\pi}{2})} - \bar{V}_{d_g}^{(2)*} e^{-j(2\omega_0 t - \frac{\pi}{2})}}{2j} \right) e^{j(\omega_0 t - \frac{\pi}{2})} \\
&\quad + j \left(V_{q_g}^{(0)} + \frac{\bar{V}_{q_g}^{(2)} e^{j(2\omega_0 t - \frac{\pi}{2})} - \bar{V}_{q_g}^{(2)*} e^{-j(2\omega_0 t - \frac{\pi}{2})}}{2j} \right) e^{j(\omega_0 t - \frac{\pi}{2})} \\
&= \underbrace{\left(V_{d_g}^{(0)} + jV_{q_g}^{(0)} \right) e^{j(\omega_0 t - \frac{\pi}{2})}}_{f_0 \text{ Hz}} + \underbrace{\frac{1}{2} \left(-j\bar{V}_{d_g}^{(2)} + \bar{V}_{q_g}^{(2)} \right) e^{j(3\omega_0 t - \frac{\pi}{2})}}_{3f_0 \text{ Hz}} \\
&\quad + \underbrace{\frac{1}{2} \left(-j\bar{V}_{d_g}^{(2)*} + \bar{V}_{q_g}^{(2)*} \right) e^{-j(\omega_0 t - \frac{\pi}{2})}}_{-f_0 \text{ Hz}} \tag{3.29}
\end{aligned}$$

In the phasor-domain, the voltage component can be written as the following.

$$\bar{V}_g^+ = V_{d_g}^{(0)} + jV_{q_g}^{(0)} \tag{3.30a}$$

$$\bar{V}_g^- = \frac{1}{2} \left(j\bar{V}_{d_g}^{(2)} + \bar{V}_{q_g}^{(2)} \right) \tag{3.30b}$$

$$\bar{V}_g^{(3)} = \frac{1}{2} \left(-j\bar{V}_{d_g}^{(2)} + \bar{V}_{q_g}^{(2)} \right) \tag{3.30c}$$

Similarly, the current component can be written in the phasor frame as the following.

$$\bar{I}_g^+ = I_{d_g}^{(0)} + jI_{q_g}^{(0)} \tag{3.31a}$$

$$\bar{I}_g^- = \frac{1}{2} \left(j\bar{I}_{d_g}^{(2)} + \bar{I}_{q_g}^{(2)} \right) \tag{3.31b}$$

$$\bar{I}_g^{(3)} = \frac{1}{2} \left(-j\bar{I}_{d_g}^{(2)} + \bar{I}_{q_g}^{(2)} \right) \tag{3.31c}$$

The voltage references of the RSC in the time domain can be written as the following.

$$v_{d_r}(t) = V_{d_r}^{(0)} + V_{d_r}^{(2)} \sin(2\omega_0 t + \theta_{d_r}) \quad (3.32a)$$

$$v_{q_r}(t) = V_{q_r}^{(0)} + V_{q_r}^{(2)} \sin(2\omega_0 t + \theta_{q_r}) \quad (3.32b)$$

where $V_{d_r}^{(0)}$ and $V_{q_r}^{(0)}$ is the DC components for the dq -axes, respectively. $V_{d_r}^{(2)}$, $V_{q_r}^{(2)}$, θ_{d_r} , θ_{q_r} represent the amplitudes of the oscillating components in the dq -axes and the corresponding phase angles, respectively. Using the dq/abc transformation matrix, the voltages of (3.32a) and (3.32b) are transformed to the abc -frame as shown in (3.33).

$$\begin{aligned} \vec{v}_r &= (v_{d_r} + jv_{q_r})e^{j(\omega_r t - \frac{\pi}{2})} \\ &= \left(V_{d_r}^{(0)} + \frac{\bar{V}_{d_r}^{(2)} e^{j(2\omega_0 t - \frac{\pi}{2})} - \bar{V}_{d_r}^{(2)*} e^{-j(2\omega_0 t - \frac{\pi}{2})}}{2j} \right) e^{j(s\omega_0 t - \frac{\pi}{2})} \\ &\quad + j \left(V_{q_r}^{(0)} + \frac{\bar{V}_{q_r}^{(2)} e^{j(2\omega_0 t - \frac{\pi}{2})} - \bar{V}_{q_r}^{(2)*} e^{-j(2\omega_0 t - \frac{\pi}{2})}}{2j} \right) e^{j(s\omega_0 t - \frac{\pi}{2})} \\ &= \underbrace{\left(V_{d_r}^{(0)} + jV_{q_r}^{(0)} \right) e^{j(\omega_0 t - \frac{\pi}{2})}}_{s f_0 \text{ Hz}} + \underbrace{\frac{1}{2} \left(-j\bar{V}_{d_r}^{(2)} + \bar{V}_{q_r}^{(2)} \right) e^{j((2+s)\omega_0 t - \frac{\pi}{2})}}_{(2+s)f_0 \text{ Hz}} \\ &\quad + \underbrace{\frac{1}{2} \left(-j\bar{V}_{d_r}^{(2)*} + \bar{V}_{q_r}^{(2)*} \right) e^{-j((2-s)\omega_0 t - \frac{\pi}{2})}}_{-(2-s)f_0 \text{ Hz}} \end{aligned} \quad (3.33)$$

In the phasor frame, the voltage component can be written as the following.

$$\bar{V}_r^+ = V_{d_r}^{(0)} + jV_{q_r}^{(0)} \quad (3.34a)$$

$$\bar{V}_r^- = \frac{1}{2} \left(j\bar{V}_{d_r}^{(2)} + \bar{V}_{q_r}^{(2)} \right) \quad (3.34b)$$

$$\bar{V}_r^{(3)} = \frac{1}{2} \left(-j\bar{V}_{d_r}^{(2)} + \bar{V}_{q_r}^{(2)} \right) \quad (3.34c)$$

Similarly, in the phasor frame, the current components can be written as the following.

$$\bar{I}_r^+ = I_{d_r}^{(0)} + jI_{q_r}^{(0)} \quad (3.35a)$$

$$\bar{I}_r^- = \frac{1}{2} \left(j\bar{I}_{d_r}^{(2)} + \bar{I}_{q_r}^{(2)} \right) \quad (3.35b)$$

$$\bar{I}_r^{(3)} = \frac{1}{2} \left(-j\bar{I}_{d_r}^{(2)} + \bar{I}_{q_r}^{(2)} \right) \quad (3.35c)$$

3.3.3.2 Control Signals

The signals in the control systems of the GSC and RSC, shown Fig. 3.16, contain DC and $2f_0$ Hz components. The two frequencies can be treated separately. The reference voltages of the GSC and RSC in the frequency domain can be written as follows, respectively.

$$\bar{V}_{d_g}^{(2)} = - \left(\bar{I}_{d_g}^{\text{ref}(2)} - \bar{I}_{d_g}^{(2)} \right) \bar{G}_{i_{d_g}}^{PI} \quad (3.36a)$$

$$\bar{V}_{q_g}^{(2)} = - \left(\bar{I}_{q_g}^{\text{ref}(2)} - \bar{I}_{q_g}^{(2)} \right) \bar{G}_{i_{q_g}}^{PI} \quad (3.36b)$$

$$\bar{V}_{d_r}^{(2)} = \left(\bar{I}_{d_r}^{\text{ref}(2)} - \bar{I}_{d_r}^{(2)} \right) \bar{G}_{i_{d_r}}^{PI} \quad (3.36c)$$

$$\bar{V}_{q_r}^{(2)} = \left(\bar{I}_{q_r}^{\text{ref}(2)} - \bar{I}_{q_r}^{(2)} \right) \bar{G}_{i_{q_r}}^{PI} \quad (3.36d)$$

$$\text{where } \bar{G}^{PI} = k_p + \frac{k_i}{j2\pi f_0}$$

where k_p and k_i , are the proportional and integral constants, respectively.

3.3.3.3 Validation

To validate the analysis conducted in section 3.3.3, the set of the unknown variables : $\bar{V}_r^-, \bar{I}_r^-, \bar{V}_g^-, \bar{I}_s^-, \bar{V}_r^{(3)}, \bar{I}_r^{(3)}, \bar{V}_g^{(3)}, \bar{I}_s^{(3)}, \bar{I}_g^-, \bar{I}_g^{(3)}, \bar{V}_r^-, \bar{I}_{d_g}^{(2)}, \bar{I}_{q_g}^{(2)}, \bar{I}_{d_r}^{(2)}, \bar{I}_{q_r}^{(2)}, \bar{V}_{d_g}^{(2)}, \bar{V}_{q_g}^{(2)}, \bar{V}_{d_r}^{(2)}, \bar{V}_{q_r}^{(2)}$ are computed using the derived equations in the analysis of section 3.3.3, summarized in Fig. 3.17, and compared with the simulation model.

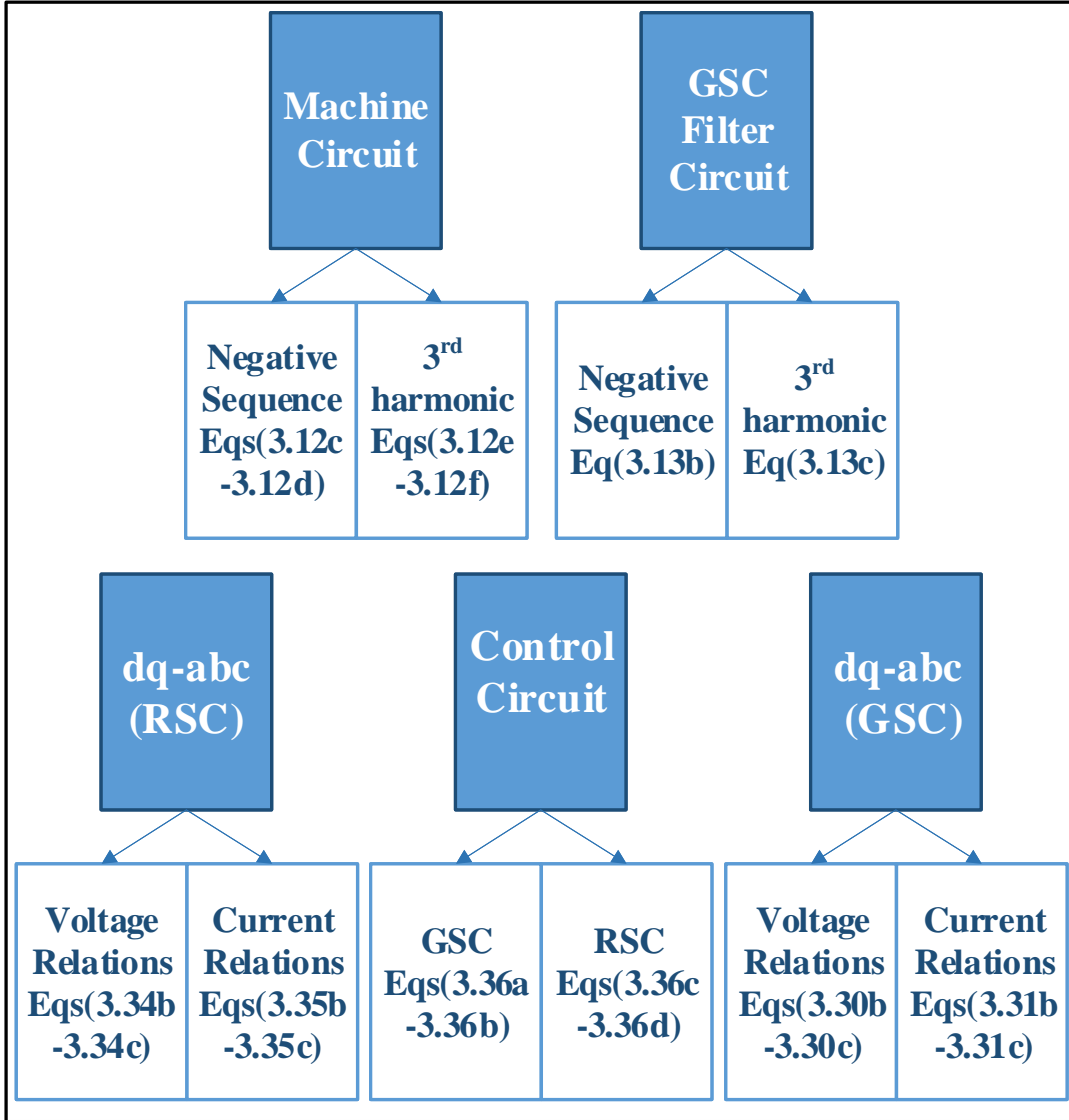


Figure 3.17: Steady-state equations (current control).

Initially, the system is operating at nominal grid voltage ($V_s^+ = 1\angle 0^\circ$ p.u), then unbalance voltage condition occurs at $t = 5$ seconds ($V_s^+ = 1\angle 0^\circ, V_s^- = 0.15\angle 180^\circ$). When the unbalance condition occurs, oscillations of 120 Hz will be introduced to $i_{d_r}^{\text{ref}(2)}$, $i_{q_r}^{\text{ref}(2)}$, $i_{d_g}^{\text{ref}(2)}$ with the values of $0.08\angle -10^\circ$, $0.05\angle -15^\circ$, $0.27\angle -108.82^\circ$, respectively. $i_{q_g}^{\text{ref}}$ is kept zero.

$i_{dg}^{\text{ref}(0)}$ is changed when the unbalance condition occurs to keep the average of the DC-link voltage at its nominal value.

The proportional and integral constants of the GSC and RSC control are $k_p^{idg} = k_p^{iqg} = 0.83$, $k_i^{idg} = k_i^{iqg} = 5$, $k_p^{idr} = k_p^{iqr} = 0.6$, $k_i^{idr} = k_i^{iqr} = 8$. The simulation results are shown in Fig. 3.22 and Fig. 3.23. The analytical and the simulation results are compared in Table 3.5. The analytical results agree with the simulation results.

Table 3.4: Results comparison (inner loops)

	Analysis	Simulation	Mismatch	$\frac{\text{analysis-simulation}}{\text{simulation}} \times 100$
\bar{V}_g	0.158060∠173.47	0.158060∠173.47	8E-08	0.00005%
\bar{I}_s	0.326701∠136.32	0.326663∠136.31	3E-05	0.01141%
\bar{I}_g	0.064330∠ - 158.04	0.064330∠ - 158.04	3E-07	0.00046%
\bar{V}_r	0.187038∠133.38	0.187∠133.4	3E-05	0.02050%
\bar{I}_r	0.313199∠ - 37.29	0.3132∠ - 37.3	9E-07	0.00028%
$\bar{V}_g^{(3)}$	0.083796∠23.53	0.083806∠ - 175.09	1E-05	0.01229%
$\bar{I}_s^{(3)}$	0.029039∠61.14	0.029037∠61.14	2E-06	0.00843%
$\bar{I}_g^{(3)}$	0.093106∠113.72	0.093093∠113.71	1E-05	0.01441%
$\bar{I}_r^{(3)}$	0.030842∠ - 118.99	0.03084∠ - 119	2E-06	0.0075%
$\bar{V}_r^{(3)}$	0.022377∠ - 31.44	0.02238∠ - 31.4	2E-06	0.00987%
$\bar{I}_{dg}^{(2)}$	0.111520∠168.51	0.111516∠168.50	4E-06	0.00412%
$\bar{I}_{qg}^{(2)}$	0.114793∠147.78	0.114776∠147.78	1E-05	0.01533%
$\bar{V}_{dg}^{(2)}$	0.234374∠93.78	0.234387∠93.78	1E-05	0.00563%
$\bar{V}_{qg}^{(2)}$	0.095281∠147.33	0.095267∠147.33	1E-05	0.01543%
$\bar{I}_{dr}^{(2)}$	0.310252∠ - 121.65	0.310218∠ - 121.65	3E-05	0.01108%
$\bar{I}_{qr}^{(2)}$	0.319113∠ - 42.78	0.319076∠ - 42.78	3E-05	0.01168%
$\bar{V}_{dr}^{(2)}$	0.208718∠44.99	0.208699∠44.98	1E-05	0.00919%
$\bar{V}_{qr}^{(2)}$	0.165544∠131.35	0.165523∠131.35	2E-05	0.01286%

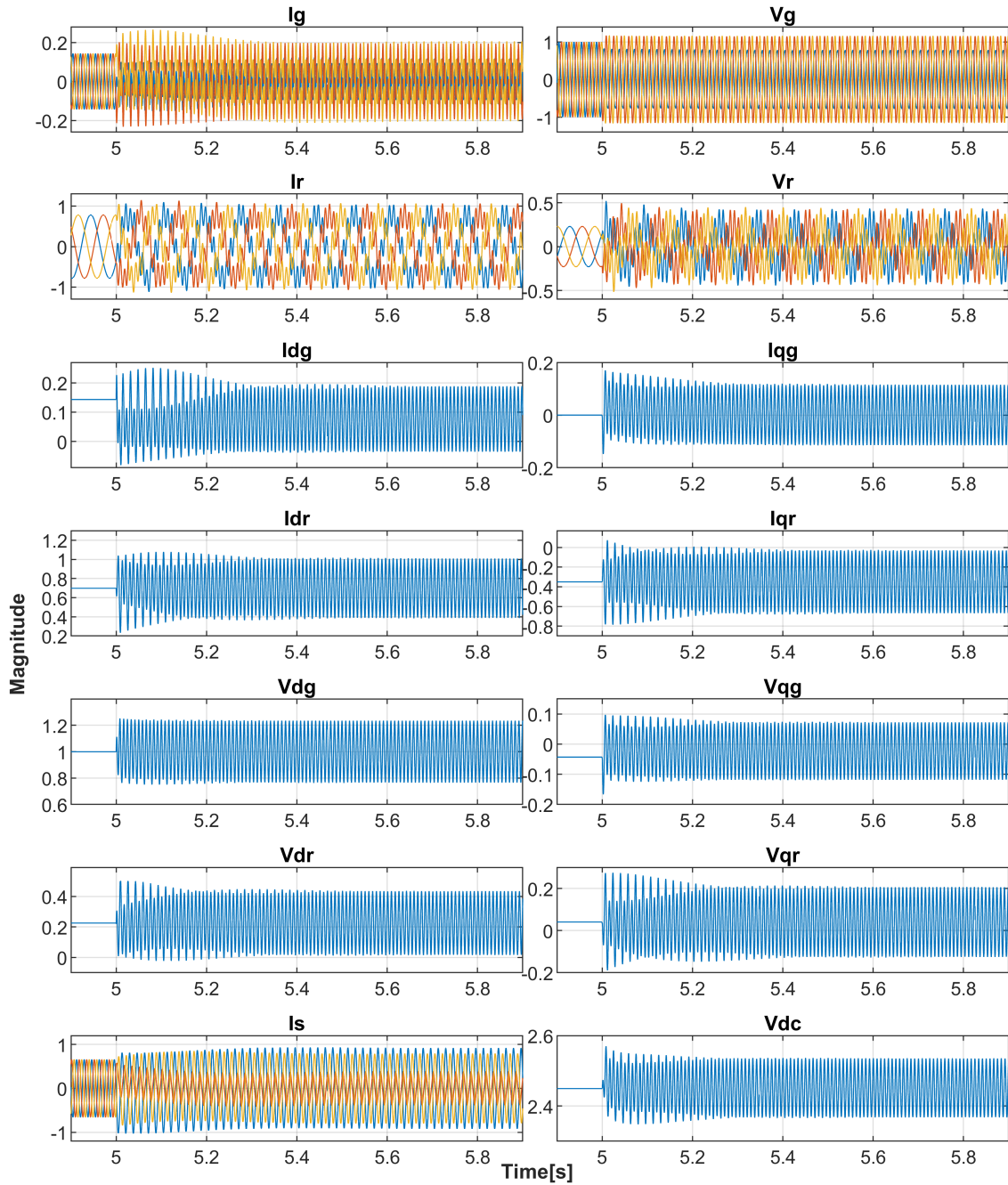


Figure 3.18: Simulation waveforms (current control considered).

3.3.4 Outer Loops Considered

In this section, the steady-state analysis is extended by considering the outer control loops of the RSC and GSC control systems, as shown Fig. 3.20. While in section 3.3.3

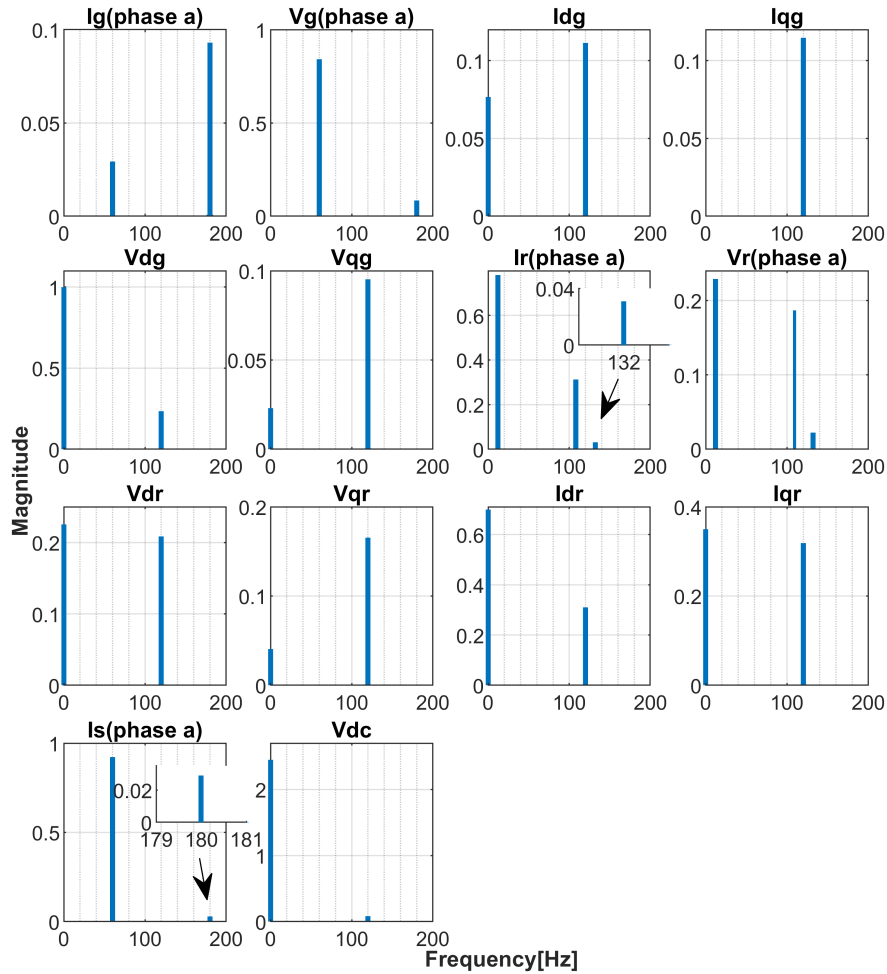
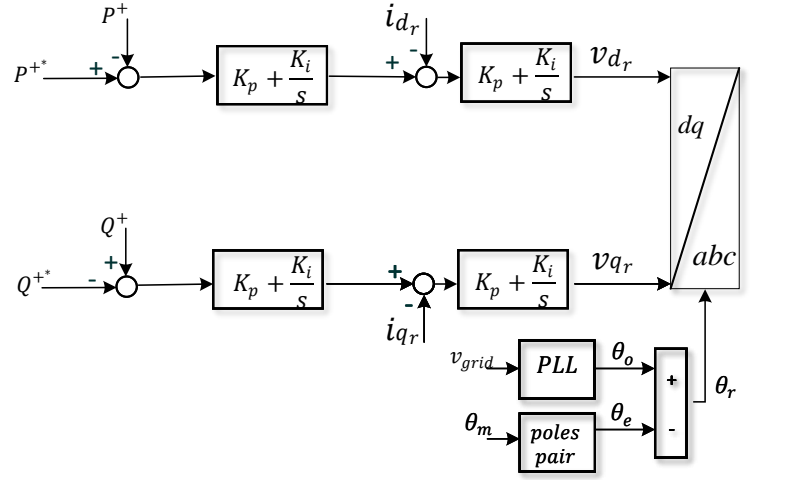


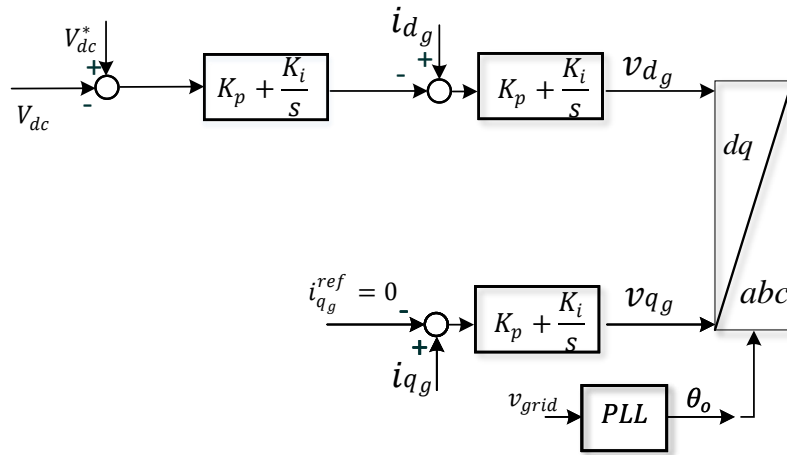
Figure 3.19: FFT analysis (current control considered).

the current references are treated as known, in this section, the converter dq -frame voltages and currents are treated as unknown variables. Variables associated with dq -frame converter controls have DC and AC components under unbalance.

A phasor-domain circuit modeling approach will be presented to compute the positive-, negative-sequence and 3rd harmonic components in the voltage and current waveform during the unbalance grid condition. 24 variables will be found through solving a set of nonlinear equations. The set of the unknown variables related to positive-sequence, negative-sequence, 3rd harmonic components, DC-link and the second harmonic values in the control system are listed as follows:



(a)



(b)

Figure 3.20: Outer control. (A) RSC control scheme. (B) GSC control scheme.

- RSC ac side components: $\bar{V}_r^+, \bar{I}_r^+, \bar{V}_r^-, \bar{I}_r^-, \bar{V}_r^{(3)}, \bar{I}_r^{(3)}$
- GSC ac side components: $\bar{V}_g^+, \bar{I}_g^+, \bar{V}_g^-, \bar{I}_g^-, \bar{V}_g^{(3)}, \bar{I}_g^{(3)}$
- Stator side ac components: $\bar{I}_s^+, \bar{I}_s^-, \bar{I}_s^{(3)}$
- DC-link components: $\bar{V}_{dc}^{(2)}$
- RSC controller components: $\bar{V}_{d_r}^{(2)}, \bar{V}_{q_r}^{(2)}, \bar{I}_{d_r}^{(2)}, \bar{I}_{q_r}^{(2)}$

- GSC controller components: $\bar{V}_{d_g}^{(2)}, \bar{V}_{q_g}^{(2)}, \bar{I}_{d_g}^{(2)}, \bar{I}_{q_g}^{(2)}$

3.3.4.1 GSC Power

The outer loop of GSC control is set to regulate the DC-link capacitor voltage, as shown in Fig. 3.20.b. During the unbalance condition, besides the $2f_0$ component, the DC-link voltage will contain ripples of $4f_0, 6f_0$..etc, which will be passed through the outer loop and lead to generate different harmonics in the AC side voltage. If only the dominant components, positive, negative and third harmonic, are considered, the GSC power during the unbalance condition can be written as (3.37)

$$\begin{aligned}
P_g &= \frac{3}{2} \Re(\vec{v}_g \vec{i}_g^*) \\
&\approx \frac{3}{2} \underbrace{(\bar{V}_g^+ \bar{I}_g^{+*} + \bar{V}_g^{+*} \bar{I}_g^+)}_{0\text{Hz}} + \underbrace{(\bar{V}_g^- \bar{I}_g^{-*} + \bar{V}_g^{-*} \bar{I}_g^-)}_{0\text{Hz}} + \underbrace{(\bar{V}_g^{(3)} \bar{I}_g^{(3)*} + \bar{V}_g^{(3)*} \bar{I}_g^{(3)})}_{0\text{Hz}} \\
&\quad + \underbrace{\bar{V}_g^- \bar{I}_g^+ e^{j(2\omega_0 t - \pi)} + \bar{V}_g^{+*} \bar{I}_g^{+*} e^{-j(2\omega_0 t - \pi)}}_{2f_0\text{Hz}} + \underbrace{\bar{V}_g^+ \bar{I}_g^- e^{j(2\omega_0 t - \pi)} + \bar{V}_g^{+*} \bar{I}_g^{-*} e^{-j(2\omega_0 t - \pi)}}_{2f_0\text{Hz}} \\
&\quad + \underbrace{\bar{V}_g^{(3)} \bar{I}_g^{+*} e^{j(2\omega_0 t)} + \bar{V}_g^{(3)*} \bar{I}_g^+ e^{-j(2\omega_0 t)}}_{2f_0\text{Hz}} + \underbrace{\bar{V}_g^{+*} \bar{I}_g^{(3)} e^{j(2\omega_0 t)} + \bar{V}_g^+ \bar{I}_g^{(3)*} e^{-j(2\omega_0 t)}}_{2f_0\text{Hz}} \\
&\quad + \underbrace{\bar{V}_g^- \bar{I}_g^{(3)} e^{j(4\omega_0 t - \pi)} + \bar{V}_g^{-*} \bar{I}_g^{(3)*} e^{-j(4\omega_0 t - \pi)}}_{4f_0\text{Hz}} + \underbrace{\bar{V}_g^{(3)} \bar{I}_g^- e^{j(4\omega_0 t - \pi)} + \bar{V}_g^{(3)*} \bar{I}_g^{-*} e^{-j(4\omega_0 t - \pi)}}_{4f_0\text{Hz}} \quad (3.37)
\end{aligned}$$

In the phasor frame, the power component can be written as the following.

$$P_g^{(0)} \approx 3 (V_g^+ I_g^+ \cos(\angle \mathbf{E}_g^+ - \angle \mathbf{I}_g^+) + V_g^- I_g^- \cos(\angle \mathbf{E}_g^- - \angle \mathbf{I}_g^-) + V_g^{(3)} I_g^{(3)} \cos(\angle \mathbf{E}_g^{(3)} - \angle \mathbf{I}_g^{(3)})) \quad (3.38a)$$

$$\bar{P}_g^{(2)} \approx 3 (-j \bar{V}_g^- \bar{I}_g^+ + j \bar{V}_g^{(3)} \bar{I}_g^{+*} - j \bar{V}_g^+ \bar{I}_g^- + j \bar{V}_g^{+*} \bar{I}_g^{(3)}) \quad (3.38b)$$

$$\bar{P}_g^{(4)} \approx 3 (-j \bar{V}_g^- \bar{I}_g^{(3)} - j \bar{V}_g^{(3)} \bar{I}_g^-) \quad (3.38c)$$

3.3.4.2 RSC Power

In the given control system shown Fig. 3.20.a, the outer loop is used to regulate the stator active (P^+) and reactive power (Q^+). Positive-sequence quantities are used for the outer loop signals. During the unbalance condition, the outer loop will only contain DC components. The RSC power during the unbalance condition can be written as (3.39).

$$\begin{aligned}
P_r &= \frac{3}{2} \Re \mathbf{e}(\vec{v}_r \vec{i}_r^*) \\
&= \frac{3}{2} \left(\underbrace{\overline{V}_r^+ \overline{I}_r^{+*} + \overline{V}_r^{+*} \overline{I}_r^+}_{0\text{Hz}} + \underbrace{\overline{V}_g^- \overline{I}_g^- + \overline{V}_g^{-*} \overline{I}_r^-}_{0\text{Hz}} + \underbrace{\overline{V}_r^{(3)} \overline{I}_r^{(3)*} + \overline{V}_r^{(3)*} \overline{I}_r^{(3)}}_{0\text{Hz}} \right. \\
&\quad + \underbrace{\overline{V}_r^- \overline{I}_r^+ e^{j(2\omega_0 t - \pi)} + \overline{V}_r^{-*} \overline{I}_r^{+*} e^{-j(2\omega_0 t - \pi)}}_{2f_0\text{Hz}} + \underbrace{\overline{V}_r^+ \overline{I}_r^- e^{j(2\omega_0 t - \pi)} + \overline{V}_r^{+*} \overline{I}_r^{-*} e^{-j(2\omega_0 t - \pi)}}_{2f_0\text{Hz}} \\
&\quad + \underbrace{\overline{V}_r^{(3)} \overline{I}_r^{+*} e^{j(2\omega_0 t)} + \overline{V}_r^{(3)*} \overline{I}_r^+ e^{-j(2\omega_0 t)}}_{2f_0\text{Hz}} + \underbrace{\overline{V}_r^+ \overline{I}_r^{(3)*} e^{j(2\omega_0 t)} + \overline{V}_r^{+*} \overline{I}_r^{(3)} e^{-j(2\omega_0 t)}}_{2f_0\text{Hz}} \\
&\quad \left. + \underbrace{\overline{V}_r^- \overline{I}_r^{(3)*} e^{j(4\omega_0 t - \pi)} + \overline{V}_r^{-*} \overline{I}_r^{(3)} e^{-j(4\omega_0 t - \pi)}}_{4f_0\text{Hz}} + \underbrace{\overline{V}_r^{(3)} \overline{I}_r^- e^{j(4\omega_0 t - \pi)} + \overline{V}_r^{(3)*} \overline{I}_r^{-*} e^{-j(4\omega_0 t - \pi)}}_{4f_0\text{Hz}} \right) \quad (3.39)
\end{aligned}$$

In the phasor frame, the power component can be written as the following.

$$P_r^{(0)} = 3 \left(V_r^+ I_r^+ \cos(\mathbf{E}_r^+ - \mathbf{I}_r^+) + V_r^- I_r^- \cos(\mathbf{E}_r^- - \mathbf{I}_r^-) + V_r^{(3)} I_r^{(3)} \cos(\mathbf{E}_r^{(3)} - \mathbf{I}_r^{(3)}) \right) \quad (3.40a)$$

$$P_r^{(2)} = 3 \left(-j \overline{V}_r^- \overline{I}_r^+ + j \overline{V}_r^{(3)} \overline{I}_r^{+*} - j \overline{V}_r^+ \overline{I}_r^- + j \overline{V}_r^{+*} \overline{I}_r^{(3)} \right) \quad (3.40b)$$

$$P_r^{(4)} = 3 \left(-j \overline{V}_r^- \overline{I}_r^{(3)*} - j \overline{V}_r^{(3)} \overline{I}_r^- \right) \quad (3.40c)$$

3.3.4.3 DC-Link Power

The DC-link power can be derived as the following.

$$P_{dc} = P_g - P_r \quad (3.41)$$

Considering the DC and $2f_0$ components, in phasor-domain, (3.41) can be written as the following.

$$P_{dc}^{(0)} = P_g^{(0)} - P_r^{(0)} \quad (3.42a)$$

$$\overline{P}_{dc}^{(2)} = \overline{P}_g^{(2)} - \overline{P}_r^{(2)} \quad (3.42b)$$

For the 0 Hz component, the capacitor is open circuited, so (3.42a) can be re-written as the following.

$$P_g^{(0)} = P_r^{(0)} \quad (3.43)$$

For the $2f_0$ Hz component, the relation in (3.42b) can be re-written as the following.

$$j2\omega_0 C_{dc} \overline{V}_{dc}^{(2)} V_{dc}^{(0)} = \overline{P}_g^{(2)} - \overline{P}_r^{(2)} \quad (3.44)$$

3.3.4.4 Control Signals

The reference voltages of the GSC and RSC, shown in Fig. 3.20, in the frequency domain, can be written as follows, respectively.

$$\overline{V}_{dg}^{(2)} = \left(\overline{V}_{dc}^{(2)} \overline{G}_{dc}^{PI} + \overline{I}_{dg}^{(2)} \right) \overline{G}_{i_{dg}}^{PI} \quad (3.45a)$$

$$\overline{V}_{qg}^{(2)} = \overline{I}_{qg}^{(2)} \overline{G}_{i_{qg}}^{PI} \quad (3.45b)$$

$$\overline{V}_{dr}^{(2)} = -\overline{I}_{dr}^{(2)} \overline{G}_{i_{dr}}^{PI} \quad (3.45c)$$

$$\overline{V}_{qr}^{(2)} = -\overline{I}_{qr}^{(2)} \overline{G}_{i_{qr}}^{PI} \quad (3.45d)$$

3.3.4.5 Controller Target

The outer loop of the GSC control is set to regulate the DC-link capacitor voltage and provides unity power factor, while the control of the RSC is set to regulate the stator active

(P^+) and reactive power (Q^+). At steady-state conditions, the following equations are satisfied.

$$P^{+*} - V_s^+ I_s^+ \cos(\theta_s^+ - \phi_s^+) = 0 \quad (3.46a)$$

$$Q^{+*} - V_s^+ I_s^+ \sin(\theta_s^+ - \phi_s^+) = 0 \quad (3.46b)$$

$$V_s^+ I_g^+ \sin(\theta_s^+ - \phi_g^+) = 0 \quad (3.46c)$$

$$V_{dc}^{(0)} - V_{dc}^{(0)*} = 0 \quad (3.46d)$$

3.3.4.6 Validation

To validate the analysis conducted in Section 3.3.4, the set of the unknown variables: $\bar{V}_r^+, \bar{I}_r^+, \bar{V}_g^+, \bar{I}_s^+, \bar{V}_r^-, \bar{I}_r^-, \bar{V}_g^-, \bar{I}_s^-, \bar{V}_r^{(3)}, \bar{I}_r^{(3)}, \bar{V}_g^{(3)}, \bar{I}_s^{(3)}, \bar{I}_g^-, \bar{I}_g^{(3)}, \bar{V}_r^-, \bar{I}_{dg}^{(2)}, \bar{I}_{qg}^{(2)}, \bar{I}_{dr}^{(2)}, \bar{I}_{qr}^{(2)}, \bar{V}_{dg}^{(2)}, \bar{V}_{qg}^{(2)}, \bar{V}_{dr}^{(2)}, \bar{V}_{qr}^{(2)}, \bar{V}_{dc}^{(2)}$ are computed using the derived equations in the analysis, summarized in Fig. 3.21, and compared with the simulation model. In this section, YALMIP is used to solve the non-linear equations through a non-linear programming solver `ipopt`.

Initially, the system is operating at nominal grid voltage ($V_s^+ = 1\angle 0^\circ$ p.u), then unbalance voltage condition occurs at $t = 5$ seconds ($V_s^+ = 1\angle 0^\circ, V_s^- = 0.15\angle 180^\circ$). The proportional and integral constants of the GSC and RSC control are $k_p^{i_{dg}} = k_p^{i_{qg}} = 0.83, k_i^{i_{dg}} = k_i^{i_{qg}} = 5, k_p^{i_{dr}} = 6, k_p^{i_{qr}} = 0.42, k_i^{i_{dr}} = 8, k_i^{i_{qr}} = 5.6, k_p^{dc} = 8, k_i^{dc} = 400, k_p^P = k_p^Q = 0.5, k_i^P = k_i^Q = 8$. The active and reactive power references are $P^{+*} = 0.55, Q^{+*} = 0$. The simulation results are shown in Fig. 3.22 and Fig. 3.23. The analytical and the simulation results are compared in Table 3.5. It is found that they agree with each other with a mismatch less than 3%.

3.4 Conclusion

In this chapter, the occurrence of the 3rd harmonic in Type-III WTs under unbalance is proven mathematically. An efficient algorithm has been designed for the steady-state analysis

of a DFIG-based Type-III WTs under unbalance. Harmonic circuit analysis of the induction machine with the RSC, the DC-link, and the GSC AC side circuit has been carried out. Furthermore, the relationships between the DC and AC sides variables of the two DC/AC converters are investigated. A set of algebraic equations is formed to carry out a steady-state analysis, leading to the calibration of harmonic components in Type-III WTs. The results from the algorithm have been validated via EMT simulation results.

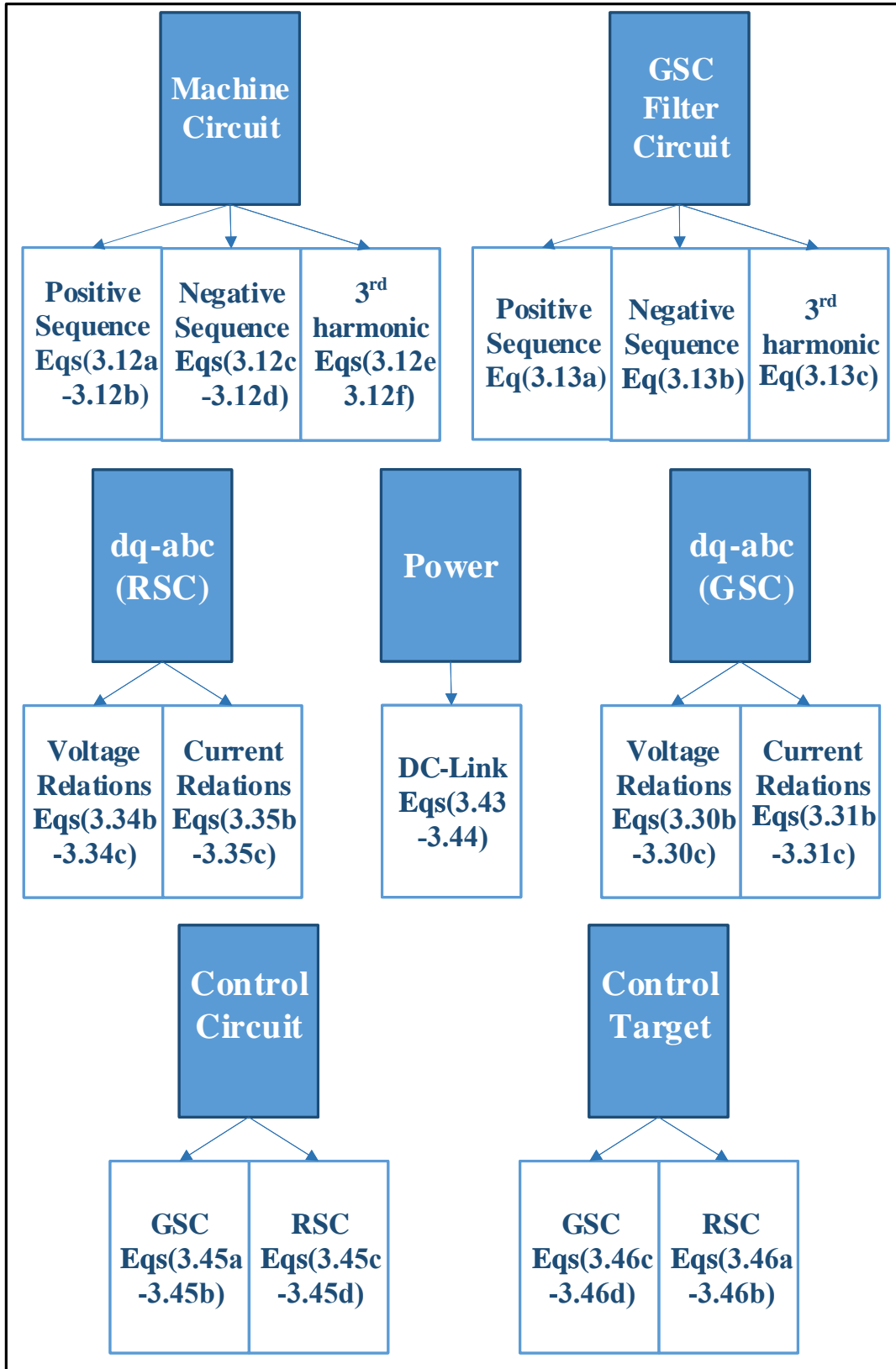


Figure 3.21: Steady-state equations (two-level controller).

Table 3.5: Results comparison (two-level controller)

	Analysis	Simulation	Mismatch	$\frac{\text{analysis-simulation}}{\text{simulation}} \times 100$
\bar{V}_g^+	1.000023∠ - 1.268	1.000023∠ - 1.269	0	0%
\bar{I}_s^+	0.623765∠180	0.62383426∠179.99	6.9E-05	0.01110%
\bar{I}_g^+	0.073765∠0	0.07383427∠0	6.9E-05	0.09381%
\bar{V}_r^+	0.22786265∠9.6148	0.2278650∠9.6	2.3E-06	0.00103%
\bar{I}_r^+	0.7491493∠ - 27.83	0.7492141∠ - 27.830	6.4E-05	0.00864%
\bar{V}_g^-	0.161894∠171.086	0.162617391∠171.19	7.2E-4	0.44484%
\bar{I}_s^-	0.331317∠128.32	0.3312757∠128.317	4.1E-05	0.01246%
\bar{I}_g^-	0.089935∠ - 157.81	0.09028446∠ - 156.15	3.49E-04	0.38706%
\bar{V}_r^-	0.1578517∠133.538	0.1578∠133.5	5.17E-05	0.03276%
\bar{I}_r^-	0.3126913∠ - 46.27	0.3127∠ - 46.3	8.7E-06	0.00278%
$\bar{V}_g^{(3)}$	0.077232∠12.609	0.07879711∠12.07	1.56E-03	1.98625%
$\bar{I}_s^{(3)}$	0.029535∠79.929	0.0295290∠79.92	6E-06	0.02031%
$\bar{I}_g^{(3)}$	0.085813∠102.8	0.087528474∠102.26	1.71E-3	1.95990%
$\bar{V}_r^{(3)}$	0.0227598∠ - 12.658	0.02276∠ - 12.69	2E-07	0.00087%
$\bar{I}_r^{(3)}$	0.0313688∠ - 100.213	0.03136∠ - 100.2	8.8E-06	0.02806%
$\bar{I}_{d_g}^{(2)}$	0.1340516∠151.35	0.1377859∠152.33	3.73E-3	2.71021%
$\bar{I}_{q_g}^{(2)}$	0.1137309∠154.07	0.112428∠154.143	1.30E-3	1.15887%
$\bar{V}_{d_g}^{(2)}$	0.235452∠87.99	0.2379041∠87.97	2.45E-3	1.03070%
$\bar{V}^{(2)}$	0.094399∠153.61	0.0933183∠153.68	1.08E-3	1.15807%
$\bar{I}_{d_r}^{(2)}$	0.2953157∠ - 131.35	0.29528172∠ - 131.354	3.4E-05	0.01150%
$\bar{I}_{q_r}^{(2)}$	0.332127∠ - 50.65	0.3320814∠ - 50.65	4.5E-05	0.01373%
$\bar{V}_{d_r}^{(2)}$	0.1772171∠47.63	0.1771966∠47.63	2E-05	0.01156%
$\bar{V}^{(2)}$	0.13951517∠128.33	0.139496∠128.32	1.917E-05	0.01374%
$\bar{V}_{DC}^{(2)}$	0.077163∠60.26	0.078714∠63.527	1.55E-3	1.97042%

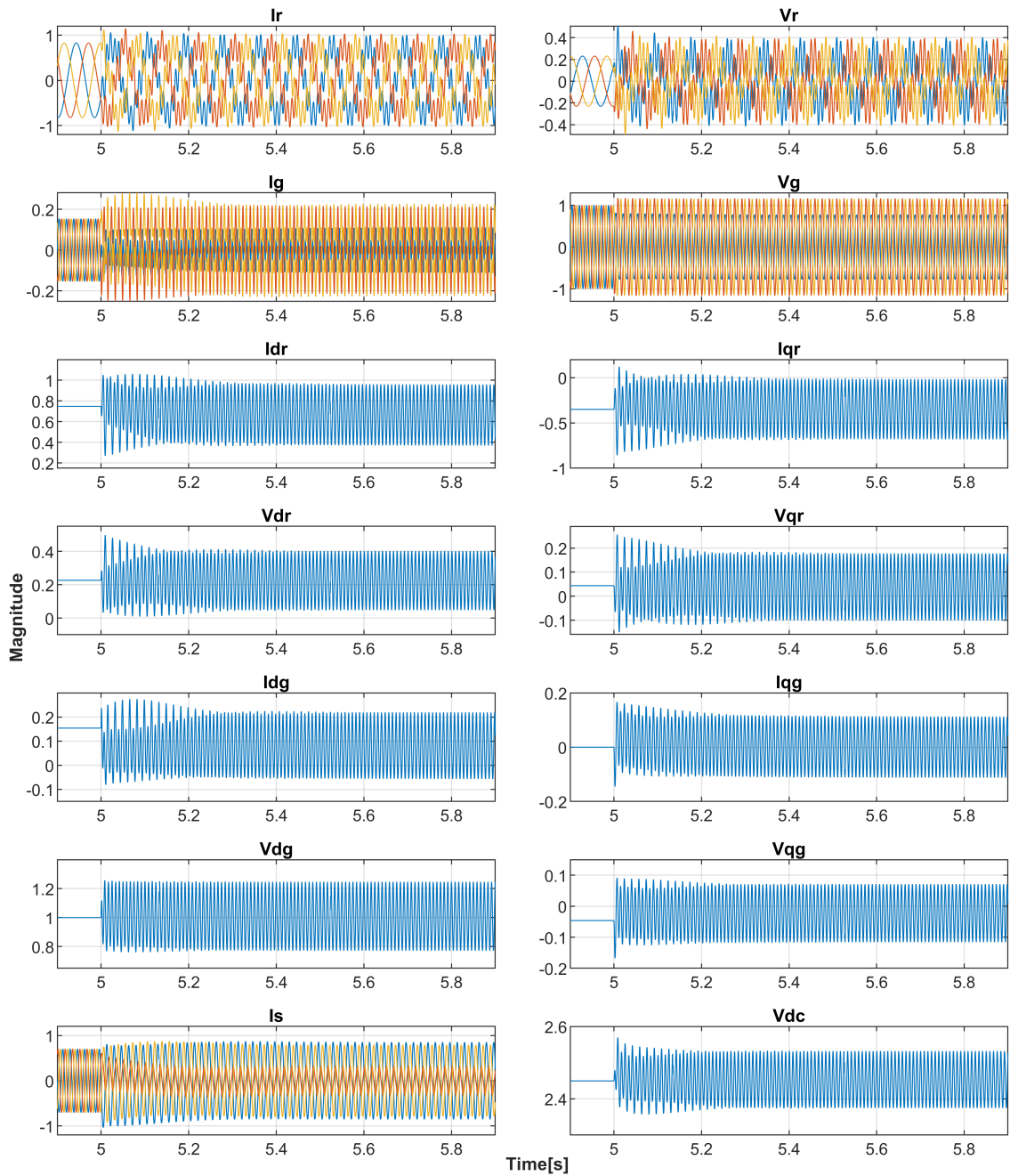


Figure 3.22: Simulation waveforms (two-level controller).

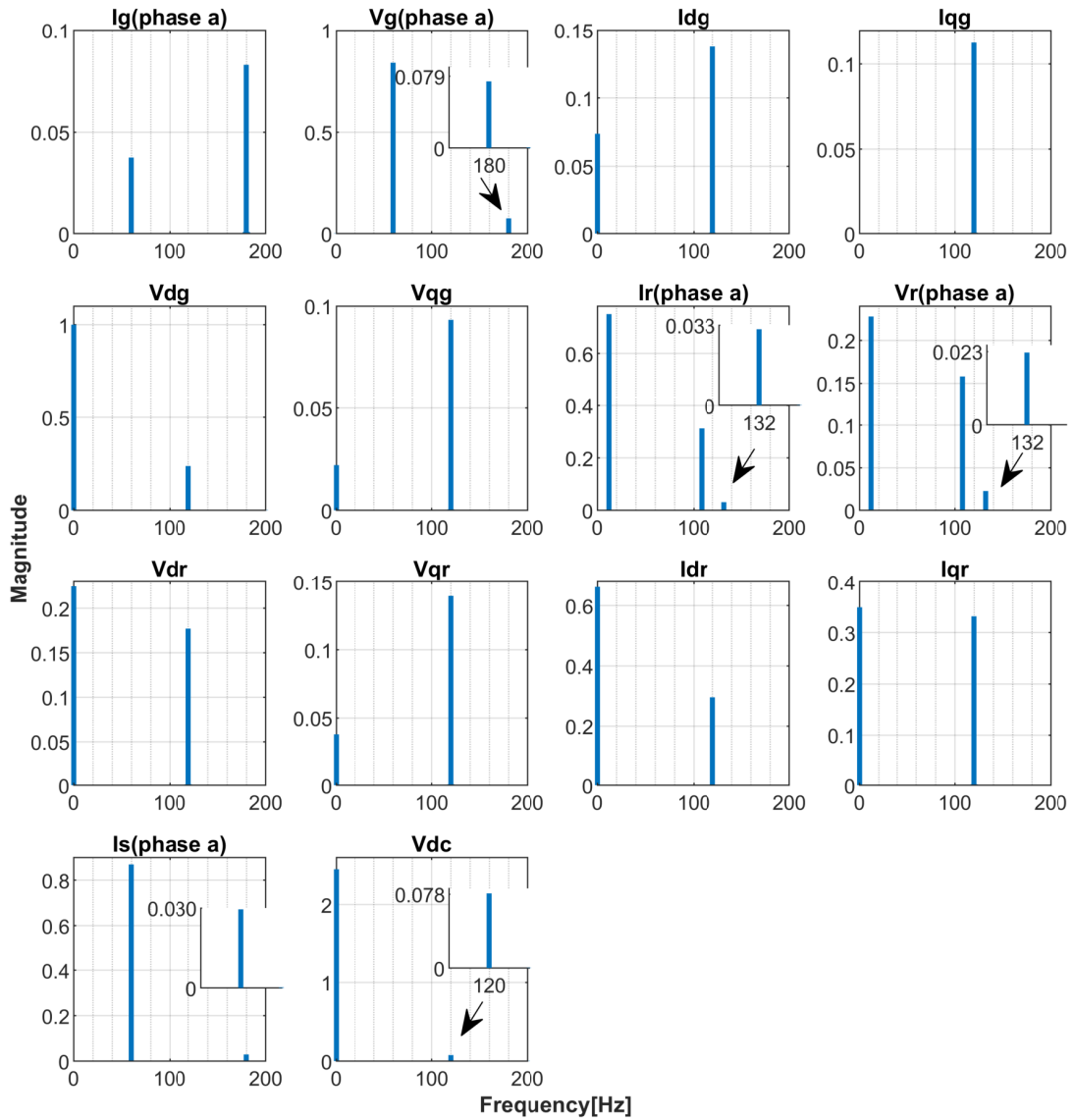


Figure 3.23: FFT analysis (two-level controller).

Chapter 4: Mixed Integer Programming-Based Modeling

4.1 Introduction

In this chapter³, two Mixed-Integer Programming (MIP) problems are formulated to address two issues in power systems. In the first part of the chapter, a mixed-integer non-linear programming (MINLP) problem is formulated to model the behavior of Type-III WTs considering the current limits imposed by the control system. A one-step algorithm is developed to compute the steady-state operating point of Type-III WTs for various balanced stator voltage levels. For a given stator voltage and wind speed, the electrical and mechanical variables of the system can be computed. Lossy DFIG back-to-back converters are considered. The proposed method is validated with electromagnetic transient (EMT) simulations. The significance of this research compared to state-of-the art is a much more accurate computation model for DFIG.

Another application of MIP in power system is discussed in section 4.3. MIP is introduced to the field of fault location identification. Binary variables are introduced to indicate whether a bus is subject to fault. From there, an efficient mixed integer linear programming (MILP) formulation is formulated to identify fault location, fault type and fault currents. This formulation is then extended for application in unbalanced distribution systems. The proposed algorithm shows high accuracy rate for many challenging scenarios.

³Part of this chapter was published in International Transactions on Electrical Energy Systems [61], 2021 and North American Power Symposium [62], 2018. Permissions are included in Appendix A.

4.2 MIP Formulation for Type-III WT's Modeling

In this section, a MINLP problem is formulated to calculate the steady-state variables of the Type-III WT's considering the control system behavior under balanced stator voltage conditions.

4.2.1 System Configuration

The Type-III WT model considered in this chapter is similar to the system adopted in chapter 2 (Testbed-B), shown in Fig .4.1. The steady-state model of DFIG-based WT's, converters currents limits, and control modes are previously discussed in chapter 2 in section 2.3.1, section 2.3.2.1, and section 2.3.2.3, respectively.

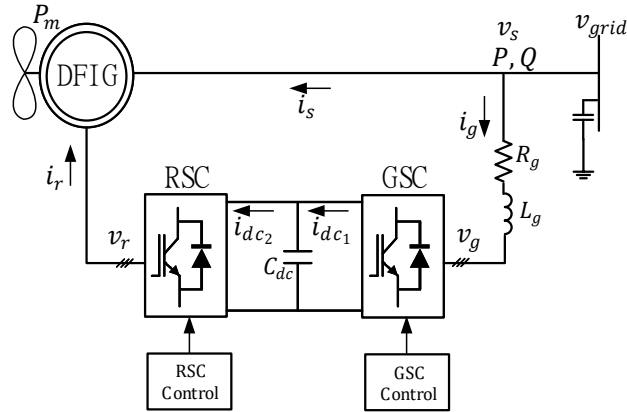


Figure 4.1: Type-III WT's.

4.2.1.1 Control System

The RSC control implemented in this chapter is shown in Fig. 4.2. $i_{dr}, i_{qr}, v_{dr}, v_{qr}$ are DFIG rotor currents and voltages on the d and q axes, respectively. θ_m is the rotor mechanical angle, and θ_e is the rotor electrical angle.

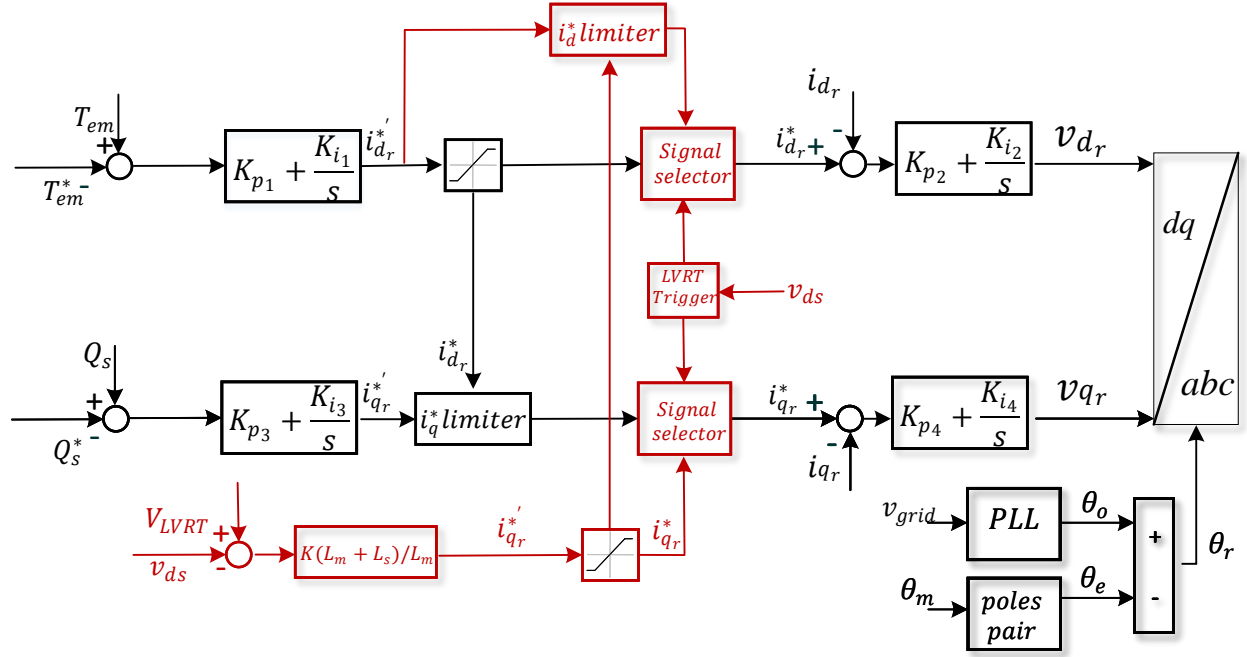


Figure 4.2: RSC control.

The control of RSC is achieved using a two-level controller: fast inner loops and slow outer loops. The inner loops are used to calculate the voltage references in order to generate the modulation index. The slow outer loops are used to calculate the current references i_{dr}^* , i_{qr}^* . In the given control system, the outer loops regulate the electromagnetic torque (T_{em}) and the stator reactive power (Q_s). The two controls are implemented by referring all AC quantities to a synchronous reference frame oriented with the stator voltage as adopted in [55]. That is $v_{ds} = |\bar{V}_s|$ and $v_{qs} = 0$,

A similar technique is used for the GSC controls, as shown in Fig. 4.3. i_{dg} , i_{qg} , v_{dg} , v_{qg} are grid-side-converter currents and voltages on the d and q axes, respectively. The outer loops of the control regulate the DC-link capacitor voltage (V_{dc}) and reactive power (Q_g).

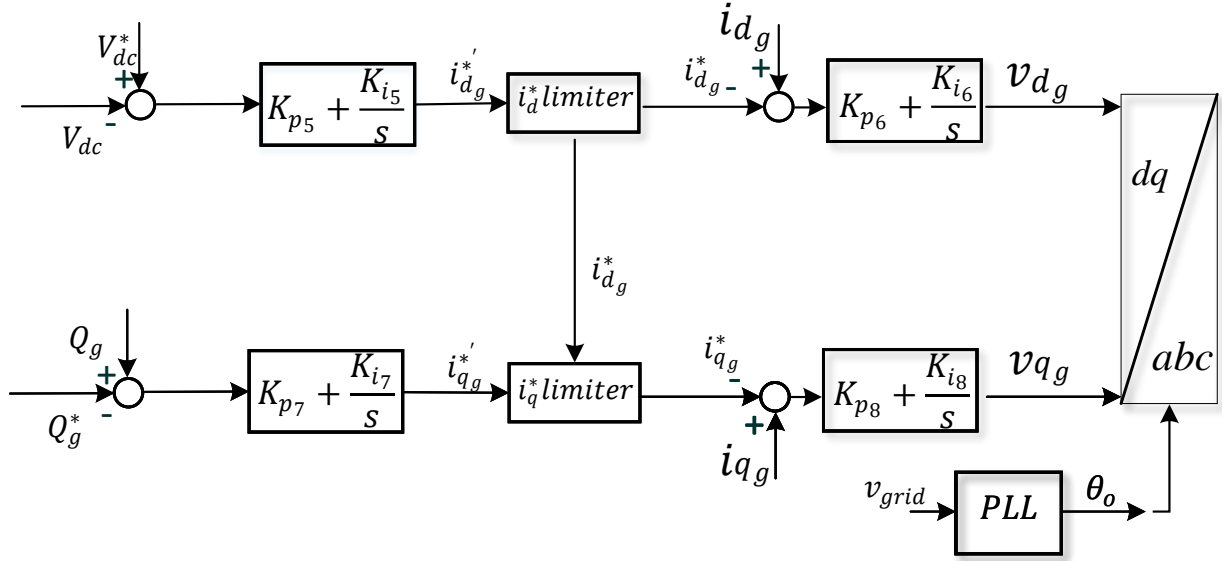


Figure 4.3: GSC control.

4.2.1.2 LVRT Function

When the stator voltage is below a certain value (V_{LVRT}), the behavior of the control system of RSC changes, and the low voltage ride-through function is activated. The Q control will be deactivated, and the WT will generate a reactive current component proportional to the voltage drop. It should be noted that the FRT function is essential for the WTs operating under the Q-control to comply with the grid code requirements regarding the voltage support. During that mode, the reactive current reference is calculated based on equation (4.1). A similar control scheme (FRT function) has been adopted in [29, 63–67].

$$i_{qr}^* = K(V_{LVRT} - v_{ds}) \quad (4.1)$$

K is the proportional gain.

When the LVRT mode is activated, the RSC controller will target satisfying equation (4.1) to comply with the grid code requirement while minimizing the error of equation (2.17a)

4.2.2 Optimization Problem Formulation

The main challenge in finding the steady-state variable of the DFIG based WT is identifying the operating mode of the control systems for a given stator voltage. Once the operating mode of the control system is known, an adequate algorithm can be designed to find the operating point of the DFIG. Fig. 4.4 shows the possible combinations of the operating mode for the RSC and GSC converters. The DFIG may operate in one of six combinations based on the settings of the controllers and the stator voltage. For the adopted control scheme, the DC-link voltage keep increasing once the active current in the GSC hits the limits as no protection scheme is adopted on the DC-link. The wind turbine is assumed to not operate in this region, so no calculations were conducted. This case will be addressed in future research. If Mode-A and Mode-B can be merged and modeled using one formulation,

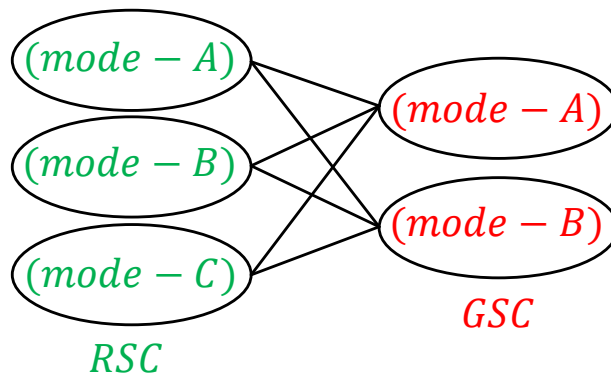


Figure 4.4: Operating modes combinations.

the possibilities in Fig. 4.4 are reduced as show in Fig. 4.5. Only two possibilities can be considered. If only Mode-A and Mode-B of the RSC controller are considered, the behavior of the controller and the current limiters can be modeled using optimization problems with equality and inequality constraints as the following:

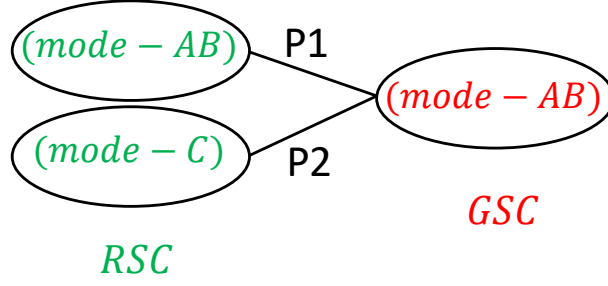


Figure 4.5: Reduced operating modes combinations.

- Mode-A

$$\begin{aligned}
 & \text{minimize} \quad (0) \\
 & \text{subject to} \quad (X_m(i_{qs}i_{dr} - i_{ds}i_{qr})) - T_{em}^* = 0 \\
 & \quad \quad \quad (-v_{ds}i_{qs} - Q_s^*) = 0 \\
 & \quad \quad \quad i_{qr}^2 + i_{dr}^2 < I_r^{limit^2}
 \end{aligned} \tag{4.2}$$

- Mode-B

$$\begin{aligned}
 & \text{minimize} \quad |-v_{ds}i_{qs} - Q_s^*| \\
 & \text{subject to} \quad (X_m(i_{qs}i_{dr} - i_{ds}i_{qr})) - T_{em}^* = 0 \\
 & \quad \quad \quad i_{qr}^2 + i_{dr}^2 = I_r^{limit^2}
 \end{aligned} \tag{4.3}$$

Both optimization problems can be merged into one formulation modeling both modes as the following.

- Mode-AB

$$\begin{aligned}
 & \text{minimize} \quad |-v_{ds}i_{qs} - Q_s^*| \\
 & \text{subject to} \quad (X_m(i_{qs}i_{dr} - i_{ds}i_{qr})) - T_{em}^* = 0 \\
 & \quad \quad \quad i_{qr}^2 + i_{dr}^2 \leq I_r^{limit^2}
 \end{aligned} \tag{4.4}$$

For the GSC, no information about the DC-link voltage reference is in the formulation. Instead, the power balance equation between the RSC and GSC is used. Mode-A and Mode-B can be merged into one formulation easily.

4.2.2.1 Scenario-P1 Modeling

In this section, an optimization problem is formulated to model the DFIG-based WT when the controllers of the RSC and GSC are operating in Mode-A or Mode-B (P1 in Fig. 4.5). The objective function of the optimization problem is the minimization of the absolute error of the control system equations (2.16-2.18b) (the un-prioritized quantities). The constraints of the optimization problem include the steady-state circuit, power and torque equations. The behavior of the current limiters is incorporated in the optimization problem using inequality constraints. The decision variables are the stator currents, rotor currents, GSC currents, rotor voltages, DFIG active power, DFIG mechanical power and the slip ($i_{ds}, i_{qs}, i_{dr}, i_{qr}, i_{dg}, i_{qg}, v_{dr}, v_{qr}, s, P, P_m$). The inputs of the optimization problem are the stator voltage and wind speed.

Please note that the torque equation (2.17a) is added as an equality constraint, while the reactive power equation (2.18b) is added in the objective function. The reason is to ensure that the priority is given for torque (T_{em}) in this operating region.

$$\begin{aligned}
& \text{minimize} && | -v_{ds}i_{qs} - Q_s^* | + | -v_{ds}i_{qg} - Q_g^* | \\
& \text{subject to} && (2.7 - 2.8), (2.10) \\
& && (X_m(i_{qs}i_{dr} - i_{ds}i_{qr}) - T_{em}^*) = 0 \\
& && i_{qr}^2 + i_{dr}^2 \leq I_r^{limit^2} \\
& && i_{qg}^2 + i_{dg}^2 \leq I_g^{limit^2} \\
& && -1 \leq s \leq 0
\end{aligned} \tag{4.5}$$

4.2.2.2 Scenario-P2 Modeling

In this section, an optimization problem is formulated to model the DFIG-based WT when the controller of the RSC operates in mode-C while the GSC converter operates in

Mode-A or Mode-B (P2 in Fig. 4.5). The objective function of the optimization problem is the minimization of the absolute error of the GSC reactive power equations and the electromagnetic torque equations (2.16-2.18a). The constraints of the optimization problem include the steady-state circuit and power equations. The behavior of the current limiters is incorporated in the optimization problem using equality and inequality constraints. The decision variables are $(i_{ds}, i_{qs}, i_{dr}, i_{qr}, i_{dg}, i_{qg}, v_{dr}, v_{qr}, s, P, P_m)$. The input of the optimization problem are the stator voltage and wind speed.

$$\begin{aligned}
& \text{minimize} && | -v_{ds}i_{qs} - Q_s^* | + | X_m(i_{qs}i_{dr} - i_{ds}i_{qr}) - T_{em}^* | \\
& && + | -v_{ds}i_{qg} - Q_g^* | \\
& \text{subject to} && (2.7 - 2.8), (2.10) \\
& && i_{dr}^2 = I_r^{limit^2}, i_{qr} = 0 \\
& && i_{qg}^2 + i_{dg}^2 \leq I_g^{limit^2} \\
& && -1 \leq s \leq 0
\end{aligned} \tag{4.6}$$

Please note that the torque equation is now a part of the objective function. The priority is ensured to be given to the active current using the additional constraints ($i_{qr} = 0, i_{dr}^2 = I_r^{limit^2}$).

4.2.2.3 MIP Formulation

In this section, a MINLP problem is formulated to calculate the steady-state variables of the Type-III WTs considering the control system behavior. As the operating modes are assumed to be unknown, a binary variable u_1 is used to incorporate the main operating scenarios P1 and P2, shown in Fig. 4.5, into one optimization problem. The control system of the DFIG is operating in scenario-P1 when $u_1 = 0$, while it is operating in scenario-P2 when $u_1 = 1$.

The objective function of the optimization problem is the minimization of the absolute error of the control system equations. The constraints of the optimization problem include the steady-state circuit and power equations. The behavior of the current limiters is incorporated into the optimization problem using equality and inequality constraints. The decision variables are $(i_{ds}, i_{qs}, i_{dr}, i_{qr}, i_{dg}, i_{qg}, v_{dr}, v_{qr}, s, P, P_m, u_1)$. The inputs to the optimization problem are the stator voltage V_s and the wind speed W_{wind} .

$$\begin{aligned}
& \text{minimize} && | -v_{ds}i_{qs} - Q_s^* | + | -v_{ds}i_{qg} - Q_g^* | \\
& && + | X_m(i_{qs}i_{dr} - i_{ds}i_{qr}) - T_{em}^* | u_1 \\
& \text{subject to} && (2.7 - 2.8), (2.10) \\
& && (X_m(i_{qs}i_{dr} - i_{ds}i_{qr}) - T_{em}^*)(1 - u_1) = 0 \\
& && i_{qr}u_1 = 0 \tag{4.7} \\
& && u_1 I_r^{limit^2} \leq i_{dr}^2 \leq I_r^{limit^2} \\
& && i_{qr}^2 + i_{qr}^2 \leq I_r^{limit^2} \\
& && i_{qg}^2 + i_{qg}^2 \leq I_g^{limit^2} \\
& && -1 \leq s \leq 0
\end{aligned}$$

Please note that the main idea of using the binary variable is to divide the operating of the system into to main modes and then ensure prioritizing the T_{em}^* over Q_s^* in each region. Naturally, one may think to remove the binary variable and insert the torque equation always in the objective with a very high penalty coefficient. However, that formulation tends to be weak as the penalty coefficient value affects the solution. A very large value will affect the efficiency of the calculation, and an optimal solution may not always be obtained. A small value will not achieve the goal and will not prioritize the T_{em}^* over Q_s^* .

4.2.2.4 LVRT Considered

When the LVRT function is activated, The RSC controller prioritizes the reactive current instead of the active current and switches from the Q-control to a proportional V-control. To incorporate that effect into the original MIP formulation in the previous section, a binary variable u_2 is considered. When $V_{LVRT} < V_s$, the binary variable u_2 is equal to 0, so the LVRT function is not modeled and the optimization problem reflects the normal operation where priority in the RSC controller is given to the active current. When $V_{LVRT} > V_s$, the binary variable u_2 is equal to 1, and the LVRT function is modeled. The LVRT constraint in (4.1) is added as an equality constraint, while the torque equation is added in the objective function. That will ensure giving priority to reactive current in this operating mode. The overall optimization problem considering the LVRT function is the following.

$$\begin{aligned}
& \text{minimize} && | -v_{ds}i_{qs} - Q_s^*|(1 - u_2) + | -v_{ds}i_{qg} - Q_g^*| \\
& && + |X_m(i_{qs}i_{dr} - i_{ds}i_{qr}) - T_{em}^*|(u_1 + u_2) \\
& \text{subject to} && (2.7 - 2.8), (2.10) \\
& && (X_m(i_{qs}i_{dr} - i_{ds}i_{qr}) - T_{em}^*)(1 - u_1)(1 - u_2) = 0 \\
& && i_{qr}u_1 = 0 \\
& && u_2(K(V_{LVRT} - v_{ds}) - i_{qs}) = 0 \tag{4.8} \\
& && u_2 + u_1 \leq 1 \\
& && u_1 I_r^{limit^2} \leq i_{dr}^2 \leq I_r^{limit^2} \\
& && i_{qr}^2 + i_{qr}^2 \leq I_r^{limit^2} \\
& && i_{qg}^2 + i_{qg}^2 \leq I_g^{limit^2} \\
& && -1 \leq s \leq 0
\end{aligned}$$

4.2.3 Validation

To validate the analysis conducted in the previous section, a testbed of Type-III WT's model is simulated in MATLAB/SimPowerSystems(2020), as shown in Fig .2.13. Table 4.1 presents the detailed parameters of the EMT model.

Table 4.1: Parameters of Simulink model

R_s	0.023(p.u)	friction factor	0	X_g	0.3(p.u)
R_r	0.016(p.u)	pole pairs	3	R_g	0.003(p.u)
X_s	0.18(p.u)	Inertia	0.0685 s	C_{dc}	0.01 (F)
X_r	0.16(p.u)	S_n	1.5 (MVA)	V_{dc}	1150 V
X_m	2.9(p.u)	V_n	575 V	Q_s^*	-0.2(p.u)
I_r^{limit}	1(p.u)	I_g^{limit}	0.5(p.u)	Q_g^*	-0.4(p.u)
W_{wind}	11 m/s (1 p.u)	T_{em}^*	-0.70(p.u)	f_n	60 Hz

The calculations are conducted considering 4 different values of the stator voltages, which lead to different operating modes of the control systems. In Case-A, the stator voltage is dropped to 0.80, so the GSC controller can not track the reactive power reference. In Case-B, the stator voltage is dropped to 0.75, so the GSC and RSC controllers can not track the reactive power references. In Case-C, the stator voltage is dropped to 0.72, so the GSC controllers can not track the reactive power reference. The RSC controller can not track the electromagnetic and reactive power references at that voltage level. In Case-E, the stator voltage is dropped to 0.65, so the LVRT function is activated. The RSC controller give priority to the reactive current to follow the LVRT requirement ($i_{qr}^* = K(V_{LVRT} - v_{ds})$). As a result, the RSC controller can not track the electromagnetic torque reference.

The steady-state calculations are conducted using YALMIP. The formulated MIP problem is solved using BMIBNB (a built in solver on YALMIP). The solver implements a standard branch and bound algorithm. The solver relies on external linear, quadratic and semidefinite programming solvers for solving the lower bounding relaxation problems, and nonlinear

solvers for the upper bound computations (FILTERSD). It also uses an external linear programming solver for bound strengthening (GLPK).

The results obtain from the steady-state calculation problem are compared with the results from the EMT model as shown in Fig. 4.6-4.9. The solid line are obtained from the EMT model, and the dashed lines are obtained from the proposed method.

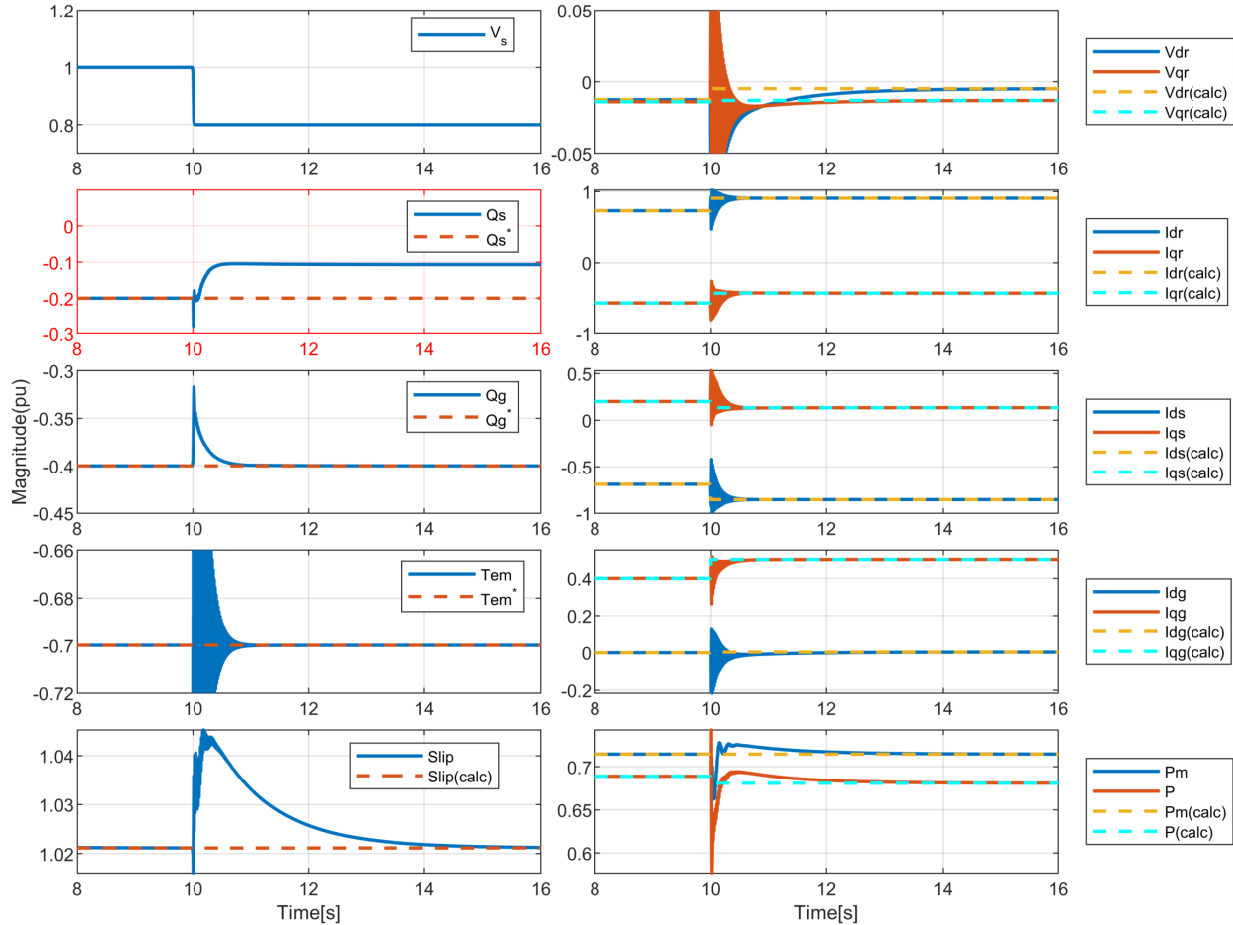


Figure 4.6: Comparison between the simulation and proposed method results at two operation points. When $t < 10$, current limits are not reached, so the control systems track the references (Mode-A). When $t > 10$, reactive current hits the limit, so the control system of the RSC can not track the reactive power reference. The RSC controller operates in Mode-B, while the GSC controller operates in Mode-A.

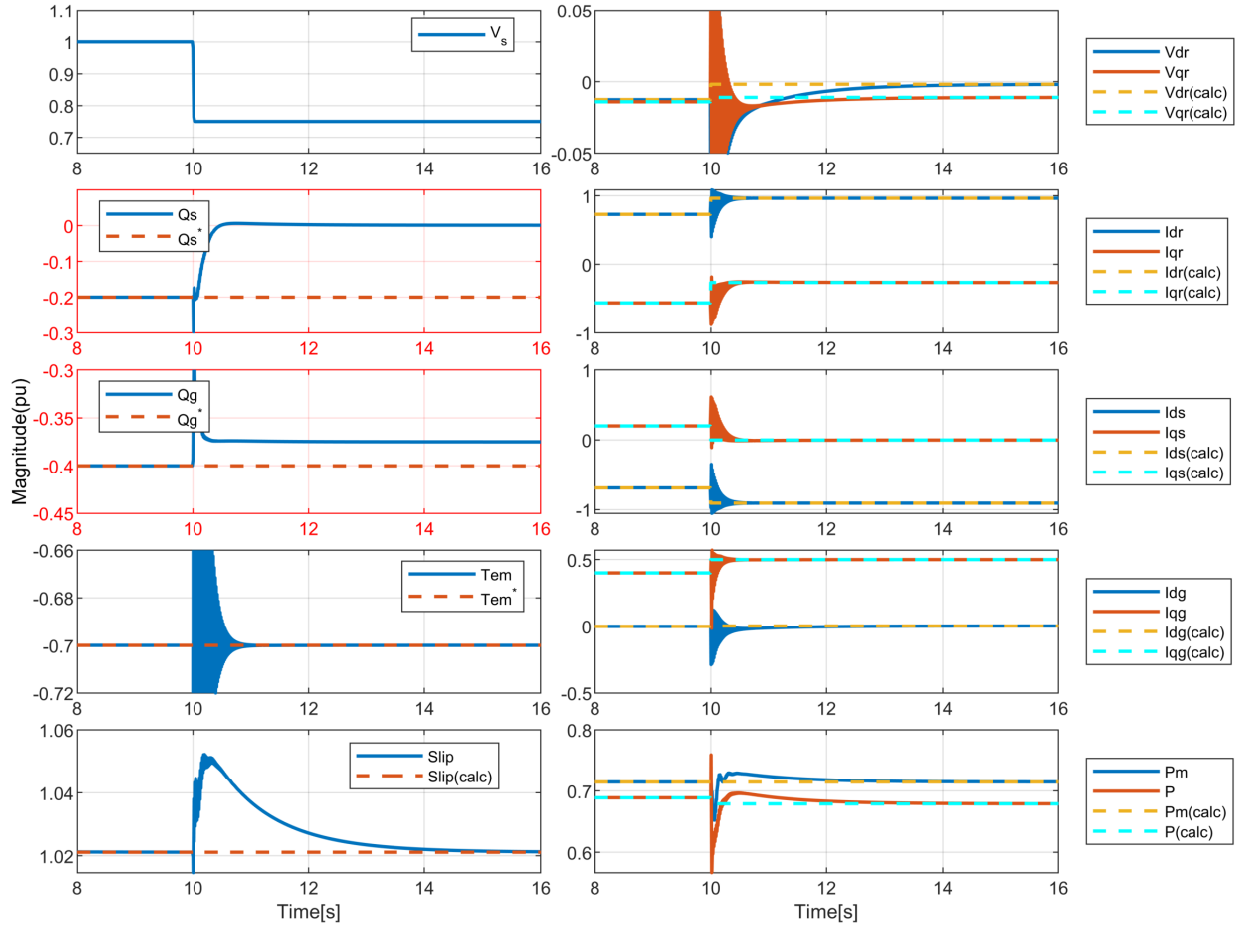


Figure 4.7: Comparison between the simulation and proposed method results. When $t > 10$, the reactive currents of the RSC and GSC hit the limit, so the control systems can not track the reactive power references. The RSC and GSC controls operate Mode-B in this region.

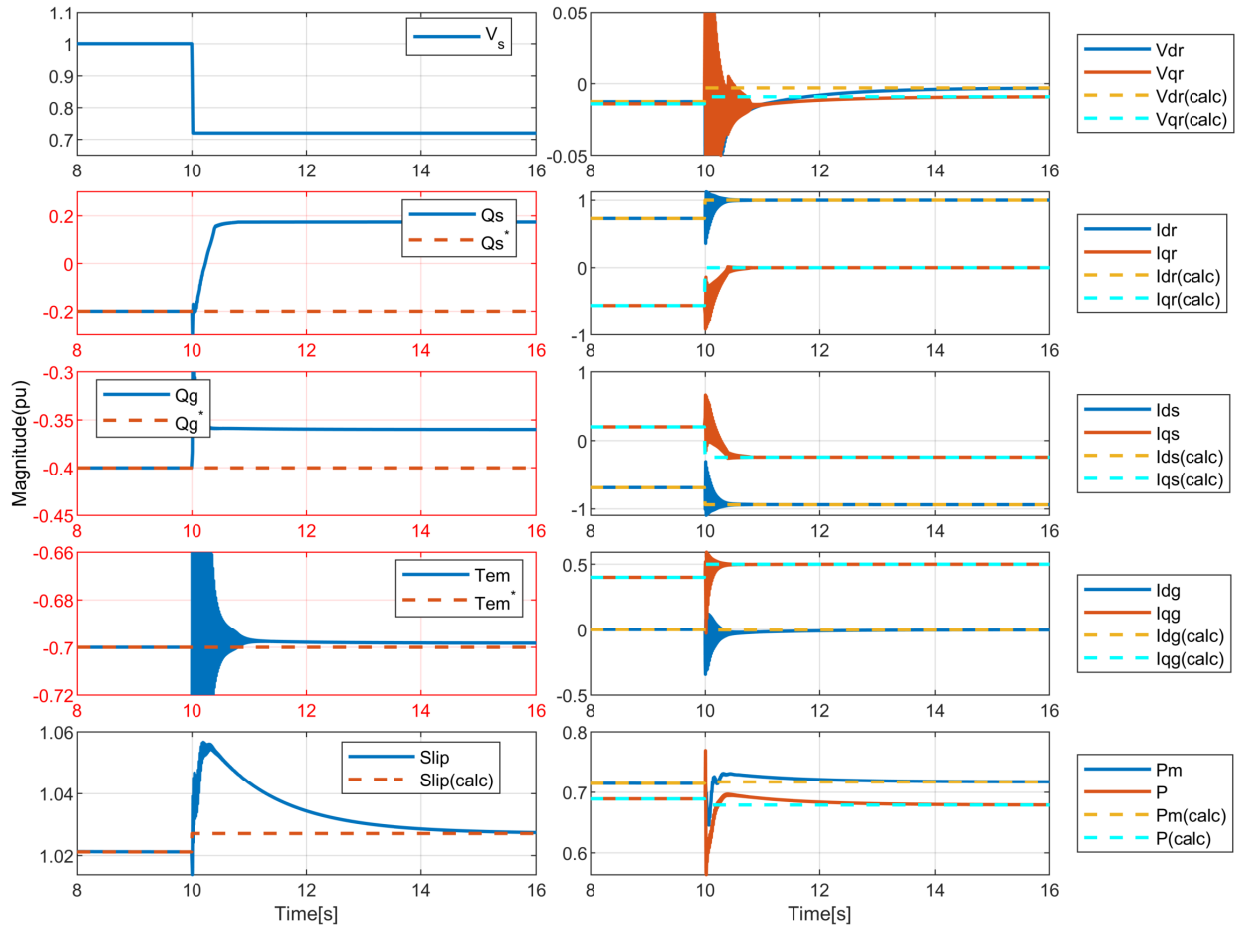


Figure 4.8: Comparison between the simulation and proposed method results. When $t > 10$, the active and reactive currents of the RSC hit the limit, so the control system can not track the electromagnetic torque and reactive power references (Mode-C). The GSC controller operates in Mode-B in this region.

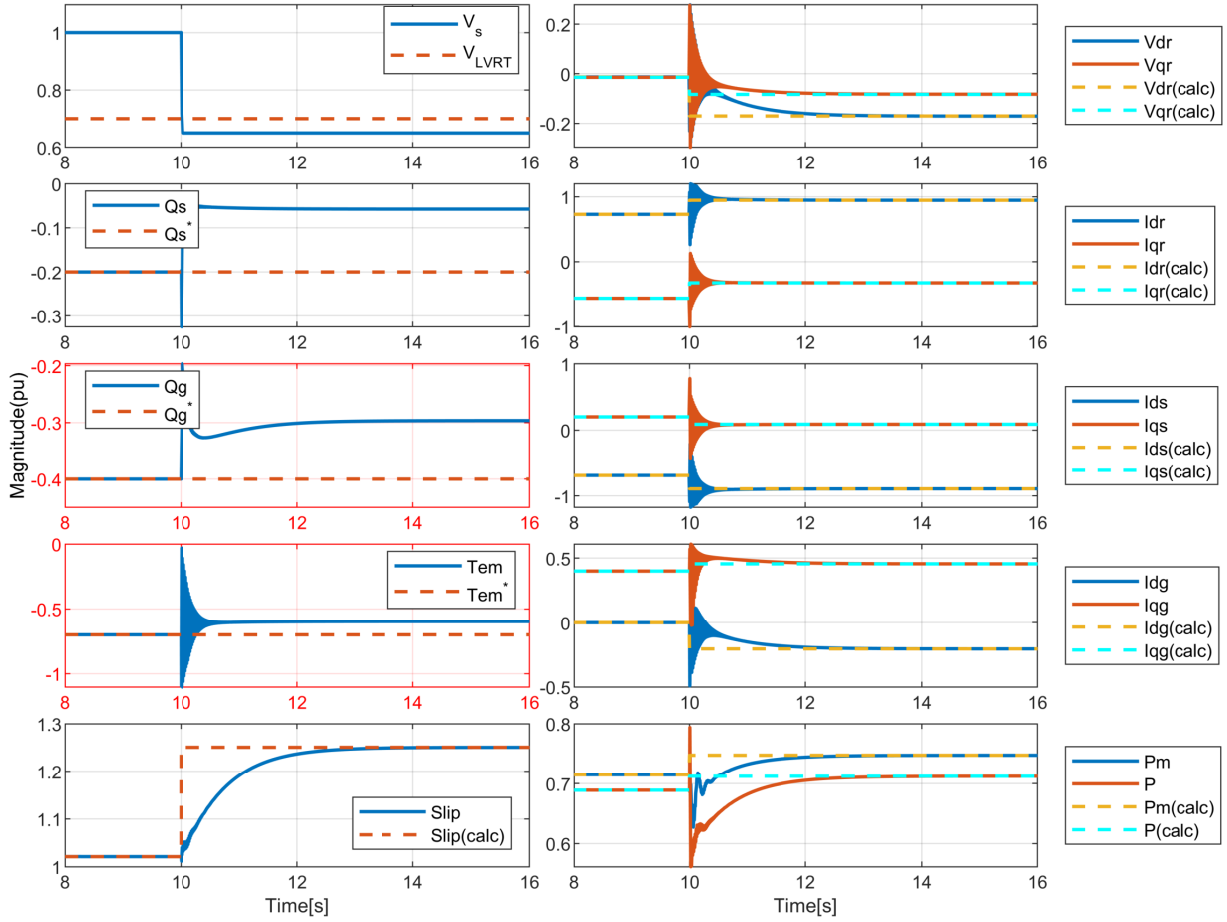


Figure 4.9: Comparison between the simulation and proposed method results. When $t > 10$, the LVRT function is activated. The RSC controller can track the LVRT linear curve ($i_{qr} = -6.5(V_{LVRT} - v_{ds})$), but it can not track the electromagnetic torque reference. The GSC controller operates in Mode-B in this region.

4.3 MIP Formulation for Fault Location Identification

4.3.1 Overview

The electric utility industry has become a competitive field in which the reliability indices are adopted to evaluate the performance of the utilities. Service interruptions caused by faults negatively affect the power quality in distribution networks. In order to reduce interruption time caused by faults in distribution feeders, utility crews should locate the fault in fast manner to ensure fast service restoration. Several strategies have been developed to locate faults or narrow the suspected area. These strategies can be categorized into: local impedance-based and wide-area monitoring-based.

The impedance-based method has been popularly used in transmission system. This method is also adopted for distribution feeders. Voltage and current measurements at the substation are used to estimate the impedance and then the distance to the fault point [68–71]. Due to the radial topology of the distribution networks, the impedance-based method may yield to multi-estimation for one fault [68].

The wide-area monitoring method relies mainly on phasor measurement units (PMUs) which have been used for several years in transmission system due to their ability to provide synchronized measurements with high precision. In wide-area monitoring methods, synchronized phasor measurements or smart meters are placed at different locations along a feeder to observe changes in voltage and current due to a fault which gives information regarding the effected area [72, 73].

Conventional PMUs have phase angle accuracy of $\pm 1^\circ$. In distribution networks, as angle differences and changes are significantly smaller than the transmission systems, micro phasor measurement units have be developed which are capable of providing more accurate measurements. Compared to the conventional PMUs, the resolution of the microPMUs has improved 100 times. The angle accuracy of microPMUs is $\pm 0.01^\circ$ [74–76].

Using microPMU for state estimation and fault location has been examined in [73] where microPMUs are assumed to be installed at every bus. This assumption is not realistic. Hence, in [77–81], sparse phasor measurements are assumed. Along with smart meter measurements, sparse phasor measurements are to estimate fault locations. In [77], the estimation is obtained by relating the calculated fault current to the measured voltage deviation by each meter. In [78], relationship of voltage deviations and fault locations are established based on given voltage/current measurements and a given impedance matrix.

In [79–81], optimization techniques were introduced for fault location identification. Compressive sensing method was employed in [79] and the K-nearest neighbors technique was employed in [80]. The capability of the both techniques is limited to locating the faulted bus only. Both techniques can neither classify the fault type nor identify the fault current magnitude.

Compared to the methods of [79, 80], the method in [81] has the capability of not only locating faulted bus, but also fault types. This method is based on an impedance matrix. A least-squares estimation problem is formulated to locate faults in distributions networks. The proposed formulation relies on linear least-squares estimator if synchronized measurements are installed in the feeder, and relies on the trust region-reflective method to solve nonlinear least-squares estimator if the measurements used are non-synchronized. The optimization problem requires multiple iterative steps to be solved until the convergence is achieved. To reduce the search space and computational burden, the proposed algorithm also utilizes existing protective devices to determine buses that are located in isolated areas.

In this thesis, mixed integer programming (MIP) is introduced to the field of fault location identification. Our method also relies on a known impedance matrix similar as the methods in [77–81]. Binary variables are introduced to indicate whether a bus is subject to fault. From there, an efficient mixed integer linear programming (MILP) formulation is formulated

to identify fault location, fault type and fault currents. This formulation is then extended for application in unbalanced distribution systems.

Compared with continuous variable based optimization, integer programming or mixed integer programming (MIP) problems are more challenging. MIP solving techniques have advanced in the past decades. Currently, large-scale MILP problems can be solved efficiently by off-shelf solvers such as Gurobi [82] or CPLEX [83]. Current computing technology offers a guarantee to find global optimum for MILP problems. Thus, the fault identification problem needs to be first modeled as a MIP problem and further into a MILP problem. From the optimization point of view, MILP problem formulation requires non-trivial techniques. In this thesis, we showcased how to introduce binary variables to model if or not a bus is subject to fault. We also convert bilinear expressions into linear expressions using big-M technique so a MIP problem becomes a MILP problem. The formulated MILP problem leads to a global optimum solution. This is the underlying reason that the algorithm can identify fault very accurately. In the case studies, we show the power of this MILP-based fault identification algorithm. Its robustness against network information error, noisy measurements, reduced number of PMUs has all been examined and the results are satisfactory.

For mixed integer programming problems, scalability is the key to feasibility. An algorithm has to be tested on large-size problems. Thus, the scalability of the proposed formulation should be tested. The algorithm is tested on two larger-scale distribution systems (IEEE 123-bus feeder and 134-node real-life feeder) with different characteristics to demonstrate its scalability. Furthermore, realistic considerations are taken into account. Effects of distributed generation penetration, reduced number of microPMUs, noise in measurement data, error in prior network information, inclusion of load information, and fault resistance on the performance of the proposed method have all been thoroughly examined.

The proposed algorithm shows high accuracy rate for many challenging scenarios. An underlying reason is that the solution from the MILP formulation is guaranteed to be a global optimum. The features and requirements of the proposed algorithm are listed as follows.

- In addition to the fault type and location, the proposed method can determine the severity of the fault current by identifying the magnitude of the fault with high accuracy.
- The algorithm can handle networks with single, double or three lines and unbalanced loading feeders.
- The proposed method requires the pre and during fault voltages at the end of the branches in addition to the impedance bus matrix. A data network is also needed to concentrate data and feed them into the MILP-based algorithm for fault identification.

4.3.2 Fault Identification in a Tree Network

Fig. 4.10 shows a simple radial feeder with one main source (the substation). Using the superposition theorem, the network can be viewed during the occurrence of a fault at Bus 4 by the sum of Circuit 1 and Circuit 2. Circuit 1 represents the pre-fault condition where the voltage phasors are the pre-fault values. The node voltage phasors in Circuit 2 can be found by $\Delta\bar{V} = \bar{V}^{\text{post}} - \bar{V}^{\text{pre}}$

The topology is the same for the two circuits. For Circuit 1, the voltage and current relationship can be expressed by $\bar{I} = Y\bar{V}$. Further, the node by the source bus will be noted by the subscript S and the rest of the buses by the subscript N .

$$\begin{bmatrix} \bar{I}_S^{\text{pre}} \\ \bar{I}_N^{\text{pre}} \end{bmatrix} = \begin{bmatrix} Y_{SS} & Y_{SN} \\ Y_{NS} & Y_{NN} \end{bmatrix} \begin{bmatrix} \bar{V}_S^{\text{pre}} \\ \bar{V}_N^{\text{pre}} \end{bmatrix} \quad (4.9)$$

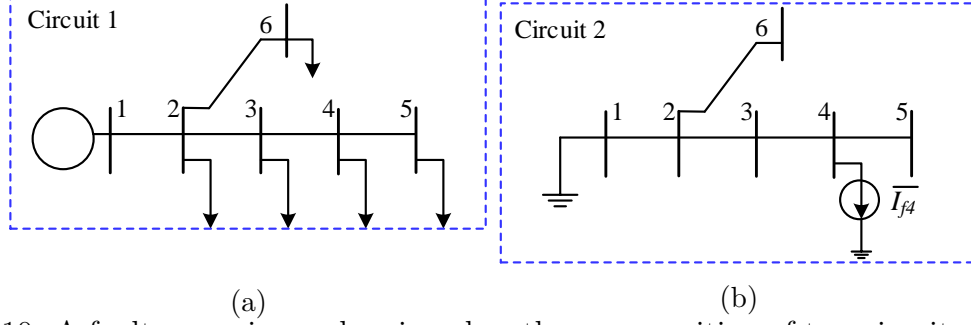


Figure 4.10: A fault scenario can be viewed as the superposition of two circuits. a) Circuit 1. b) Circuit 2.

For Circuit 2, the relationship between the node voltage phasors and current inject phasors can be written as the following:

$$\begin{bmatrix} 0 & 0 & -\bar{I}_{f4} & 0 & 0 \end{bmatrix}^T = Y_{NN} \Delta \bar{V}_N \quad (4.10)$$

The nodal voltage phasors can be expressed using the impedance matrix $Z_{NN} = Y_{NN}^{-1}$ as the following:

$$\Delta \bar{V}_N = Z_{NN} \begin{bmatrix} 0 & 0 & -\bar{I}_{f4} & 0 & 0 \end{bmatrix}^T = Z_{NN}(:, 3)(-\bar{I}_{f4}) \quad (4.11)$$

Only one voltage phasor is required to find a unique solution for \bar{I}_{f4} . The problem becomes an estimation problem (over-determined) when data is available from multiple voltage phasor measurements.

The problem now is extended further so the fault location and current are assume to be unknown. A binary variable u is designated for each node. $u_i = 1$ If there is a fault at node i , and $u_i = 0$ if there is no fault. The node voltage phasor equations in Circuit 2 can be re-written as following:

$$\Delta \bar{V}_N = Z_{NN} \begin{bmatrix} -u_2 \bar{I}_{f2} & -u_3 \bar{I}_{f3} & -u_4 \bar{I}_{f4} & -u_5 \bar{I}_{f5} & -u_6 \bar{I}_{f6} \end{bmatrix}^T \quad (4.12)$$

$u_i \bar{I}_{fi}$ is replaced by \bar{I}_{xi} so the following logic statement is imposed.

$$\bar{I}_{xi} = \begin{cases} \bar{I}_{fi}, & \text{if } u_i = 1 \\ 0, & \text{if } u_i = 0 \end{cases} \quad (4.13)$$

$u_i \bar{I}_{fi}$ is a bilinear expression which can not be solved using the current off-shelf mixed integer programming solvers such as Mosek [84]. Hence, the big-M technique is employed to overcome that issue and impose the logic statement in (4.13). A big number $M = 10^6$ is introduced. In the computing process, the complex form is used so real and imaginary parts can be considered separately. The the logic statement in (4.13) can be expressed by the following inequality constraints.

$$\begin{aligned} -(1 - u_i)M + \text{Re}(\bar{I}_{fi}) &\leq \text{Re}(\bar{I}_{xi}) \leq \text{Re}(\bar{I}_{fi}) + (1 - u_i)M \\ -(1 - u_i)M + \text{Im}(\bar{I}_{fi}) &\leq \text{Im}(\bar{I}_{xi}) \leq \text{Im}(\bar{I}_{fi}) + (1 - u_i)M \\ -u_i M &\leq \text{Re}(\bar{I}_{xi}) \leq +u_i M \\ -u_i M &\leq \text{Im}(\bar{I}_{xi}) \leq +u_i M \end{aligned} \quad (4.14)$$

If there is only one fault in system, an inequality constraint can be imposed as follows:

$$\sum_{i=2}^6 u_i \leq 1.$$

4.3.3 Minimum Placement of MicroPMUs

In this section, the minmum number of microPMUs and their placement on the feeder which allows identifying fault currents at any node in the feeder are discussed. This placement problem has been addressed in [81] by studying linear independency of columns in an impedance matrix. We will use a more tutorial approach and an example to describe the minimum placement requirement. Suppose that the fault location is known. Then any

measurement will indicate the fault current based on (4.11) and its implication. However, if the fault location is assumed to be unknown, the identification needs further consideration to obtain accurate results.

The Z_{NN} matrix characteristics is examined using the example test feeder from Fig. 4.10. If the shunt branches are neglected the and the impedance of a line connecting Node i and Node j is z_{ij} , the impedance matrix Z_{NN} (5×5) for the 6-node distribution feeder can be obtained as the following:

$$Z_{NN} = \begin{bmatrix} z_{12} & z_{12} & z_{12} & z_{12} & z_{12} \\ z_{12} & z_{12} + z_{23} & z_{12} + z_{23} & z_{12} + z_{23} & z_{12} \\ z_{12} & z_{12} + z_{23} & z_{12} + z_{23} + z_{34} & z_{12} + z_{23} + z_{34} & z_{12} \\ z_{12} & z_{12} + z_{23} & z_{12} + z_{23} + z_{34} & z_{12} + z_{23} + z_{34} + z_{45} & z_{12} \\ z_{12} & z_{12} & z_{12} & z_{12} & z_{12} + z_{26} \end{bmatrix}.$$

The first row has the same impedance z_{12} , which means that faults at Buses (2 to 6) will have the same impact from Bus 2 voltage's prospective since the voltage phasor at Bus 2 can be describe as follows:

$$\Delta \bar{V}_2 = -z_{12} \bar{I}_{fi}, \text{ for all } i \geq 2. \quad (4.15)$$

It can be seen from the second row that Bus 3's voltage phasor can only differentiate if the fault is at either Buses 2,6 or Buses 3,4,5. However, it can not distinguish between Bus 2 and Bus 6 nor Bus 3, 4 and 5. Row 4 shows that Bus 5's voltage can distinguish between faults at every location, but it can not differentiate if the fault is at Bus 2 or Bus 6. Row 5 shows that the voltage at Bus 6 can distinguish faults at the main feeder branch (Buses 2, 3, 4, 5) versus a fault located at another branch (Bus 6).

The fault location can be accurately located by placing two microPMUs at Bus 5 and Bus 6 if the fault current phasor is known. The two buses are characterized by being located at the end of each branch in the feeder. As an extension, the analysis indicates that if the fault current phasor is known, placing microPMUs at end Buses will ensure accurate fault location identification. Fault at Bus 3 and Bus 4 may result in the same value of $\Delta\bar{V}_5$ if the fault current is not fixed. To avoid that scenario, the fault current is found by installing a microPMU at Bus 2 since the fault current can be found by measuring $\Delta\bar{V}_2$ and using (4.15). The assumption is that there is only one fault in the entire distribution feeder. Otherwise, $\Delta\bar{V}_2$ will not give enough information regarding the fault current phasor.

As a summary, the minimum number of microPMUs required to accurately identify fault current and location is equal to the number of tree branches added by 1. A mixed integer problem is formulated (shown in (4.16)) and solved by MIP commercial solvers. Norm 2 is set as an objective function to minimize the error between the measurements and their estimates.

$$\text{minimize } \sum_{i \in \mathcal{E}} \|\Delta\bar{V}_i^{\text{meas}} - \Delta\bar{V}_i\| \quad (4.16a)$$

$$\text{subject to } \sum_{i \in \mathcal{N}} u_i \leq 1 \quad (4.16b)$$

$$\Delta\bar{V}_N = -Z_{NN}\bar{I}_x \quad (4.16c)$$

$$(4.14) \text{ for all } i \in \mathcal{N}$$

where \mathcal{E} is the set of the buses located at the end of each branch and the bus closest to the substation bus, \mathcal{N} is the set of the buses except the substation bus. Constraint (4.16b) indicates that the system has a maximum of one bus subjected to fault.

4.3.4 MIP Formulation for Three-Phase Systems

In this section, The MIP formulation is extended to three-phase unbalanced distribution systems. Two binary variables are introduced. The first fault location binary variable $u_{i\phi}$ is assigned to each phase ϕ at each bus i except the substation bus. The second location binary variable k is assigned to each bus except the substation bus. For instance, if the Fig. 4.10 is a single line diagram for a three-phase distribution feeder where all the line segments are three phase, the dimension of u is 15, and the dimension of k is 5. If there is only one fault in system, an inequality constraint can be imposed as follows: $\sum_{i=2}^6 k_i = 1$.

For each Bus, there are three voltage and injected current phasors related to each phase(abc). If the example feeder in Fig. 4.10 is experiencing three-phase fault at Bus 4, the relationship in (4.10) can be written as follows:

$$\begin{bmatrix} 0_{3 \times 1} \\ 0_{3 \times 1} \\ -\bar{I}_{f4}^{abc} \\ 0_{3 \times 1} \\ 0_{3 \times 1} \end{bmatrix} = Y_{NN}^{abc}{}_{15 \times 15} \underbrace{\begin{bmatrix} \Delta \bar{V}_2^{abc} \\ \Delta \bar{V}_3^{abc} \\ \Delta \bar{V}_4^{abc} \\ \Delta \bar{V}_5^{abc} \\ \Delta \bar{V}_6^{abc} \end{bmatrix}}_{\bar{V}_N^{abc}} \quad (4.17)$$

where $(.)^{abc}$ notates a column vector consisting of phase a, b, and c phasors, subscript 3×1 or 15×15 notates the dimension of a vector (matrix). Similarly, the relationship in (4.12) can be written in the three-phase format as follows:

$$\Delta \bar{V}_N^{abc} = Z_{NN}^{abc} \begin{bmatrix} -u_{2a} \bar{I}_{f2}^a & -u_{2b} \bar{I}_{f2}^b & -u_{2c} \bar{I}_{f2}^c & \dots & -u_{6a} \bar{I}_{f6}^a & -u_{6b} \bar{I}_{f6}^b & -u_{6c} \bar{I}_{f6}^c \end{bmatrix}^T \quad (4.18)$$

The mixed integer least norm 2 problem in (4.16), which is formulated considering a single phase system, is now written in three-phase format as shown in (4.19).

$$\text{minimize } \sum_{i \in \mathcal{E}} \|\Delta \bar{V}_i^{abc, \text{meas}} - \Delta \bar{V}_i^{abc}\| \quad (4.19a)$$

$$\text{subject to } \Delta \bar{V}_N^{abc} = -Z_{NN}^{abc} \bar{I}_x^{abc} \quad (4.19b)$$

$$-(1 - u_{i\phi})M + \text{Re}(\bar{I}_{fi}^\phi) \leq \text{Re}(\bar{I}_{xi}^\phi) \leq \text{Re}(\bar{I}_{fi}^\phi) + (1 - u_{i\phi})M \quad (4.19c)$$

$$-(1 - u_{i\phi})M + \text{Im}(\bar{I}_{fi}^\phi) \leq \text{Im}(\bar{I}_{xi}^\phi) \leq \text{Im}(\bar{I}_{fi}^\phi) + (1 - u_{i\phi})M \quad (4.19d)$$

$$-u_{i\phi}M \leq \text{Re}(\bar{I}_{xi}^\phi) \leq +u_{i\phi}M \quad (4.19e)$$

$$-u_{i\phi}M \leq \text{Im}(\bar{I}_{xi}^\phi) \leq +u_{i\phi}M \quad (4.19f)$$

$$u_{ia} + u_{ib} + u_{ic} = 3k_i \quad (4.19g)$$

$$\sum_{i \in \mathcal{E}} k_i = 1 \quad (4.19h)$$

for all $i \in \mathcal{N}$

where \mathcal{E} is the set of the microPMU phases, \mathcal{N} is the set of the buses except the substation bus. The impedance matrix Z_{NN}^{abc} was found by removing the first three columns and rows in the Y_{bus}^{abc} obtained from OpenDSS [85], and then inverting it. u_{ia} , u_{ib} and u_{ic} are the binary variables assigned to phase a , phase b and phase c in Bus i .

If a DG is connected to a feeder, the three-phase voltage phasors of the DG terminals should be measured. Z_{NN}^{abc} is then obtained from a modified admittance matrix. The original admittance matrix Y_{NN}^{abc} will have its rows corresponding to the buses with DGs modified. This treatment of DG has been adopted by [81].

A brief explanation is presented in the following using the 6-node feeder example. If a DG is connected at Bus 3, the equation (4.17) can be written as follows.

$$\begin{bmatrix} 0_{3 \times 1} \\ -\bar{I}_{f4}^{abc} \\ 0_{3 \times 1} \\ 0_{3 \times 1} \\ \hline \Delta \bar{V}_3^{abc} \end{bmatrix} = \begin{bmatrix} Y'_{NN}{}^{abc} \\ \hline \cdots & 0 & 1 & 0 & 0 \\ \cdots & 0 & 0 & 1 & 0 \\ \cdots & 0 & 0 & 0 & 1 \end{bmatrix} \begin{bmatrix} \Delta \bar{V}_2^{abc} \\ \Delta \bar{V}_4^{abc} \\ \Delta \bar{V}_5^{abc} \\ \Delta \bar{V}_6^{abc} \\ \Delta \bar{V}_3^{abc} \end{bmatrix} \quad (4.20)$$

where $Y'_{NN}{}^{abc}$ is obtained after deleting rows in Y_{NN}^{abc} that are relevant to Bus 3.

The constraint (4.19b) can be written as the following general form:

$$\Delta \bar{V}_N^{abc} = -Z_{NN}^{abc} \begin{bmatrix} \bar{I}_x^{abc} \\ \hline -\bar{V}_{DG}^{abc} \end{bmatrix} \quad (4.21)$$

where Z_{NN}^{abc} is the inverse of the modified admittance matrix with DG consideration.

4.3.4.1 Faulted Bus and Phase Determination

Note that the equality constraints expressed as $u_{ia} + u_{ib} + u_{ic} = 3k_i$ greatly reduces the feasible region of the MIP problem. When a fault occurs at a bus i , k_i will be set as 1. The fault can be single line to ground (e.g, phase a to ground and $(u_{ia}, u_{ib}, u_{ic}) = (1, 0, 0)$), or two phase to ground (e.g., $(u_{ia}, u_{ib}, u_{ic}) = (1, 1, 0)$), or three phase to ground ($(u_{ia}, u_{ib}, u_{ic}) = (1, 1, 1)$). Hence, naturally we want to have the inequality constraints: $u_{ia} + u_{ib} + u_{ic} \geq k_i$. For every bus with three phases, there are $\binom{3}{1} + \binom{3}{2} + \binom{3}{3} = 7$ combinations of fault types to be examined. For a 123-bus feeder, we need to examine $122 \times 7 = 854$ possibilities of fault locations.

On the other hand, the equality constraint $u_{ia} + u_{ib} + u_{ic} = 3(k_i)$ indicates that when there is no fault at Bus i , $u_{ia} = u_{ib} = u_{ic} = 0$ and when there is a fault at Bus i , $u_{ia} = u_{ib} = u_{ic} = 1$. This constraint is equivalent to $u_{ia} = u_{ib} = u_{ic} = k_i$. Hence the entire MIP problem can be viewed to have just $N - 1$ binary variables with all fault types assumed as three-phase to ground faults. For a 123-bus feeder, we only need to examine 122 possibilities of fault locations. This formulation leads to efficient computation.

We will then rely on identified fault current magnitude at each phase to determine fault types. The faulted phase (or phases) is distinguished by its high magnitude compared to the negligible magnitudes of the unfaulted phases. To distinguish between double-phase to ground and phase to phase faults in grounded systems, the angles of the fault currents can be used. An angle difference of around 180° is an indication for a phase to phase fault.

4.3.5 Numerical Examples

To evaluate the performance of the proposed method on 3-phase systems with different characteristics, the IEEE 37-bus feeder, IEEE 123-bus feeder, and the 134-node real-life feeder are considered. Load flow computing and faults simulating are done using OpenDSS. After load flow computation, the voltage phasor of the pre-fault and during-fault conditions are recorded from microPMUs located at the measurement buses. The admittance matrix is obtained for the feeder topology prior the fault and not changing during the fault. The data collected from OpenDSS is fed to MATLAB and solved by Mosek or Gurobi in CVX interface [86]. Alternatively, BNB solver in YALMIP [54] interface is used, which uses CPLEX as a lower solver and Rounder as an upper solver.

The tests were conducting using Mosek and the default setting of the CVX precision. The optimal solutions were successfully found in most cases. For the few cases where Mosek could not find the optimal solution using the default setting of CVX precision, optimal solutions were found by either changing the CVX precision or using Gurobi or BNB. During the tests,

to its small magnitude [88], the proposed method was successful in identifying all the faulted phases and the magnitude of the faults with high accuracy. Samples of the identification results are presented in Table 4.2. The identified fault current (in Ampere) is compared with the actual fault currents from OpenDSS.

Table 4.2: Phase-to-ground faults ($\Delta - \Delta$)

Location	Identification Results			OpenDSS Measurements	
	Obj	$I_F(\text{A})$	$\angle \bar{I}_F$	$I_{\text{flow}}(\text{A})$	$\angle \bar{I}_{\text{flow}}$
729. <i>b</i>	0.070	2.111	-36	2.225	-33.5
711. <i>c</i>	0.170	2.064	-158.9	2.188	-156.1
702. <i>b</i>	0.053	2.124	-36	2.240	-33.5
775. <i>a</i>	0.002	$4.9e10^{-4}$	-97.5	$5.3e10^{-4}$	-94.2

One at a time, double-phase to ground (between phase *a* and *b*) and three-phase faults were applied at each bus in the feeder (a total of 72 tests for each fault resistance 0 Ω , 5 Ω and 10 Ω). The proposed method was successful in identifying all the faulted phases except a double-phase to ground and three-phase faults at Bus 707. The identified Bus was 722, which is adjacent bus to Bus 707. The error distance is 37 meter. By excluding Bus 722 from the searching space, the proposed method correctly identified the faulted bus. Table 4.3 presents the identification results for double-phase to ground and three-phase faults, respectively.

Table 4.3: Double and three-phase faults ($\Delta - \Delta$)

Location	Identification Results				OpenDSS Measurements		
	Obj	$I_F^a(\text{A})$	$I_F^b(\text{A})$	$I_F^c(\text{A})$	$I_{\text{flow}}^a(\text{A})$	$I_{\text{flow}}^b(\text{A})$	$I_{\text{flow}}^c(\text{A})$
736. <i>ab</i>	155.1	1147.7	1168.5	-	1263.8	1262.9	-
714. <i>ab</i>	165.8	1992.8	2027.1	-	2191.5	2191	-
775. <i>ab</i>	39.07	10630.7	10869.4	-	11796	11796	-
727. <i>abc</i>	131.69	2231.8	2377.5	2242	2500.8	2573.9	2434.4
708. <i>abc</i>	140.2	1998.6	2159.2	2027.1	2242.2	2337.3	2197.2
720. <i>abc</i>	257	2030.3	2188.6	2070.9	2261.3	2366.7	2253.6

In order to test the performance of the proposed technique with different transformer configurations, the connection of the substation transformer was changed from Δ - Δ to Δ -Y with solidly grounded neutral. All the three types of faults were tested and the success rate was 100% in identifying single-phase faults and 97% for the other types of faults (only faults at Bus 707 were identified as faults at Bus 722).

If the load data is assumed to be available and included into the bus impedance matrix, the success rate is 100% for all the three types of faults. The load data can be collected through load meters or using the load curve.

Table 4.4 presents some of the identification results for the three types of faults with different fault resistances in Δ -Y configuration. In Case-A, the load information is not included while in Case-B, this information is included in the impedance matrix. It can be seen that with load information included, the fault current magnitudes matches better with the measurements.

4.3.5.2 The IEEE 123-Bus System

To study the performance of the proposed algorithm on networks composed of three, double and single overhead and underground lines, the IEEE 123-bus system is considered. The feeder contains four capacitor banks and a load transformer. The load is unbalanced with a combination of three types of load: constant power, constant current and constant impedance [87]. The substation voltage regulator is omitted and the three voltage regulators along the feeder are assumed as locked so that the taps are fixed.

Since the lines and the cables are not all 3 phase, each phase is evaluated separately. As a result, a microPMU is installed at the end of each branch of each phase except 27.c, 95.a and 95.c. Initial results show that in many cases faults on these ends can be detected by the microPMUs installed at 33.a and 96.b due to the mutual coupling between the phases.

Table 4.4: Identification results for the IEEE 37-bus feeder ($\Delta - Y$)

Locations	Identification Results														OpenDSS Measurements							
	Case-A								Case-B						$R_f = 0(\Omega)$			$R_f = 10(\Omega)$				
	$R_f = 0(\Omega)$				$R_f = 10(\Omega)$				$R_f = 0(\Omega)$			$R_f = 10(\Omega)$			$R_f = 0(\Omega)$			$R_f = 10(\Omega)$				
	Obj	$I_P^a(A)$	$I_P^b(A)$	$I_P^c(A)$	Obj	$I_P^a(A)$	$I_P^b(A)$	$I_P^c(A)$	Obj	$I_P^a(A)$	$I_P^b(A)$	$I_P^c(A)$	Obj	$I_P^a(A)$	$I_P^b(A)$	$I_P^c(A)$	$I_{flow}^a(A)$	$I_{flow}^b(A)$	$I_{flow}^c(A)$	$I_{flow}^a(A)$	$I_{flow}^b(A)$	$I_{flow}^c(A)$
702.a	89.6	2636.2	-	-	7.6	223.3	-	-	11.6	2807.8	-	-	1	237.9	-	-	2832.9	-	-	239.9	-	-
741.c	100.2	-	-	1210	16.7	-	-	208.8	13.4	-	-	1276.1	2	-	-	217.1	-	-	1285.4	-	-	218.9
707.b	94.2	-	1513	-	13.2	-	216.8	-	9.6	-	1582.9	-	1	-	226.8	-	-	1591.9	-	-	228	-
735.ab	140.6	1581.4	1446.2	-	18.2	202.8	211	-	15.8	1689.7	1569.1	-	1.8	214.7	227.4	-	1706.4	1583.4	-	216.7	229.6	-
704.ab	172.7	2407.3	2172	-	15.9	221	224	-	17.5	2554.1	2358.5	-	1.6	233.2	242	-	2576.5	2375.5	-	235	244.1	-
728.ab	119	2150.6	1934.4	-	12.1	216	220.2	-	12.7	2288.6	2103.6	-	1.2	228.6	238	-	2309.4	2120.3	-	230.5	240.3	-
725.abc	265	1757.7	1904.1	1807.7	30.7	206.1	219.4	215.4	30.9	1929.5	2042	1947.9	3.1	226.4	235.2	232.3	1956.6	2059.5	1966.6	229.4	237.3	234.9
744.abc	152.7	2142.3	2282.5	2152.9	15.3	207.7	224.3	220.8	14.3	2373.1	2455	2319	1.6	230.3	241.1	238	2399.9	2472.2	2336.3	233.7	243.2	240.6
732.abc	153.2	1864.8	2015.8	1899.3	16.9	202.5	220.2	216.9	16.8	2066.4	2165.7	2041.8	1.7	224.7	236.5	233.4	2092.1	2182.2	2058.3	228.1	238.6	235.9

The single PMU placement algorithm in Section 5.3 could be extended in future work to consider the mutual coupling between the phases, so that the number of microPMUs could be reduced. Fig. 4.12 shows the modified version of the IEEE 123-bus test feeder and the microPMU locations. The microPMU placement is based on the initial status of the feeder switches.

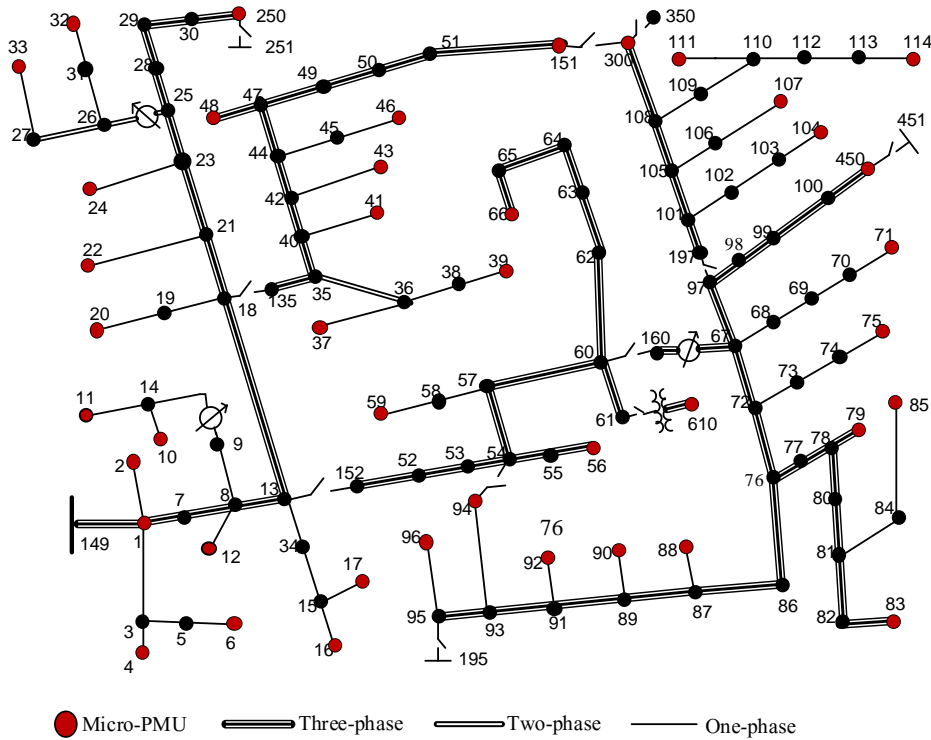


Figure 4.12: Modified version of the IEEE 123-bus test feeder.

To fully test the proposed method against the most common fault types, a single phase fault was applied at each phase in each bus in the feeder, one at a time (a total of 259). Moreover, double-phase to ground faults (phase a and b) (69 faults) and three phase to ground faults (66 faults) were applied. The three types of faults are simulated with 0Ω , 5Ω and 10Ω fault resistances.

In order to test the performance of the proposed algorithm with/without the availability of load data, three scenarios are evaluated. The first one (Case-A) makes no use of the load

data, which means less input requirements. In the second scenario (Case-B), the linear part of the loads is included into the impedance matrix. In Case-C, the load is assumed to be constant impedance and included into the bus impedance matrix.

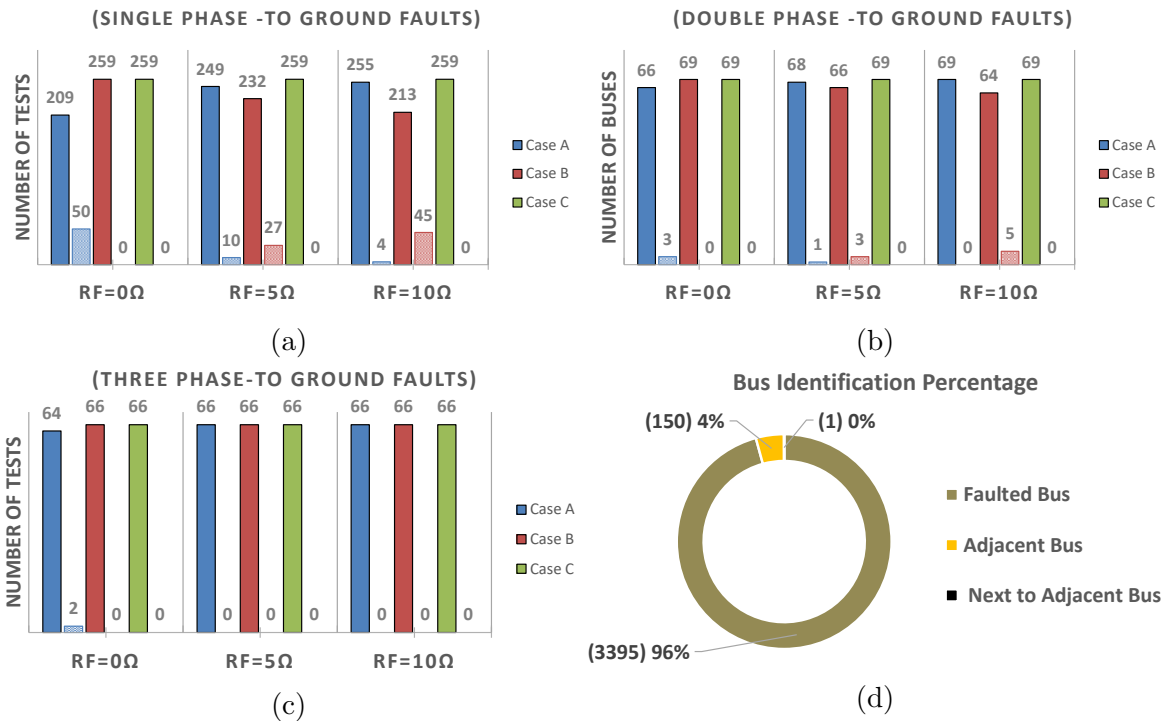


Figure 4.13: Simulation results of the fault-location algorithm. a) LG faults. b) LLG faults. c) 3LG faults. d) Identification percentage.

The histograms in Fig. 4.13 present the results of the proposed method for the three cases. The solid columns are used when a faulted bus is identified correctly while the pale columns are for the instances when the proposed method identifies an adjacent bus as a faulted bus. Table 4.5 presents the identification results for selected instances. The results show that the best performance of the proposed algorithm is for Case-C. All the faults with different fault resistances were identified correctly and the fault current magnitudes were identified with high accuracy. In Case-B, 100% success rate was achieved with bolted faults. The performance of Case-A increases as fault currents get smaller. Fig. 4.13 shows the total identification percentages for the three scenarios. More than 96% of the faulted buses

were correctly pinpointed. The fault types were 100% identified for the three scenarios. It can be seen that including the load in the admittance matrix will not always improve the performance of the algorithm unless the load is constant impedance as the performance of Case-A is better than Case-B when $R_f = 10 \Omega$.

4.3.5.2.1 Less Number of MicroPMUs

Since it is not an economic practice to install many microPMUs along distribution feeders, the number of microPMUs was reduced as shown in Fig. 4.14. All the microPMUs installed at the end of the short single phase branches were removed. Fig. 4.15 shows the results for Case-A and Case-C with reduced number of microPMUs. By comparing the results in Fig. 4 and Fig. 6, it can be seen that the performance of the algorithm did not degrade significantly in terms of the faulted bus identification. Regarding the accuracy of the estimated fault current, the performance of the method is satisfactory. For example, a fault at Bus 10 with a magnitude of 223.8 A was identified as a fault at bus 14, which is an adjacent bus, with a magnitude of 217.9 A using the reduced number of the microPMUs while it was identified correctly with a magnitude of 218.8 A when using the original microPMUs placement.

4.3.5.2.2 Noisy MicroPMUs

In this section, the sensitivity of the proposed method against inaccuracy in voltage measurements is evaluated. The magnitudes of the measured pre and during-fault voltages are multiplied by $(1 + n)$, where n is a random values generated by normal distribution with standard deviation equals to 0.5% and zero mean. The simulation results with noisy input data are shown in Fig. 4.16 and Table 4.6. It can be seen that the percentage of the noise added has almost no effect on the proposed method when the fault current is very high ($R_f = 0 \Omega$).

Table 4.5: Identification results for the IEEE 123-bus test feeder

Location	$R_f(\Omega)$	Identification Results															OpenDSS Measurements					
		CaseA					CaseB					CaseC					CaseA/B			CaseC		
		$I_F^a(A)$	$I_F^b(A)$	$I_F^c(A)$	Bus	Dist.(m)	$I_F^a(A)$	$I_F^b(A)$	$I_F^c(A)$	Bus	Dist.(m)	$I_F^a(A)$	$I_F^b(A)$	$I_F^c(A)$	Bus	Dist.(m)	$I_{flow}^a(A)$	$I_{flow}^b(A)$	$I_{flow}^c(A)$	$I_{flow}^a(A)$	$I_{flow}^b(A)$	$I_{flow}^c(A)$
56.b	0	-	4236	-	56.b	0	-	4514	-	56.b	0	-	4540	-	56.b	0	-	4523.5	-	-	4538.6	-
80.ab	0	2894	3117	-	81.ab	144.7	3143	3275	-	80.ab	0	3159	3278	-	80.ab	0	3152.5	3278	-	3158.6	3277.3	-
108.abc	0	3488	3889	3872	108.abc	0	3730	4066	4072	108.abc	0	3742	4071	4080	108.abc	0	3739.8	4069.7	4078.2	3742	4070.8	4079.7
111.a	5	367.9	-	-	111.a	0	411.3	-	-	111.a	0	397.1	-	-	111.a	0	394.5	-	-	397	-	-
36.ab	5	397.4	458.9	-	36.ab	0	434.9	474.9	-	36.ab	0	419.8	465.7	-	36.ab	0	417.7	465.5	-	419.7	465.5	-
63.abc	5	412	439.3	428.6	63.abc	0	442	461.7	451.5	63.abc	0	426.5	445.1	439.8	63.abc	0	423.9	443.5	438.2	426.4	445	439.7
78.c	10	-	-	219.7	78.c	0	-	-	238.9	77.c	30.4	-	-	226.8	78.c	0	-	-	225.7	-	-	226.8
27.ac	10	223.3	-	213.9	27.ac	0	234.2	-	228.1	27.ac	0	227.9	-	219.7	27.ac	0	227.1	-	219	227.8	-	219.7
7.abc	10	232.5	234	230	7.abc	0	248.7	244	241.4	7.abc	0	233.9	238.9	236.1	7.abc	0	233.4	238.3	235.7	233.7	238.2	235.9

Table 4.6: Identification results with noise considered for the IEEE 123-bus test feeder

Location	$R_f(\Omega)$	Identification Results												OpenDSS Measurements					
		CaseA						CaseC						CaseA			CaseC		
		Obj	$I_F^a(A)$	$I_F^b(A)$	$I_F^c(A)$	Bus	Dist.(m)	Obj	$I_F^a(A)$	$I_F^b(A)$	$I_F^c(A)$	Bus	Dist.(m)	$I_{flow}^a(A)$	$I_{flow}^b(A)$	$I_{flow}^c(A)$	$I_{flow}^a(A)$	$I_{flow}^b(A)$	$I_{flow}^c(A)$
56.b	0	221.2	-	4233	-	56.b	0	119	-	4532	-	56.b	0	-	4523.5	-	-	4538.6	-
80.ab	0	170.5	2897	3123	-	81.ab	144.7	105	3158	3275	-	80.ab	0	3152.5	3278	-	3158.6	3277.3	-
108.abc	0	156.1	3484	3891	3876	108.abc	0	107.1	3741	4074	4072	108.abc	0	3739.8	4069.7	4078.2	3742	4070.8	4079.7
111.a	5	122	368.1	-	-	111.a	0	150.1	399.5	-	-	111.a	0	394.5	-	-	397	-	-
36.ab	5	143.1	390.1	455.6	-	36.ab	0	145	428.1	461.5	-	36.ab	0	417.7	465.5	-	419.7	465.5	-
63.abc	5	111.4	421.1	436.8	431.3	62.abc	53.3	125.1	423.6	451.2	437.6	62.abc	53.3	423.9	443.5	438.2	426.4	445	439.7

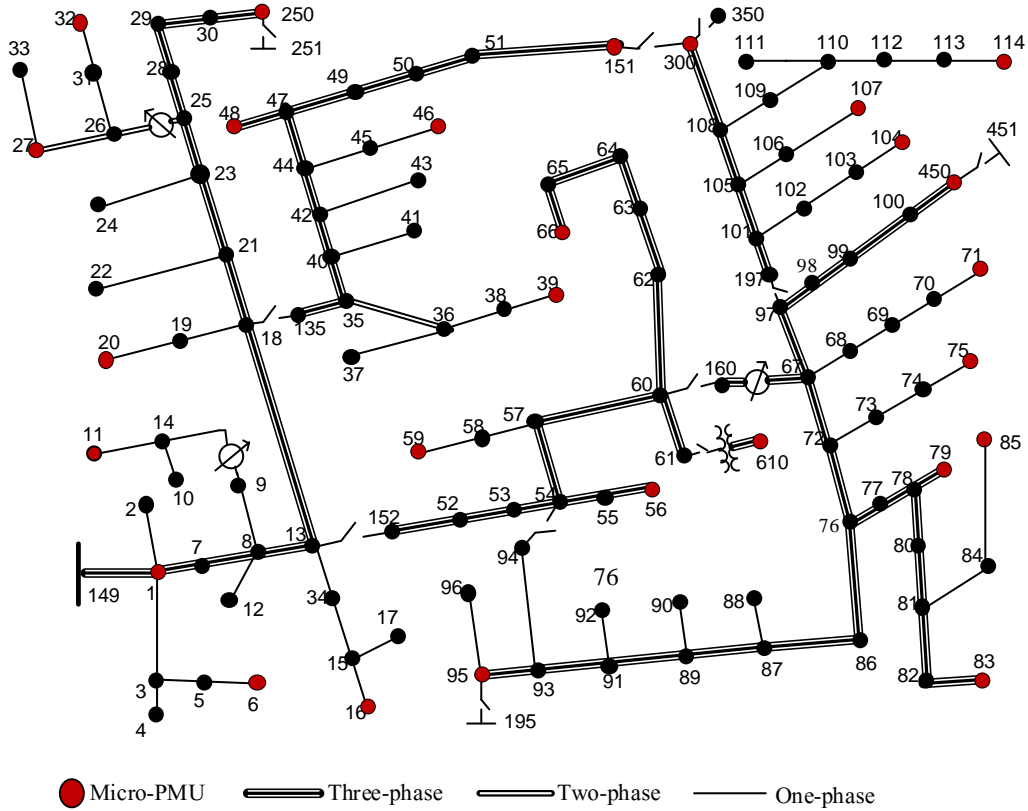


Figure 4.14: MicroPMUs placement with reduced number.

The performance of the proposed method with noisy data decreases as the fault current gets smaller. For instance, the magnitude and the fault type of double-phase (when $R_f = 5 \Omega$) and single phase faults on Bus 610 are not identified correctly (around 45 A and 1 mA, respectively) even though the proposed method was successful in identifying the faulted buses. The overall performance of the method is satisfactory since 90% of the faults were located correctly as shown in Fig. 4.16. In ungrounded systems, detecting single-phase faults may be difficult with noisy measurements.

4.3.5.3 134-Node Real-Life Feeder

The proposed method is tested on 13.8-kV, 134-bus real distribution feeder that has been commonly adopted in fault location literature [77–81, 89]. The feeder was firstly used in [89]

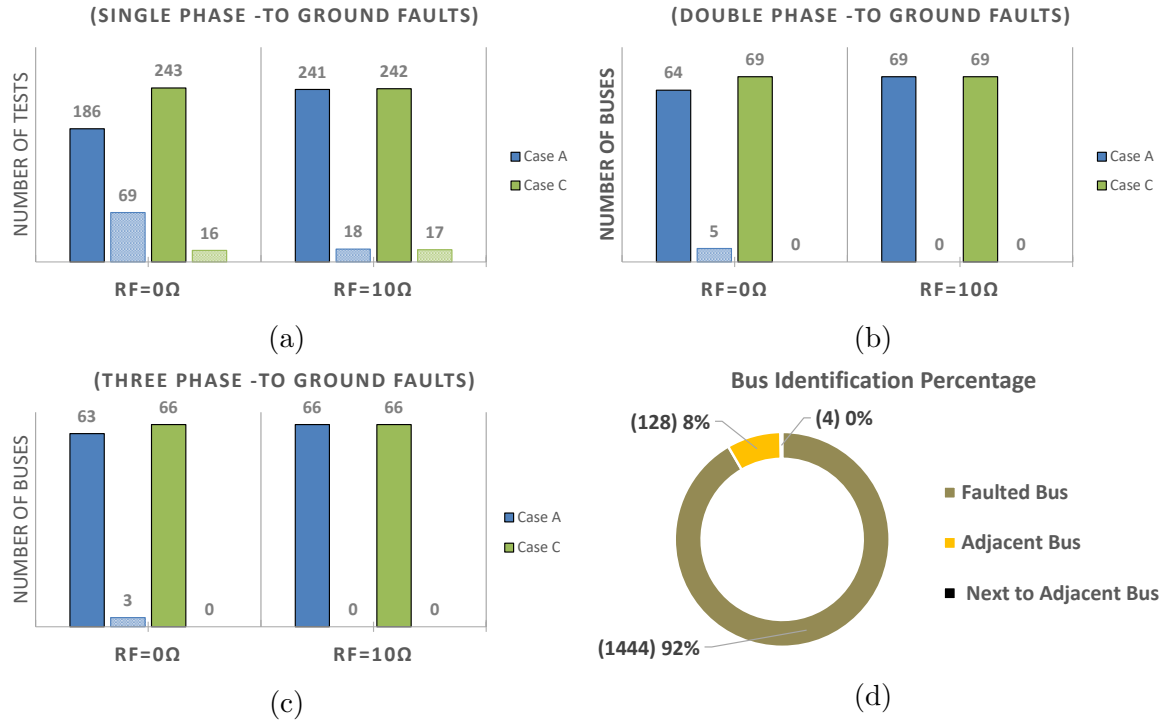


Figure 4.15: Simulation results by the reduced number of microPMUs. a) LG faults. b) LLG faults. c) 3LG faults. d) Identification percentage.

and detailed information about the feeder can be found in [77]. Only 19 microPMUs are used as shown in Fig. 4.17. Short branches are not monitored to minimize the number of the microPMUs. The simulation results are shown in Fig. 4.18 where the error is the distance from the estimated faulted bus to the actual faulted bus in meters. In Case-A, the load data are not used. The load data are assumed to be available and included into the impedance matrix in Case-B. The performance of Case-B is better than Case-A since most of the faults were identified with zero error distance and high magnitude accuracy. However, the performance of Case-A is satisfactory considering the input data requirements and since most of the faults were located within 50m error distance. Regarding the faults types, all the faults types were identified correctly in both cases. The operation of the protective devices along the feeder was not used during the tests to create the most challenging scenario, so all the 133 buses were included in the searching space.

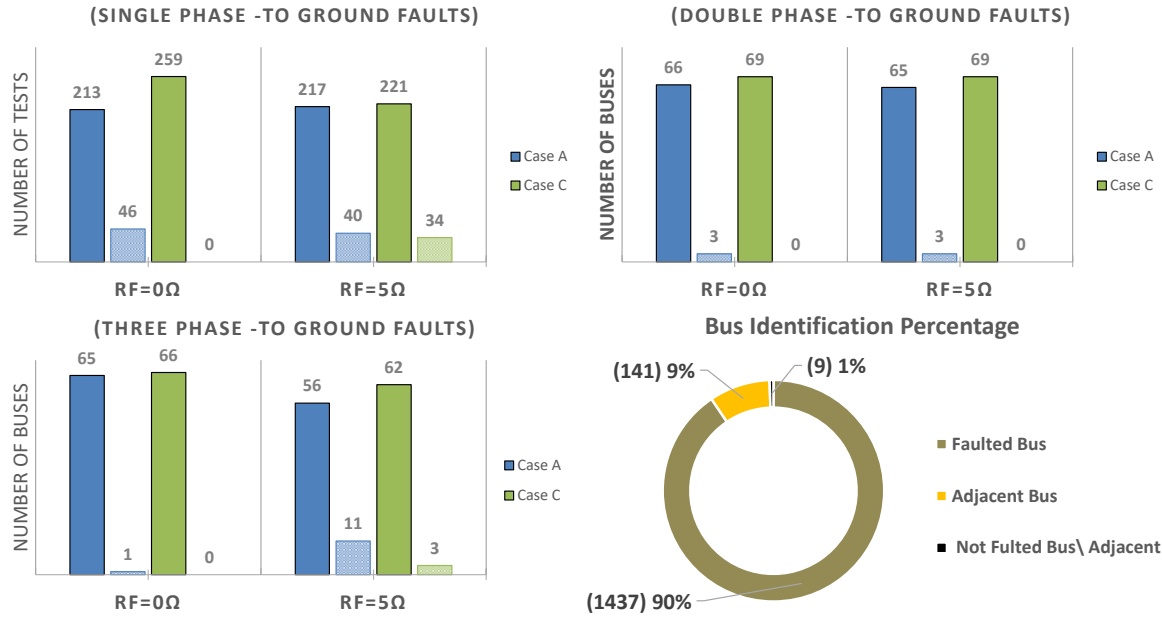


Figure 4.16: Simulation results with noise. a) LG faults. b) LLG faults. c) 3LG faults. d) Identification percentage.

4.3.5.3.1 DG Penetration

In order to evaluate the DGs impact on the proposed fault location method, two 800 kW PVs are placed at buses 90 and 134 through 13.8 kV/0.48 kV transformers. Two additional microPMUs are placed on the PVs buses. Fig. 4.19 shows the identification results for Case-A and Case-B with 0.5 Ω, 10 Ω and 100 Ω fault resistances. The results indicate that the performance of the proposed method is satisfactory when DG penetration is considered.

4.3.5.3.2 Errors in Line Impedance

In this section, sensitivity of the proposed method against inaccuracy in line impedance is evaluated. Random normal distributed noise with zero mean and standard deviation of 1% and 10% are generated. The impedance matrix of each line type is multiplied by a value from the generated noise vector. Fig. 4.20 shows the performance of the proposed algorithm

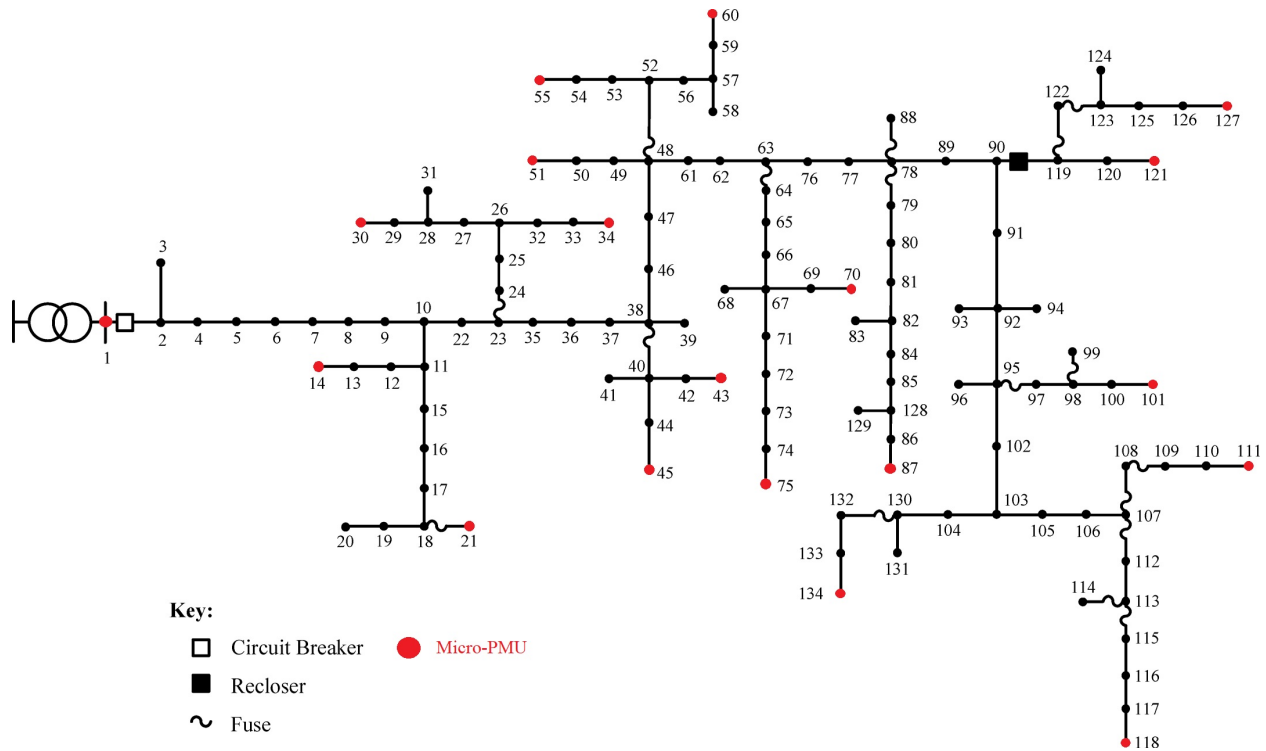


Figure 4.17: Single-line diagram of the 134-node feeder [89].

with 1% and 10% error in line impedances for the two cases. It can be seen that the proposed algorithm is robust against inaccuracy in line impedances.

4.3.5.3.3 MicroPMUs Synchronization Errors

In order to study the effect of microPMUs synchronization errors, random numbers with zero mean and standard deviations of 0.1% and 0.5% are generated and added to the angles of the measurements in radians (0.05 and 0.28 in degrees). Fig. 4.21 shows the performance of the proposed algorithm with 0.1% and 0.5% synchronization errors for the two cases. The overall performance of the method is satisfactory. It can be seen that the percentage of the noise added has small impact on the proposed method when the fault current is high ($R_f = 0.5 \Omega$). The performance of the proposed method decreases as the fault current gets smaller.

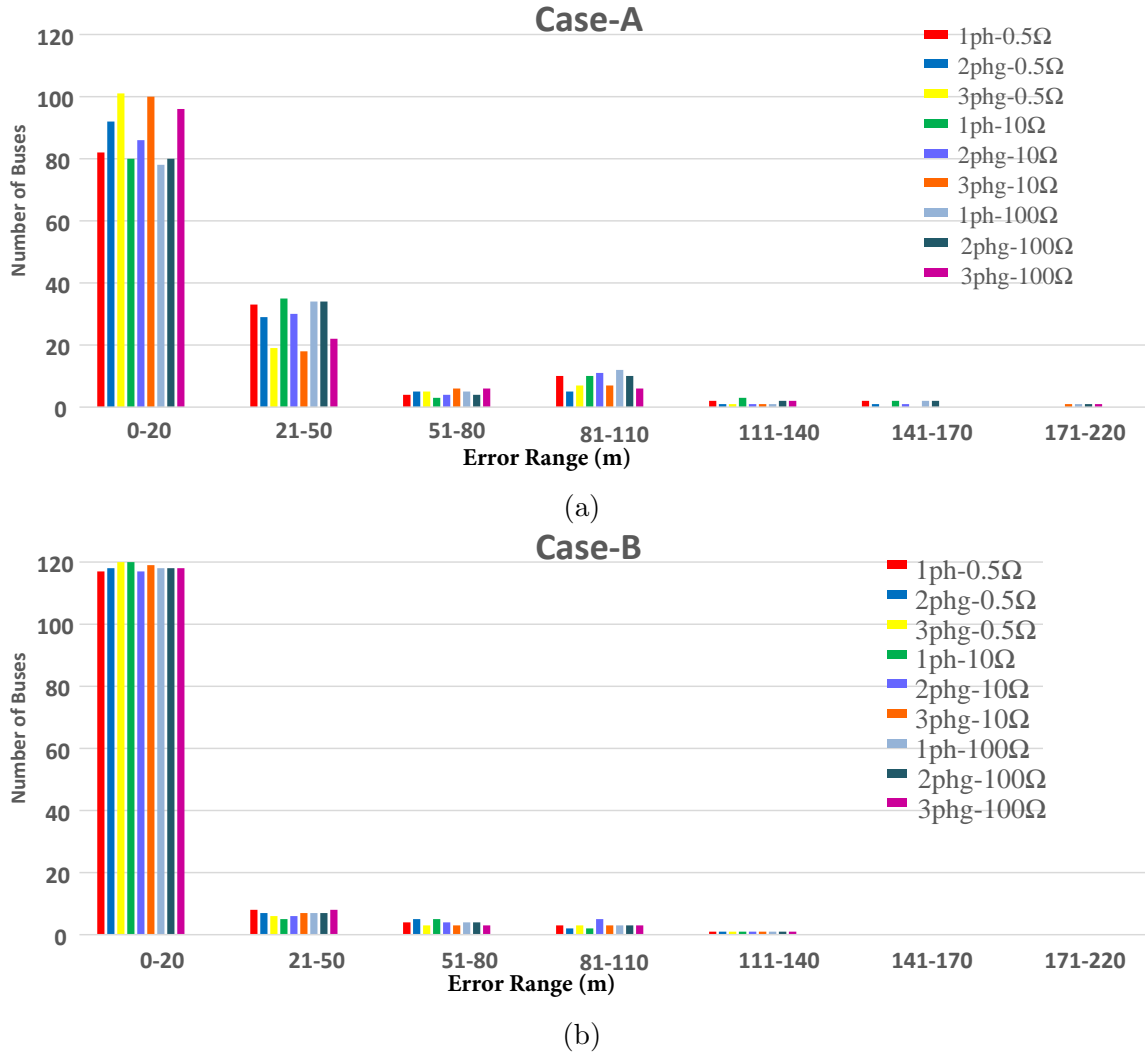


Figure 4.18: Simulation results of the fault identification algorithm. a) Case-A. b) Case-B.

4.3.6 Discussion and Comparison

Comparative studies have been conducted to compare the proposed method with other methods in the literature. The method in [77] requires load data to be included into the impedance matrix, which means a high number of load meters are required in addition to the voltage measurements. If the loads are not included in the bus impedance matrix, it will yield multiple identification answers. In contrast, our approach is applicable with or without the availability of the load data. Our MILP-based approach outperforms the

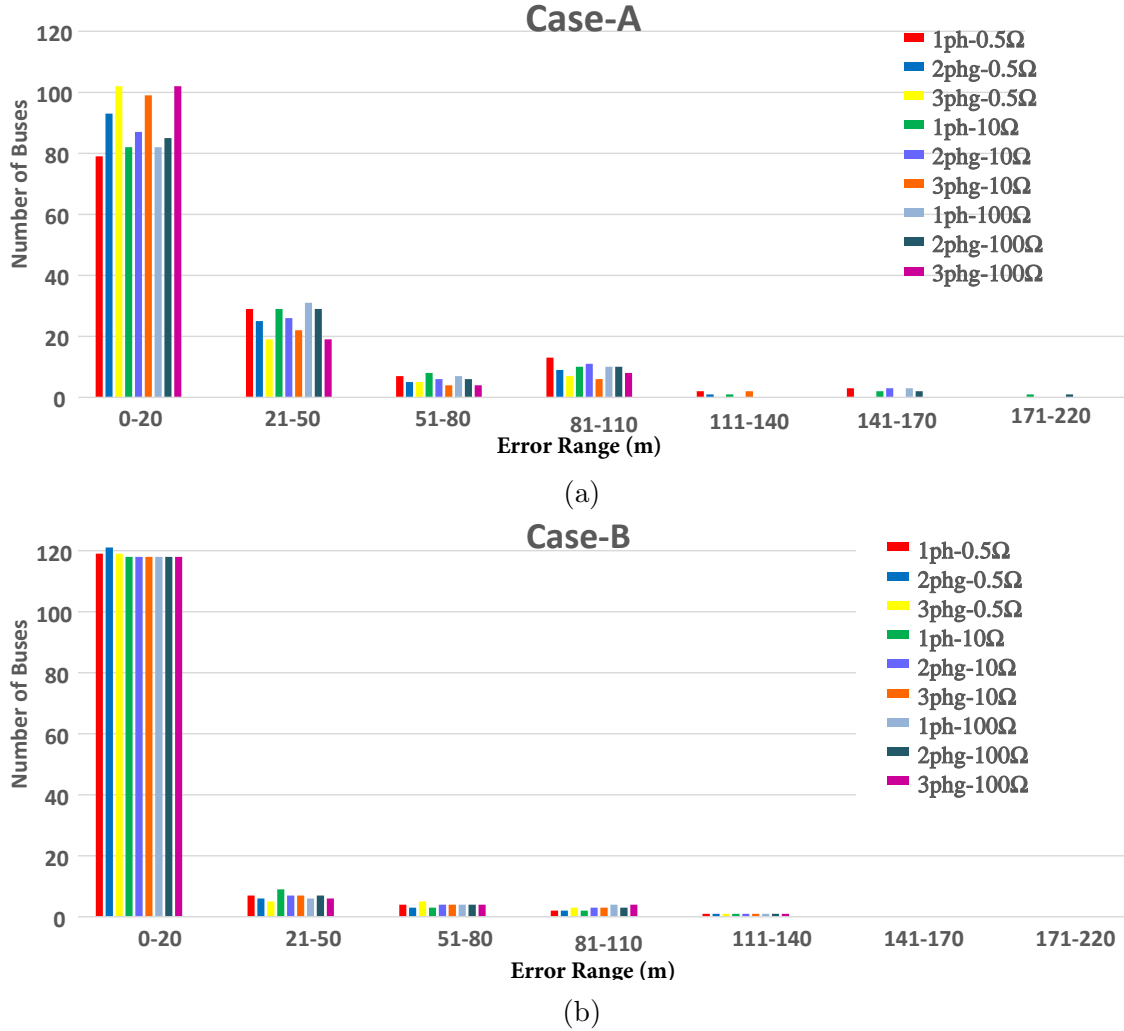


Figure 4.19: Simulation results with DGs. a) Case-A. b) Case-B.

methods in [79,80] since it can determine the fault type and the current drained by the fault with high accuracy. Table 4.7 represents a direct comparison between the performance of the method in this paper, in [77], and in [79]. It can be seen that the MIP-based method in this paper outperforms the other two methods.

For the 134-node feeder, the approach in [78] utilizes voltage and current measurements located at 13 buses, which means 78 measured values (each meter provides the three-phase voltages and currents). In our approach, for the same scenario, less error rate is achieved with less measurements. 57 (3×19) values are used in our approach. Fig. 4.22 shows

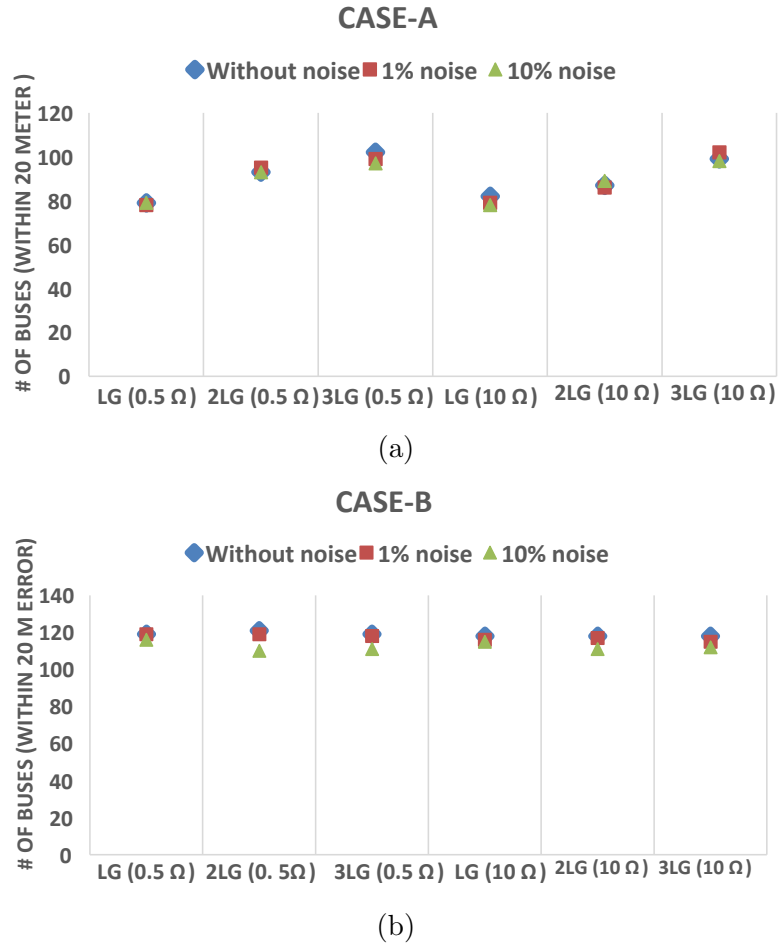
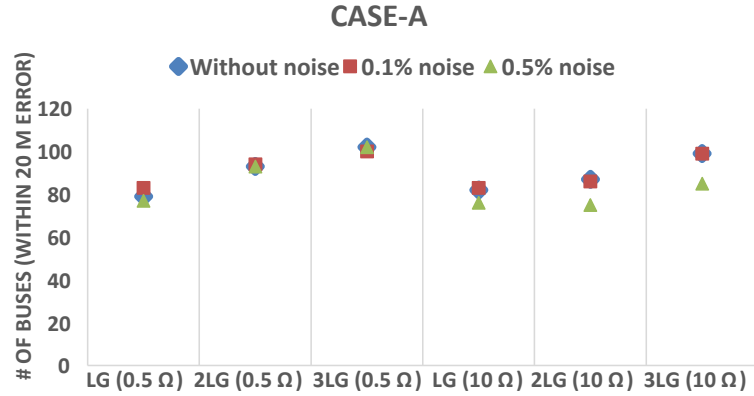


Figure 4.20: Simulation results with errors in line impedances. a) Case-A. b) Case-B.

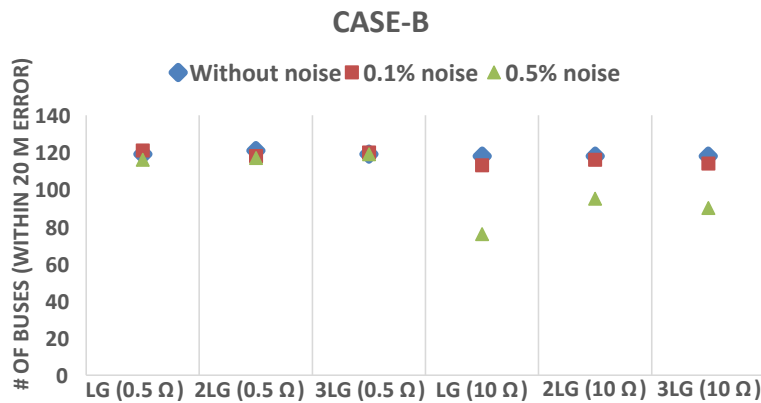
the simulation results in [78] and that from this paper. It can be seen that our approach outperforms the method in [78] for its higher accuracy in fault location identification.

4.4 Conclusion

In this chapter, two applications of MIP in power systems are presented. In the first application, an efficient MINLP problem is formulated to model Type-III WTs accurately, considering the control impact. A one-step algorithm is developed to compute the steady-state operating point of Type-III WTs for various balanced stator voltage levels. For a given stator voltage and wind speed, the electrical and mechanical variables of the system can be



(a)



(b)

Figure 4.21: Simulation results with microPMUs synchronization errors. a) Case-A. b) Case-B.

computed. Lossy DFIG back-to-back converters are considered. The formulated problem is non-linear, so it is solved using BMIBNB (a built-in solver on YALMIP). The solver implements a standard branch and bound algorithm. The solver relies on external linear, quadratic, and semidefinite programming solvers for solving the lower bounding relaxation problems and non-linear solvers for the upper bound computations. It also uses an external linear programming solver for bound strengthening. The results obtained by solving the formulated problem are validated with electromagnetic transient (EMT) simulations.

In the second part of this chapter, a new application MIP is introduced in this dissertation to identify faults locations in distribution networks. An efficient MILP formulation is

Table 4.7: Comparison between the proposed method in this paper with [77] and [79]

Method	In this paper						In [77]						In [79]					
	19 microPMUs						13 microPMUs+load data+fault type						22 microPMUs					
	LG		LLG		3L		LG		LLG		3L		LG		LLG		3L	
type	0.5	10	0.5	10	0.5	10	0.5	10	0.5	10	0.5	10	0.5	10	0.5	10	0.5	10
R_f	0.5	10	0.5	10	0.5	10	0.5	10	0.5	10	0.5	10	0.5	10	0.5	10	0.5	10
0-100m	125	126	130	127	129	129	120	120	-	-	115	115	113	114	109	112	109	110
100-200m	8	7	3	6	4	3	12	12	-	-	15	15	15	14	18	16	20	18
200-300m	0	0	0	0	0	1	1	1	-	-	2	2	4	4	5	4	3	4
>300	0	0	0	0	0	0	0	0	-	-	1	1	1	1	1	1	1	1

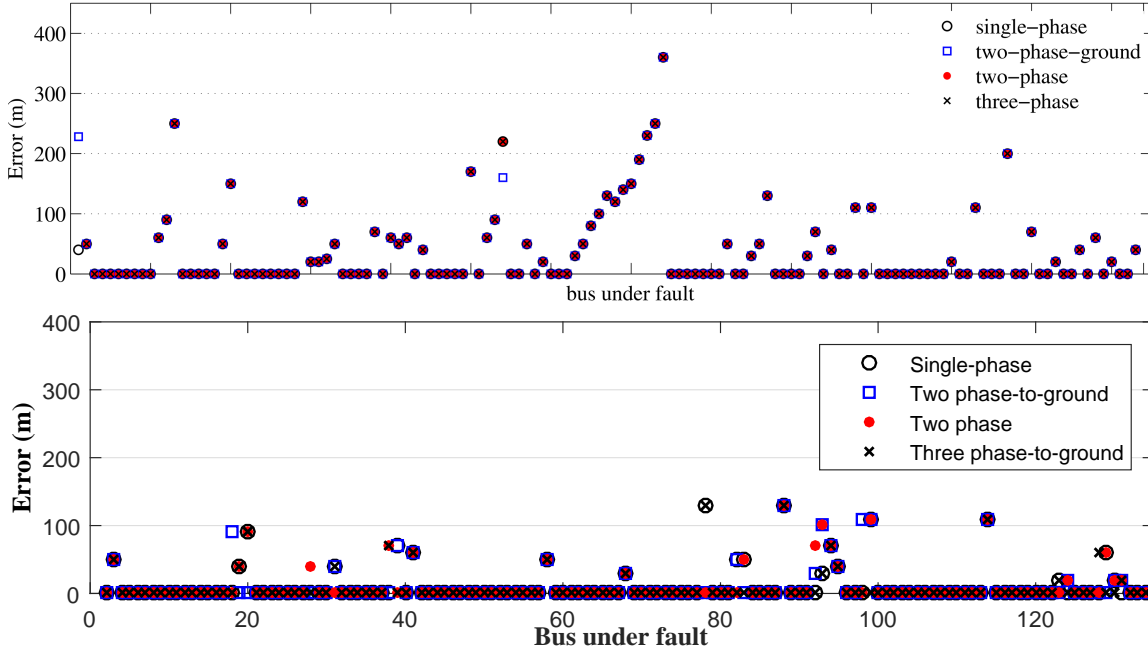


Figure 4.22: Location error for different faults ($R_f = 1 \Omega$) using microPMUs. a) Simulation results in [78]. b) Simulation results in this paper. Permission is included in Appendix A.

developed and introduced into fault identification problem formulation. The main findings of this research are summarized as follows.

- The proposed MIP-based method is capable of identifying fault location, fault type, and fault current with high accuracy in distribution networks using the pre and during fault voltages at the end of the branches in addition to the impedance bus matrix.
- The algorithm can be used with different characteristics networks. Feeders with single, double, or three lines and unbalance loading can be handled. Three feeders with different characteristics were chosen for demonstration.

- The results have shown that the method is robust against different challenging scenarios. It presented good performance with noisy measurements, inaccurate bus impedance matrix, distributed generation penetration, different fault resistance values, and a reduced number of microPMUs.

The formulated problem is linear, so it is solved by Mosek or Gurobi in CVX interface. Alternatively, BNB solver in YALMIP interface is used, which uses CPLEX as a lower solver and Rounder as an upper solver.

Chapter 5: Conclusion and Future Work

5.1 Conclusion

This dissertation focused on developing an accurate steady-state phasor model for Type-III WTGs. In contrast to conventional synchronous or asynchronous generators, Type-III WTGs are electronically coupled to the electrical grid. The steady-state and dynamic responses of DFIG-based WTGs are dependent on the converters' controllers. Accurate modeling requires simulating the behavior of the power electronics and control systems under a variety of operating conditions. This research area is analyzed in two tasks. The first task considers the balanced stator voltage situation, while the second task considers the unbalanced stator voltage situation. The first task proposes two methods for computing the steady-state operating conditions of Type-III WTGs while taking control limits into account. The proposed methods are applicable in both ideal and low-voltage operating conditions. The first method begins by formulating an optimization problem to determine the voltage thresholds at which the control system's behavior changes due to reaching the current limits. An efficient algorithm for steady-state calculations is designed using the identified limits. The problem is formulated as equality and inequality constraints and solved using a non-linear programming solver. The second method develops a one-step algorithm. The steady-state operating point of Type-III WTGs is computed using an efficient algorithm based on MINLP. The electrical and mechanical variables of the system can be calculated given the stator voltage and wind speed. In that modeling, we considered a full-order model of DFIG-based WTGs. Certain oversimplifying assumptions that are frequently made in the literature are avoided. Losses

in the back-to-back converter are considered, as is the non-zero reactive power support provided by the grid-side converter. In comparison to state-of-the-art, the proposed methods result in significantly more accurate DFIG computation models. Electromagnetic transient (EMT) simulations are used to validate the proposed methods.

The second task proposes an adequate model of a Type-III WT under grid unbalance. Not only does the proposed model consider positive and negative sequence circuits, but also the third harmonic circuit. Along with modeling, we develop an efficient steady-state analysis algorithm. To accomplish this, harmonic circuit analysis is first performed on the induction machine, RSC, DC-link, and GSC ac side. Additionally, the relationships between the dc and ac side variables of the two dc/ac converters are examined. The steady-state analysis problem is formulated as a set of algebraic equality constraints. A non-linear optimization solver is used to solve the optimization problem. The analysis produces phasors for the harmonic components at the steady-state. The results are validated and compared to phasors derived from Fourier transforms of electromagnetic transient (EMT) simulation results.

5.2 Future Work

For further study of this dissertation, the following may be provided. The research in this dissertation can be extended by considering different control designs (e.g., unbalance mitigation controls). Moreover, incorporating the proposed model in load flow and short circuit studied can be investigated. A brief survey on the topic of islanded microgrid power flow is provided in the following section.

5.2.1 Islanded Microgrid Power Flow

The power flow analysis of islanded microgrids is a challenging task due to the following:

- 1) There is no bus that can be treated as an infinite bus that is capable of holding the system frequency and its local bus voltage to a constant value.
- 2) Given that there is no slack bus,

it will be impossible to make all DG units operate in PV or PQ modes. DGs and loads are regulated by droop/secondary controls. 3) Microgrids structure may vary, which impacts the solving algorithm [90].

In [91, 92], the power flow for an islanded microgrid is solved using the conventional approach. In these studies, the DG with the highest rating is selected as the slack bus, while other DGs are represented as PV or PQ buses with a pre-specified or selected active voltage magnitude and/or power. These methods assume the system frequency to be constant and ignore the decentralized droop control-based microgrid operation.

In [93], a novel three-phase power flow algorithm for islanded microgrids is proposed. The proposed method takes into account the absence of the slack bus in the system. The proposed method considers the three operation modes of DG units: PV, PQ, and droop. The number of mismatch equations describing each bus in the system depends on the type of the bus. There are 12 mismatch equations for the droop-buses, while there are 6 and 3 for PQ and PV buses. The system frequency is not pre-specified. It is assumed to be a variable and needs to be calculated. The authors implemented Newton-Trust region to overcome the challenges faced by Newton-Raphson algorithms when dealing with distribution systems. The set of non-linear equations describing the power flow is to be regarded as a minimization problem. In [94], Newton-Raphson algorithm is modified to take into account the droop characteristics of DGs, while the well-known backward/forward sweep algorithm is expanded in [95] to cope with the lack of slack bus and the droop characteristics of DGs. The system frequency is assumed to be a variable in both methods.

None of the aforementioned algorithms have addressed the hierarchical control effects in microgrids. In [96] a generalized microgrid power flow is proposed, which is able to incorporate hierarchical control schemes into the microgrids power flow. The proposed approach is based on the direct backward/forward sweep algorithm. No slack bus is assumed to exist, so the power loss is shared among all DGs. A generalized PQ bus is introduced for model-

ing DG in microgrids. The proposed method is only applicable to radial or weakly meshed microgrids as it is an extension of the direct backward/forward sweep algorithm.

In [97], an enhanced Newton-type microgrid power flow (EMPF) applicable for meshed and radial structures is proposed. In addition to the traditional PV and PQ buses, a new bus type called DER bus is introduced for distributed energy resources equipped with droop and/or secondary control. The Jacobian matrix is modified to incorporate droop controls and various secondary control modes. As the newton type power flow is sensitive to the starting point, the power flow is first run with droop control. The obtain results used are as initial values for the main problem with the hierarchy.

In [90], the implicit Z_{bus} Gauss algorithm (GRev), which can handle arbitrary structures, is adopted. The proposed algorithm allows incorporating DER hierarchical controls as well as load droops. Due to its insensitivity to initial values, GRev is more robust than Newton's method. Compared to the Newton-based algorithm in [97], the GRev algorithm is more advantageous in computational speed. It is a derivative-free approach that avoids updating the Jacobian matrix at each iteration.

References

- [1] American Wind Energy Association (AWEA), “Wind powers america first quarter 2020 report,” 2020.
- [2] Global Wind Energy Council. Global wind report 2018. [Online]. Available: URL:<https://gwec.net/global-wind-report-2018/>
- [3] R. H. Wiser and M. Bolinger, “2018 wind technologies market report,” Tech. Rep., 08/2019 2019. [Online]. Available: <https://emp.lbl.gov/wind-technologies-market-report>
- [4] S. Lindenberg, B. Smith, K. O’Dell, and E. DeMeo, “20 percent wind energy by 2030: Increasing wind energy’s contribution to us electricity supply,” *Tech. Rep., US Department of Energy*, 2008.
- [5] R. Wiser, M. Hand, J. Seel, and B. Paulos, “Reducing wind energy costs through increased turbine size: is the sky the limit?” *Rev. Berkeley National Laboratory Electricity Markets and Policy Group*, 2016.
- [6] Z. Chen, J. M. Guerrero, and F. Blaabjerg, “A review of the state of the art of power electronics for wind turbines,” *IEEE Transactions on Power Electronics*, vol. 24, no. 8, pp. 1859–1875, 2009.
- [7] P. Pourbeik, A. Ellis, J. Sanchez-Gasca, Y. Kazachkov, E. Muljadi, J. Senthil, and D. Davies, “Generic stability models for type 3 4 wind turbine generators for wecc,” in *2013 IEEE Power Energy Society General Meeting*, 2013, pp. 1–5.
- [8] L. Fan, S. Yuvarajan, and R. Kavasseri, “Harmonic analysis of a dfig for a wind energy conversion system,” *IEEE Transactions on Energy Conversion*, vol. 25, no. 1, pp. 181–190, 2010.
- [9] J. A. Baroudi, V. Dinavahi, and A. M. Knight, “A review of power converter topologies for wind generators,” *Renewable Energy*, vol. 32, no. 14, pp. 2369 – 2385, 2007. [Online]. Available: <http://www.sciencedirect.com/science/article/pii/S0960148106003430>
- [10] J. LÓpez, E. GubÍA, P. Sanchis, X. Roboam, and L. Marroyo, “Wind turbines based on doubly fed induction generator under asymmetrical voltage dips,” *IEEE Transactions on Energy Conversion*, vol. 23, no. 1, pp. 321–330, 2008.

- [11] A. M. S. Al-bayati, F. Mancilla-David, and J. L. Domínguez-García, “Aggregated models of wind farms: Current methods and future trends,” in *2016 North American Power Symposium (NAPS)*, 2016, pp. 1–6.
- [12] S. Chattopadhyay, M. Mitra, and S. Sengupta, “Electric power quality,” in *Electric Power Quality*. Springer, 2011, pp. 5–12.
- [13] “Ieee recommended practice for monitoring electric power quality,” *IEEE Std 1159-2019 (Revision of IEEE Std 1159-2009)*, pp. 1–98, 2019.
- [14] E. Nycander and L. Söder, “Review of european grid codes for wind farms and their implications for wind power curtailments,” in *17th International Wind Integration Workshop Stockholm, Sweden— 17–19 October 2018*, 2018.
- [15] C. Sourkounis and P. Tourou, “Grid code requirements for wind power integration in europe,” in *Conference Papers in Science*, vol. 2013. Hindawi, 2013.
- [16] X. Ye, Y. Qiao, and Z. Lu, “Cascading tripping out of numerous wind turbines in china: Fault evolution analysis and simulation study,” in *2012 IEEE Power and Energy Society General Meeting*, 2012, pp. 1–11.
- [17] G. Xiang, W. Hu, and Y. Min, “Study on cascading trip-off failure of large-scale wind farm in china,” in *2015 IEEE 10th Conference on Industrial Electronics and Applications (ICIEA)*, 2015, pp. 1353–1358.
- [18] H. Xu, J. Hu, and Y. He, “Operation of wind-turbine-driven dfig systems under distorted grid voltage conditions: Analysis and experimental validations,” *IEEE Transactions on Power Electronics*, vol. 27, no. 5, pp. 2354–2366, 2012.
- [19] O. Gomis-Bellmunt, A. Junyent-FerrÉ, A. Sumper, and J. Bergas-JanÉ, “Ride-through control of a doubly fed induction generator under unbalanced voltage sags,” *IEEE Transactions on Energy Conversion*, vol. 23, no. 4, pp. 1036–1045, 2008.
- [20] J. Lopez, E. Gubia, E. Olea, J. Ruiz, and L. Marroyo, “Ride through of wind turbines with doubly fed induction generator under symmetrical voltage dips,” *IEEE Transactions on Industrial Electronics*, vol. 56, no. 10, pp. 4246–4254, 2009.
- [21] M. Kiani and W. Lee, “Effects of voltage unbalance and system harmonics on the performance of doubly fed induction wind generators,” *IEEE Transactions on Industry Applications*, vol. 46, no. 2, pp. 562–568, 2010.
- [22] Y. Zhou, P. Bauer, J. A. Ferreira, and J. Pierik, “Operation of grid-connected dfig under unbalanced grid voltage condition,” *IEEE Transactions on Energy Conversion*, vol. 24, no. 1, pp. 240–246, 2009.

- [23] L. Shang and J. Hu, "Sliding-mode-based direct power control of grid-connected wind-turbine-driven doubly fed induction generators under unbalanced grid voltage conditions," *IEEE Transactions on Energy Conversion*, vol. 27, no. 2, pp. 362–373, 2012.
- [24] H. Ko, G. Yoon, and W. Hong, "Active use of dfig-based variable-speed wind-turbine for voltage regulation at a remote location," *IEEE Transactions on Power Systems*, vol. 22, no. 4, pp. 1916–1925, 2007.
- [25] J. Lopez, P. Sanchis, X. Roboam, and L. Marroyo, "Dynamic behavior of the doubly fed induction generator during three-phase voltage dips," *IEEE Transactions on Energy Conversion*, vol. 22, no. 3, pp. 709–717, 2007.
- [26] J. Hu, H. Nian, H. Xu, and Y. He, "Dynamic modeling and improved control of dfig under distorted grid voltage conditions," *IEEE Transactions on Energy Conversion*, vol. 26, no. 1, pp. 163–175, 2011.
- [27] S. Chandrasekar and R. Gokaraju, "Dynamic phasor modeling of type 3 dfig wind generators (including ssci phenomenon) for short-circuit calculations," *IEEE Transactions on Power Delivery*, vol. 30, no. 2, pp. 887–897, 2015.
- [28] T. Demiray, F. Milano, and G. Andersson, "Dynamic phasor modeling of the doubly-fed induction generator under unbalanced conditions," in *2007 IEEE Lausanne Power Tech*, 2007, pp. 1049–1054.
- [29] T. Kauffmann, U. Karaagac, I. Kocar, H. Gras, J. Mahseredjian, B. Cetindag, and E. Farantatos, "Phasor domain modeling of type iii wind turbine generator for protection studies," in *2015 IEEE Power & Energy Society General Meeting*. IEEE, 2015, pp. 1–5.
- [30] P. Ledesma and J. Usaola, "Doubly fed induction generator model for transient stability analysis," *IEEE Transactions on Energy Conversion*, vol. 20, no. 2, pp. 388–397, 2005.
- [31] D. Gautam, V. Vittal, and T. Harbour, "Impact of increased penetration of dfig-based wind turbine generators on transient and small signal stability of power systems," *IEEE Transactions on power systems*, vol. 24, no. 3, pp. 1426–1434, 2009.
- [32] M. Wu and L. Xie, "Calculating steady-state operating conditions for dfig-based wind turbines," *IEEE Transactions on sustainable Energy*, vol. 9, no. 1, pp. 293–301, 2017.
- [33] J. F. Medina Padron and A. E. Feijoo Lorenzo, "Calculating steady-state operating conditions for doubly-fed induction generator wind turbines," *IEEE Transactions on Power Systems*, vol. 25, no. 2, pp. 922–928, 2010.
- [34] N. Amutha and B. K. Kumar, "Initialization of dfig based wind generating system," in *2014 Eighteenth National Power Systems Conference (NPSC)*, 2014, pp. 1–5.

- [35] S. S. K. V. and D. Thukaram, “Accurate modeling of doubly fed induction generator based wind farms in load flow analysis,” *Electric Power Systems Research*, vol. 155, pp. 363 – 371, 2018. [Online]. Available: <http://www.sciencedirect.com/science/article/pii/S0378779617303784>
- [36] D. R. Karthik and S. Mecha Kotian, “Initialization of doubly-fed induction generator wind turbines using noniterative method,” in *2019 8th International Conference on Power Systems (ICPS)*, 2019, pp. 1–6.
- [37] V. S. Sravan Kumar, “Computation of initial conditions for dynamic analysis of a doubly fed induction machine based on accurate equivalent circuit,” in *2019 IEEE International Electric Machines Drives Conference (IEMDC)*, 2019, pp. 307–313.
- [38] A. CVS, “Enhanced modelling of doubly fed induction generator in load flow analysis of distribution systems,” *IET Renewable Power Generation*, vol. 15, no. 5, pp. 980–989, 2021.
- [39] T. Lund, P. Sørensen, and J. Eek, “Reactive power capability of a wind turbine with doubly fed induction generator,” *Wind Energy: An International Journal for Progress and Applications in Wind Power Conversion Technology*, vol. 10, no. 4, pp. 379–394, 2007.
- [40] A. Mishra, P. Tripathi, and K. Chatterjee, “A review of harmonic elimination techniques in grid connected doubly fed induction generator based wind energy system,” *Renewable and Sustainable Energy Reviews*, vol. 89, pp. 1 – 15, 2018. [Online]. Available: <http://www.sciencedirect.com/science/article/pii/S1364032118300571>
- [41] B. Badrzadeh, M. Gupta, N. Singh, A. Petersson, L. Max, and M. Hogdahl, “Power system harmonic analysis in wind power plants — part i: Study methodology and techniques,” *2012 IEEE Industry Applications Society Annual Meeting*, pp. 1–11, 2012.
- [42] M. Lindholm and T. W. Rasmussen, “Harmonic analysis of doubly fed induction generators,” in *The Fifth International Conference on Power Electronics and Drive Systems, 2003. PEDS 2003.*, vol. 2, 2003, pp. 837–841 Vol.2.
- [43] A. Stefani, A. Yazidi, C. Rossi, F. Filippetti, D. Casadei, and G. Capolino, “Doubly fed induction machines diagnosis based on signature analysis of rotor modulating signals,” *IEEE Transactions on Industry Applications*, vol. 44, no. 6, pp. 1711–1721, 2008.
- [44] S. Schostan, K. Dettmann, I. Purellku, and D. Schulz, “Harmonics and powers of doubly fed induction generators at balanced sinusoidal voltages,” in *2010 International School on Nonsinusoidal Currents and Compensation*, 2010, pp. 213–217.
- [45] S. Williamson and S. Djurovic, “Origins of stator current spectra in dfigs with winding faults and excitation asymmetries,” in *2009 IEEE International Electric Machines and Drives Conference*, 2009, pp. 563–570.

- [46] V. . Phan and H. . Lee, “Stationary frame control scheme for a stand-alone doubly fed induction generator system with effective harmonic voltages rejection,” *IET Electric Power Applications*, vol. 5, no. 9, pp. 697–707, 2011.
- [47] A. C. Smith, “Harmonic field analysis for slip-ring motors including general rotor asymmetry,” *IEEE Transactions on Industry Applications*, vol. 26, no. 5, pp. 857–865, 1990.
- [48] L. Xu and Y. Wang, “Dynamic modeling and control of dfig-based wind turbines under unbalanced network conditions,” *IEEE Transactions on Power Systems*, vol. 22, no. 1, pp. 314–323, 2007.
- [49] M. Z. Kamh and R. Iravani, “Three-phase steady-state model of type-3 wind generation unit—part i: Mathematical models,” *IEEE Transactions on Sustainable Energy*, vol. 2, no. 4, pp. 477–486, 2011.
- [50] T. Kauffmann, U. Karaagac, I. Kocar, H. Gras, J. Mahseredjian, B. Cetindag, and E. Farantatos, “Phasor domain modeling of type iii wind turbine generator for protection studies,” in *2015 IEEE Power Energy Society General Meeting*, 2015, pp. 1–5.
- [51] T. Kauffmann, U. Karaagac, I. Kocar, S. Jensen, J. Mahseredjian, and E. Farantatos, “An accurate type iii wind turbine generator short circuit model for protection applications,” *IEEE Transactions on Power Delivery*, vol. 32, no. 6, pp. 2370–2379, 2017.
- [52] S. F. Zarei, H. Mokhtari, M. A. Ghasemi, S. Peyghami, P. Davari, and F. Blaabjerg, “Control of grid-following inverters under unbalanced grid conditions,” *IEEE Transactions on Energy Conversion*, vol. 35, no. 1, pp. 184–192, 2020.
- [53] M. Alqahtani, Z. Miao, and L. Fan, “Induction machines limits identification during abnormal conditions using an optimization algorithm,” in *2020 IEEE Texas Power and Energy Conference (TPEC)*, 2020, pp. 1–6.
- [54] J. Lofberg, “Yalmip: A toolbox for modeling and optimization in matlab,” in *Computer Aided Control Systems Design, 2004 IEEE International Symposium on*. IEEE, 2004, pp. 284–289.
- [55] S. Muller, M. Deicke, and R. W. De Doncker, “Doubly fed induction generator systems for wind turbines,” *IEEE Industry applications magazine*, vol. 8, no. 3, pp. 26–33, 2002.
- [56] M. Alqahtani, Z. Miao, and L. Fan, “Steady-state harmonic analysis of type-iii wind turbines subject to unbalance,” *submitted, Electric Power Systems Research*, 2021.
- [57] L. Fan, S. Yuvarajan, and R. Kavasseri, “Harmonic analysis of a dfig for a wind energy conversion system,” *IEEE Transactions on Energy Conversion*, vol. 25, no. 1, pp. 181–190, 2010.

- [58] P. N. Enjeti and S. A. Choudhury, "A new control strategy to improve the performance of a pwm ac to dc converter under unbalanced operating conditions," *IEEE Transactions on Power Electronics*, vol. 8, no. 4, pp. 493–500, 1993.
- [59] D. Zhou, P. Tu, and Y. Tang, "Multivector model predictive power control of three-phase rectifiers with reduced power ripples under nonideal grid conditions," *IEEE Transactions on Industrial Electronics*, vol. 65, no. 9, pp. 6850–6859, 2018.
- [60] Y. Zhang, C. Qu, and J. Gao, "Performance improvement of direct power control of pwm rectifier under unbalanced network," *IEEE Transactions on Power Electronics*, vol. 32, no. 3, pp. 2319–2328, 2017.
- [61] M. Alqahtani, Z. Miao, and L. Fan, "Mixed integer programming formulation for fault identification based on micropmus," *International Transactions on Electrical Energy Systems*, vol. n/a, no. n/a, p. e12949. [Online]. Available: <https://onlinelibrary.wiley.com/doi/abs/10.1002/2050-7038.12949>
- [62] —, "Mip-based fault location identification using micropmus," in *2018 North American Power Symposium (NAPS)*, 2018, pp. 1–5.
- [63] E. Netz, "Grid code—high and extra high voltage. e. on netz gmbh," Tech. Rep. [Online]. Available: <http://www.eonnetz.com/Ressources/downloads...>, Tech. Rep., 2006.
- [64] T. Kauffmann, U. Karaagac, I. Kocar, S. Jensen, J. Mahseredjian, and E. Farantatos, "An accurate type iii wind turbine generator short circuit model for protection applications," *IEEE Transactions on Power Delivery*, vol. 32, no. 6, pp. 2370–2379, 2016.
- [65] U. Karaagac, T. Kauffmann, I. Kocar, H. Gras, J. Mahseredjian, B. Cetindag, and E. Farantatos, "Phasor domain modeling of type-iv wind turbine generator for protection studies," in *2015 IEEE Power Energy Society General Meeting*, 2015, pp. 1–5.
- [66] T. Kauffmann, U. Karaagac, I. Kocar, S. Jensen, E. Farantatos, A. Haddadi, and J. Mahseredjian, "Short-circuit model for type-iv wind turbine generators with decoupled sequence control," *IEEE Transactions on Power Delivery*, vol. 34, no. 5, pp. 1998–2007, 2019.
- [67] O. Goksu, R. Teodorescu, B. Bak-Jensen, F. Iov, and P. C. Kjaer, "An iterative approach for symmetrical and asymmetrical short-circuit calculations with converter-based connected renewable energy sources. application to wind power," in *2012 IEEE Power and Energy Society General Meeting*, 2012, pp. 1–8.
- [68] J. Mora-Florez, J. Melendez, and G. Carrillo-Caicedo, "Comparison of impedance based fault location methods for power distribution systems," *Electric Power Systems Research*, vol. 78, no. 4, pp. 657–666, 2008.

- [69] M. Farajollahi, A. Shahsavari, and H. Mohsenian-Rad, "Location identification of high impedance faults using synchronized harmonic phasors," in *Power & Energy Society Innovative Smart Grid Technologies Conference (ISGT), 2017 IEEE*. IEEE, 2017, pp. 1–5.
- [70] R. Krishnathevar and E. E. Ngu, "Generalized impedance-based fault location for distribution systems," *IEEE transactions on power delivery*, vol. 27, no. 1, pp. 449–451, 2012.
- [71] R. H. Salim, M. Resener, A. D. Filomena, K. R. C. De Oliveira, and A. S. Bretas, "Extended fault-location formulation for power distribution systems," *IEEE transactions on power delivery*, vol. 24, no. 2, pp. 508–516, 2009.
- [72] G. W. Chang, J.-P. Chao, H. M. Huang, C.-I. Chen, and S.-Y. Chu, "On tracking the source location of voltage sags and utility shunt capacitor switching transients," *IEEE Transactions on Power Delivery*, vol. 23, no. 4, p. 2124, 2008.
- [73] M. Pignati, L. Zanni, P. Romano, R. Cherkaoui, and M. Paolone, "Fault detection and faulted line identification in active distribution networks using synchrophasors-based real-time state estimation," *IEEE Transactions on Power Delivery Pwrld*, vol. 32, no. EPFL-ARTICLE-218391, pp. 381–392, 2017.
- [74] L. Lee and V. Centeno, "Comparison of μ pmu and pmu," in *2018 Clemson University Power Systems Conference (PSC)*, 2018, pp. 1–6.
- [75] E. Dusabimana and S.-G. Yoon, "A survey on the micro-phasor measurement unit in distribution networks," *Electronics*, vol. 9, no. 2, p. 305, 2020.
- [76] A. Jain and S. Bhullar, "Micro-phasor measurement units (μ pmus) and its applications in smart distribution systems," in *ISGW 2017: Compendium of Technical Papers*. Springer, 2018, pp. 81–92.
- [77] F. C. Trindade, W. Freitas, and J. C. Vieira, "Fault location in distribution systems based on smart feeder meters," *IEEE transactions on Power Delivery*, vol. 29, no. 1, pp. 251–260, 2014.
- [78] P. A. Cavalcante and M. C. de Almeida, "Fault location approach for distribution systems based on modern monitoring infrastructure," *IET Generation, Transmission & Distribution*, vol. 12, no. 1, pp. 94–103, 2017.
- [79] M. Majidi, A. Arabali, and M. Etezadi-Amoli, "Fault location in distribution networks by compressive sensing," *IEEE Transactions on Power Delivery*, vol. 30, no. 4, pp. 1761–1769, 2015.
- [80] M. Majidi, M. Etezadi-Amoli, and M. S. Fadali, "A novel method for single and simultaneous fault location in distribution networks," *IEEE Transactions on Power Systems*, vol. 30, no. 6, pp. 3368–3376, 2015.

- [81] M. Majidi and M. Etezadi-Amoli, “A new fault location technique in smart distribution networks using synchronized/nonsynchronized measurements,” *IEEE Transactions on Power Delivery*, vol. 33, no. 3, pp. 1358–1368, 2018.
- [82] G. Optimization, “Gurobi optimizer reference manual; gurobi optimization,” *Inc.: Houston, TX, USA*, 2016.
- [83] IBM ILOG, “User’s Manual for CPLEX 12.1,” *User’s Manual for CPLEX*, 2009.
- [84] A. MOSEK, “The mosek optimization toolbox for matlab manual. version 7.1 (revision 28), 2015,” 2017.
- [85] R. C. Dugan, “Reference guide: The open distribution system simulator (opends),” *Electric Power Research Institute, Inc*, vol. 7, 2012.
- [86] M. Grant, S. Boyd, and Y. Ye, “Cvx: Matlab software for disciplined convex programming,” 2008.
- [87] R. Dugan, “Distribution test feeders-distribution test feeder working group-ieee pes distribution system analysis subcommittee,” *Ewh. ieee. org*, 2017.
- [88] H. Sun, D. Nikovski, T. Takano, Y. Kojima, and T. Ohno, “Method for locating of single-phase-to-ground faults in ungrounded distribution systems,” in *Innovative Smart Grid Technologies-Asia (ISGT Asia), 2013 IEEE*. IEEE, 2013, pp. 1–6.
- [89] R. A. F. Pereira, L. G. W. da Silva, M. Kezunovic, and J. R. S. Mantovani, “Improved fault location on distribution feeders based on matching during-fault voltage sags,” *IEEE Transactions on Power Delivery*, vol. 24, no. 2, pp. 852–862, 2009.
- [90] F. Feng and P. Zhang, “Implicit Z_{bus} gauss algorithm revisited,” *IEEE Transactions on Power Systems*, vol. 35, no. 5, pp. 4108–4111, 2020.
- [91] H. Nikkhajoei and R. Iravani, “Steady-state model and power flow analysis of electronically-coupled distributed resource units,” *IEEE Transactions on Power Delivery*, vol. 22, no. 1, pp. 721–728, 2006.
- [92] M. Z. Kamh and R. Iravani, “Unbalanced model and power-flow analysis of microgrids and active distribution systems,” *IEEE Transactions on Power Delivery*, vol. 25, no. 4, pp. 2851–2858, 2010.
- [93] M. M. A. Abdelaziz, H. E. Farag, E. F. El-Saadany, and Y. A.-R. I. Mohamed, “A novel and generalized three-phase power flow algorithm for islanded microgrids using a newton trust region method,” *IEEE Transactions on Power Systems*, vol. 28, no. 1, pp. 190–201, 2012.

- [94] F. Mumtaz, M. Syed, M. Al Hosani, and H. Zeineldin, “A novel approach to solve power flow for islanded microgrids using modified newton raphson with droop control of dg,” *IEEE Transactions on Sustainable Energy*, vol. 7, no. 2, pp. 493–503, 2015.
- [95] G. Díaz, J. Gómez-Aleixandre, and J. Coto, “Direct backward/forward sweep algorithm for solving load power flows in ac droop-regulated microgrids,” *IEEE Transactions on Smart Grid*, vol. 7, no. 5, pp. 2208–2217, 2015.
- [96] L. Ren and P. Zhang, “Generalized microgrid power flow,” *IEEE Transactions on Smart Grid*, vol. 9, no. 4, pp. 3911–3913, 2018.
- [97] F. Feng and P. Zhang, “Enhanced microgrid power flow incorporating hierarchical control,” *IEEE Transactions on Power Systems*, vol. 35, no. 3, pp. 2463–2466, 2020.

Appendix A: Copyright Permissions

Reprint permission of Figure 1.1

Home ? Live Chat Mohammed Alqahtani



Requesting permission to reuse content from an IEEE publication

Generic stability models for type 3 & 4 wind turbine generators for WECC
Conference Proceedings: 2013 IEEE Power & Energy Society General Meeting
Author: P. Pourbeik
Publisher: IEEE
Date: 2013
Copyright © 2013, IEEE

Thesis / Dissertation Reuse

The IEEE does not require individuals working on a thesis to obtain a formal reuse license, however, you may print out this statement to be used as a permission grant:

Requirements to be followed when using any portion (e.g., figure, graph, table, or textual material) of an IEEE copyrighted paper in a thesis:

- 1) In the case of textual material (e.g., using short quotes or referring to the work within these papers) users must give full credit to the original source (author, paper, publication) followed by the IEEE copyright line © 2011 IEEE.
- 2) In the case of illustrations or tabular material, we require that the copyright line © [Year of original publication] IEEE appear prominently with each reprinted figure and/or table.
- 3) If a substantial portion of the original paper is to be used, and if you are not the senior author, also obtain the senior author's approval.

Requirements to be followed when using an entire IEEE copyrighted paper in a thesis:

- 1) The following IEEE copyright/ credit notice should be placed prominently in the references: © [year of original publication] IEEE. Reprinted, with permission, from [author names, paper title, IEEE publication title, and month/year of publication]
- 2) Only the accepted version of an IEEE copyrighted paper can be used when posting the paper or your thesis on-line.
- 3) In placing the thesis on the author's university website, please display the following message in a prominent place on the website: In reference to IEEE copyrighted material which is used with permission in this thesis, the IEEE does not endorse any of [university/educational entity's name goes here]'s products or services. Internal or personal use of this material is permitted. If interested in reprinting/republishing IEEE copyrighted material for advertising or promotional purposes or for creating new collective works for resale or redistribution, please go to http://www.ieee.org/publications_standards/publications/rights/rights_link.html to learn how to obtain a License from RightsLink.

If applicable, University Microfilms and/or ProQuest Library, or the Archives of Canada may supply single copies of the dissertation.

[BACK](#) [CLOSE WINDOW](#)

© 2021 Copyright - All Rights Reserved | Copyright Clearance Center, Inc. | Privacy statement | Terms and Conditions
Comments? We would like to hear from you. E-mail us at customercare@copyright.com

Reprint permission of Figure 4.22

6/17/2021

RightsLink - Your Account



My Orders My Library My Profile Welcome mohammed23@usf.edu [Log out](#) | [Help](#)

My Orders > Orders > All Orders

License Details

This Agreement between Mr. Mohammed Alqahtani ("You") and John Wiley and Sons ("John Wiley and Sons") consists of your license details and the terms and conditions provided by John Wiley and Sons and Copyright Clearance Center.

[Print](#) [Copy](#)

License Number	5091600220757
License date	Jun 17, 2021
Licensed Content Publisher	John Wiley and Sons
Licensed Content Publication	IET Generation, Transmission & Distribution
Licensed Content Title	Fault location approach for distribution systems based on modern monitoring infrastructure
Licensed Content Author	Paulo A.H. Cavalcanle, Madson C. Almeida
Licensed Content Date	Oct 4, 2017
Licensed Content Volume	12
Licensed Content Issue	1
Licensed Content Pages	10
Type of Use	Dissertation/Thesis
Requestor type	University/Academic
Format	Print and electronic
Portion	Figure/table
Number of figures/tables	6
Will you be translating?	No
Title	Phasor Domain Modeling of Type-III Wind Turbines
Institution name	University of South Florida
Expected presentation date	Jun 2021
Order reference number	0
Portions	Figure 6
Requestor Location	Mr. Mohammed Alqahtani [Redacted] [Redacted] [Redacted]
Publisher Tax ID	Attn: Mr. Mohammed Alqahtani EU826007151
Total	0.00 USD

[BACK](#)

Copyright © 2021 Copyright Clearance Center, Inc. All Rights Reserved. [Privacy statement](#) . [Terms and Conditions](#) . Comments? We would like to hear from you. E-mail us at customer care@copyright.com

<https://s100.copyright.com/MyAccount/viewLicenseDetails?ref=2bf98aba-7cff-424f-a2b7-20b5e191cd7c>

1/1

Reprint permission of published paper for Chapter 2 and 3



Home

Help

Email Support

Sign in

Create Account



Induction Machines limits Identification During Abnormal Conditions Using an Optimization Algorithm

Conference Proceedings: 2020 IEEE Texas Power and Energy Conference (TPEC)

Author: Mohammed Alqahtani

Publisher: IEEE

Date: Feb. 2020

Copyright © 2020, IEEE

Thesis / Dissertation Reuse

The IEEE does not require individuals working on a thesis to obtain a formal reuse license, however, you may print out this statement to be used as a permission grant:

Requirements to be followed when using any portion (e.g., figure, graph, table, or textual material) of an IEEE copyrighted paper in a thesis:

- 1) In the case of textual material (e.g., using short quotes or referring to the work within these papers) users must give full credit to the original source (author, paper, publication) followed by the IEEE copyright line © 2011 IEEE.
- 2) In the case of illustrations or tabular material, we require that the copyright line © [Year of original publication] IEEE appear prominently with each reprinted figure and/or table.
- 3) If a substantial portion of the original paper is to be used, and if you are not the senior author, also obtain the senior author's approval.

Requirements to be followed when using an entire IEEE copyrighted paper in a thesis:

- 1) The following IEEE copyright/ credit notice should be placed prominently in the references: © [year of original publication] IEEE. Reprinted, with permission, from [author names, paper title, IEEE publication title, and month/year of publication]
- 2) Only the accepted version of an IEEE copyrighted paper can be used when posting the paper or your thesis online.
- 3) In placing the thesis on the author's university website, please display the following message in a prominent place on the website: In reference to IEEE copyrighted material which is used with permission in this thesis, the IEEE does not endorse any of [university/educational entity's name goes here]'s products or services. Internal or personal use of this material is permitted. If interested in reprinting/republishing IEEE copyrighted material for advertising or promotional purposes or for creating new collective works for resale or redistribution, please go to http://www.ieee.org/publications_standards/publications/rights/rights_link.html to learn how to obtain a License from RightsLink.

If applicable, University Microfilms and/or ProQuest Library, or the Archives of Canada may supply single copies of the dissertation.

BACK

CLOSE WINDOW

Reprint permission of published paper for Chapter 4



Home

Help

Email Support

Sign in

Create Account



MIP-Based Fault Location Identification Using MicroPMUs

Conference Proceedings: 2018 North American Power Symposium (NAPS)

Author: Mohammed Alqahtani

Publisher: IEEE

Date: Sept. 2018

Copyright © 2018, IEEE

Thesis / Dissertation Reuse

The IEEE does not require individuals working on a thesis to obtain a formal reuse license, however, you may print out this statement to be used as a permission grant:

Requirements to be followed when using any portion (e.g., figure, graph, table, or textual material) of an IEEE copyrighted paper in a thesis:

- 1) In the case of textual material (e.g., using short quotes or referring to the work within these papers) users must give full credit to the original source (author, paper, publication) followed by the IEEE copyright line © 2011 IEEE.
- 2) In the case of illustrations or tabular material, we require that the copyright line © [Year of original publication] IEEE appear prominently with each reprinted figure and/or table.
- 3) If a substantial portion of the original paper is to be used, and if you are not the senior author, also obtain the senior author's approval.

Requirements to be followed when using an entire IEEE copyrighted paper in a thesis:

- 1) The following IEEE copyright/ credit notice should be placed prominently in the references: © [year of original publication] IEEE. Reprinted, with permission, from [author names, paper title, IEEE publication title, and month/year of publication]
- 2) Only the accepted version of an IEEE copyrighted paper can be used when posting the paper or your thesis on-line.
- 3) In placing the thesis on the author's university website, please display the following message in a prominent place on the website: In reference to IEEE copyrighted material which is used with permission in this thesis, the IEEE does not endorse any of [university/educational entity's name goes here]'s products or services. Internal or personal use of this material is permitted. If interested in reprinting/republishing IEEE copyrighted material for advertising or promotional purposes or for creating new collective works for resale or redistribution, please go to http://www.ieee.org/publications_standards/publications/rights/rights_link.html to learn how to obtain a License from RightsLink.

If applicable, University Microfilms and/or ProQuest Library, or the Archives of Canada may supply single copies of the dissertation.

BACK

CLOSE WINDOW

Reprint permission of published paper for Chapter 4

6/16/2021

RightsLink - Your Account



My Orders My Library My Profile Welcome mohammed23@usf.edu [Log out](#) | [Help](#)

My Orders > Orders > All Orders

License Details

This Agreement between Mr. Mohammed Alqahtani ("You") and John Wiley and Sons ("John Wiley and Sons") consists of your license details and the terms and conditions provided by John Wiley and Sons and Copyright Clearance Center.

[Print](#) [Copy](#)

License Number	508453100011
License date	Jun 08, 2021
Licensed Content Publisher	John Wiley and Sons
Licensed Content Publication	INTERNATIONAL TRANSACTIONS ON ELECTRICAL ENERGY SYSTEMS
Licensed Content Title	Mixed integer programming formulation for fault identification based on MicroPMUs
Licensed Content Author	Lingling Fan, Zhixin Miao, Mohammed Alqahtani
Licensed Content Date	Jun 3, 2021
Licensed Content Volume	0
Licensed Content Issue	0
Licensed Content Pages	21
Type of Use	Dissertation/Thesis
Requestor type	Author of this Wiley article
Format	Electronic
Portion	Full article
Will you be translating?	No
Title	Phasor Domain Modeling of Type-III Wind Turbines
Institution name	University of South Florida
Expected presentation date	Jun 2021
Order reference number	3
Requestor Location	Mr. Mohammed Alqahtani [REDACTED] [REDACTED]
Publisher Tax ID	Attn: Mr. Mohammed Alqahtani EU826007151
Total	0.00 USD

[BACK](#)

Copyright © 2021 Copyright Clearance Center, Inc. All Rights Reserved. [Privacy statement](#) . [Terms and Conditions](#) . Comments? We would like to hear from you. E-mail us at customer-care@copyright.com

<https://s100.copyright.com/MyAccount/viewLicenseDetails?ref=e775039e-57f0-4923-98af-5caabbc2aa96>

1/1

About the Author

Mohammed Alqahtani was born in October 30, 1989. He received BSc from Prince Sattam bin Abdulaziz University, Alkharj, Saudi Arabia in 2012. In 2016, he received MSc from the University of South Florida, Tampa, USA. where he is currently working towards his PhD since 2017. Mohammed works as a teaching assistant at Prince Sattam bin Abdulaziz University. His research interest includes power system computing and modeling.